

AD-A101 388

CALIFORNIA UNIV BERKELEY DEPT OF CIVIL ENGINEERING  
EXPERIMENTAL SOLITON WAVES. (U)

NOV 80 J HAMMACK

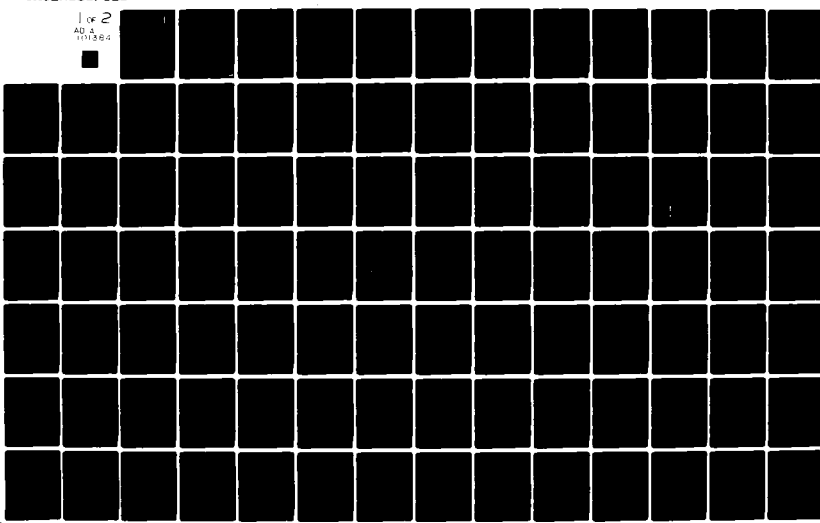
F/6 8/3

N00014-78-C-0889

NL

UNCLASSIFIED

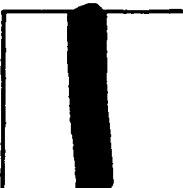
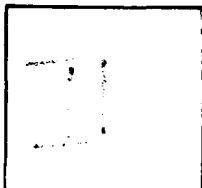
1 of 2  
AD-A101 388



AD A01384

DTIC ACCESSION NUMBER

PHOTOGRAPH THIS SHEET



LEVEL

California Univ., Berkeley  
Dept. of Civil Engineering

INVENTORY

Experimental Soliton Waves. Final Rept.

DOCUMENT IDENTIFICATION

Contract N00014-78-C-0889

14 Nov. 80

DISTRIBUTION STATEMENT A

Approved for public release.  
Distribution Unlimited

DISTRIBUTION STATEMENT

ACCESSION FOR

NTIS GRA&I



DTIC TAB



UNANNOUNCED



JUSTIFICATION

BY Pcs Ltr. (FL-88#R81-1647),  
DISTRIBUTION / dtd. 19 Jun '81

AVAILABILITY CODES

DIST

AVAIL AND/OR SPECIAL

A

DISTRIBUTION STAMP



DATE ACCESSIONED

81 7 14 001

DATE RECEIVED IN DTIC

PHOTOGRAPH THIS SHEET AND RETURN TO DTIC-DDA-2

AD A101384

FINAL REPORT

Experimental Soliton Waves

Contract Number N00014-78-C-0889

Department of the Navy  
Office of Naval Research

University of California  
Berkeley  
Department of Civil Engineering

J. Hammack, Principal Investigator

14 Nov. 1980

Approved for public release;  
Distribution unlimited

062-625  
11/14/80

Research initiated under contract N00014-78-C-0889 is most conveniently summarized in the form of four appendices. First, in Appendix I, the five different areas of research on water waves are briefly summarized. In two of these areas (evolution of long internal waves and evolution of envelope solitons) work has not been completed; some results to date are described. In the remaining three areas, final manuscripts have been completed and are presented in Appendices II, III, and IV. In particular, Appendix II is a copy of a paper entitled "Baroclinic Tsunami Generation" to appear in the *Journal of Physical Oceanography*, September 1980; Appendix III is a copy of a paper entitled "Long Waves Generated by Complex Bottom Motions" to appear in *Proceedings, 17th Conference on Coastal Engineering*; and Appendix IV is a copy of lecture notes on small-scale ocean waves presented at the summer (1980) course "Topics In Ocean Physics" held at the International School of Physics "Enrico Fermi", Varenna, Italy.

**Appendix I**

**Research Summary**

### Research Summary

Research conducted during the past year under Contract No. N00014-78-C-0889 may be conveniently divided into four categories.

I. Baroclinic Tsunami Generation. Utilizing experimental data obtained previously, a study was completed on the internal waves generated in a stratified ocean by a vertical motion of the sea floor. Details of this study are presented in the enclosed manuscript (see Appendix II) which will appear in the *Journal of Physical Oceanography*.

II. Evolution of Long Internal Waves. Subsequent to the generation processes mentioned above, the evolution of long internal waves on a thin pycnocline has been examined. Dr. Harvey Segur of Aeronautical Research Associates of Princeton and I have analyzed the experimental data and prepared a draft manuscript which examines several model equations for internal wave evolution in the context of experimental data. This work is ongoing; a copy of our final manuscript will be forwarded as soon as possible.

III. Long Waves Generated by a Complex Bottom Motion. As a final statement on barotropic water-wave generation by motions of the sea floor, Professor Frederic Raichlen (of Cal Tech) and I completed a manuscript (enclosed) which illustrates a technique for computing wave structure when the time-displacement history of the sea floor is very complicated. The analytical mode was verified by experiments. These results were presented at the 17th International Conference on Coastal Engineering in Sydney, Australia (March 1980), and the manuscript (see Appendix III) will appear in the meeting proceedings.

IV. Lecture Notes on Small-Scale Ocean Waves. At the invitation of the Italian Society of Physics, I presented a series of lectures at their summer course on "Topics in Ocean Physics" held during 7 July - 19 July 1980 at the International School of Physics "Enrico Fermi", in Varenna, Italy. These lectures focused on the nonlinear aspects of water waves including solitons and resonant-interaction forcing of edge waves. The collection of lecture notes from the ten invited speakers will be published by the North Holland Publishing Company. A copy of my notes is presented in Appendix IV.

V. Evolution of Short-Wave (Envelope) Solitons. The first goal of the experimental research program on short-wave evolution was the direct generation of an envelope soliton. The best results obtained to date for a wave packet with a carrier wave period  $T = 1$  sec and water depth  $h = 1$  m are shown in figures 1 abcd. Results at four positions along the (Berkeley) wave tank are presented with theoretical soliton profiles based on the local amplitude of the wave packet. The initial data measured at  $x = 6$  m from the wave paddle agree well with the theoretical soliton profile. During subsequent propagation the packet retains its compactness and travels with the (predicted) linear group speed of the carrier wave. However, the measured packet deviates slightly from the predicted soliton profile; this behavior is especially obvious at the last station ( $x = 45$  m) of measurement. The front-to-back asymmetry emerging at  $x = 45$  m is similar to that observed by previous researchers on deep water wave packets. In fact, the symmetrical measurements prior to the last measurement station are quite exceptional and have not been reported previously in the literature. (I might add that the first three wave traces of figure 1 are almost identical to those generated in the Florida facility; only the added length of the Berkeley wave tank permitted the distortion to be clearly observed.)

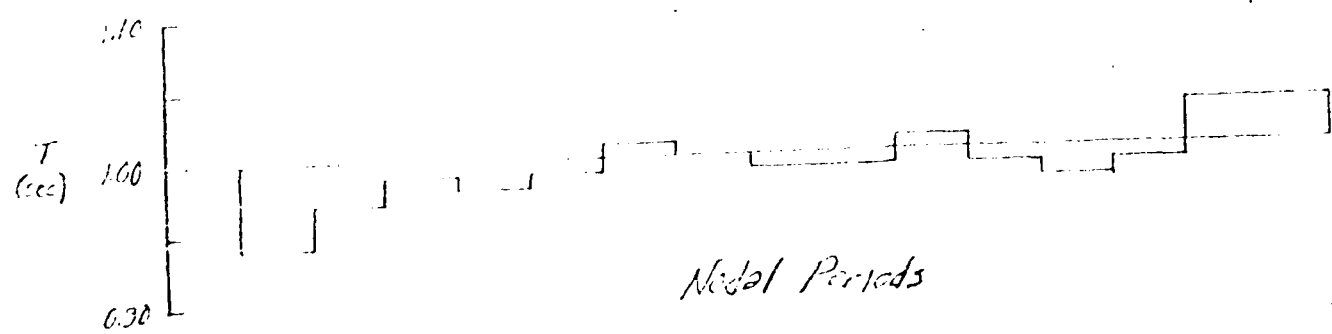
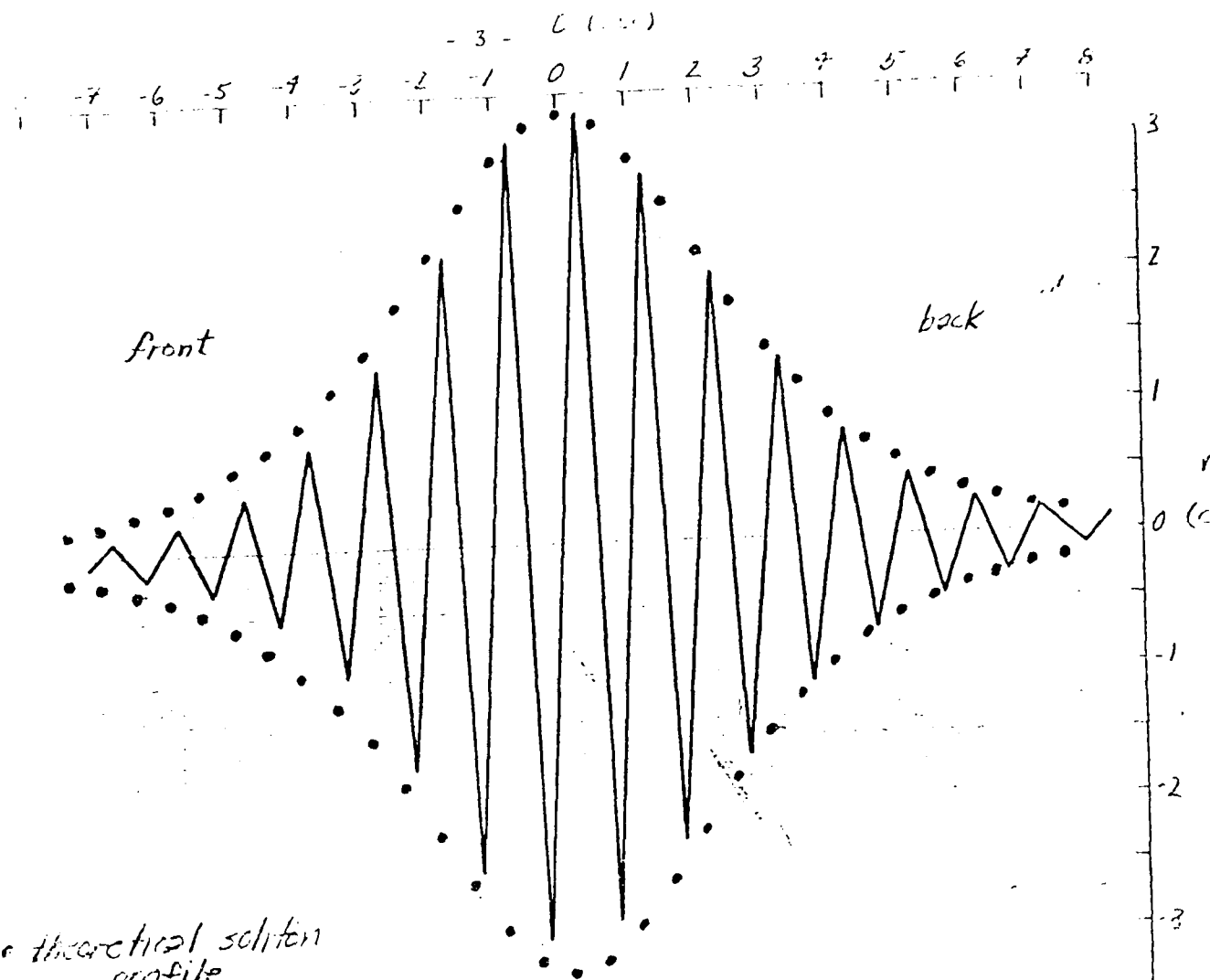
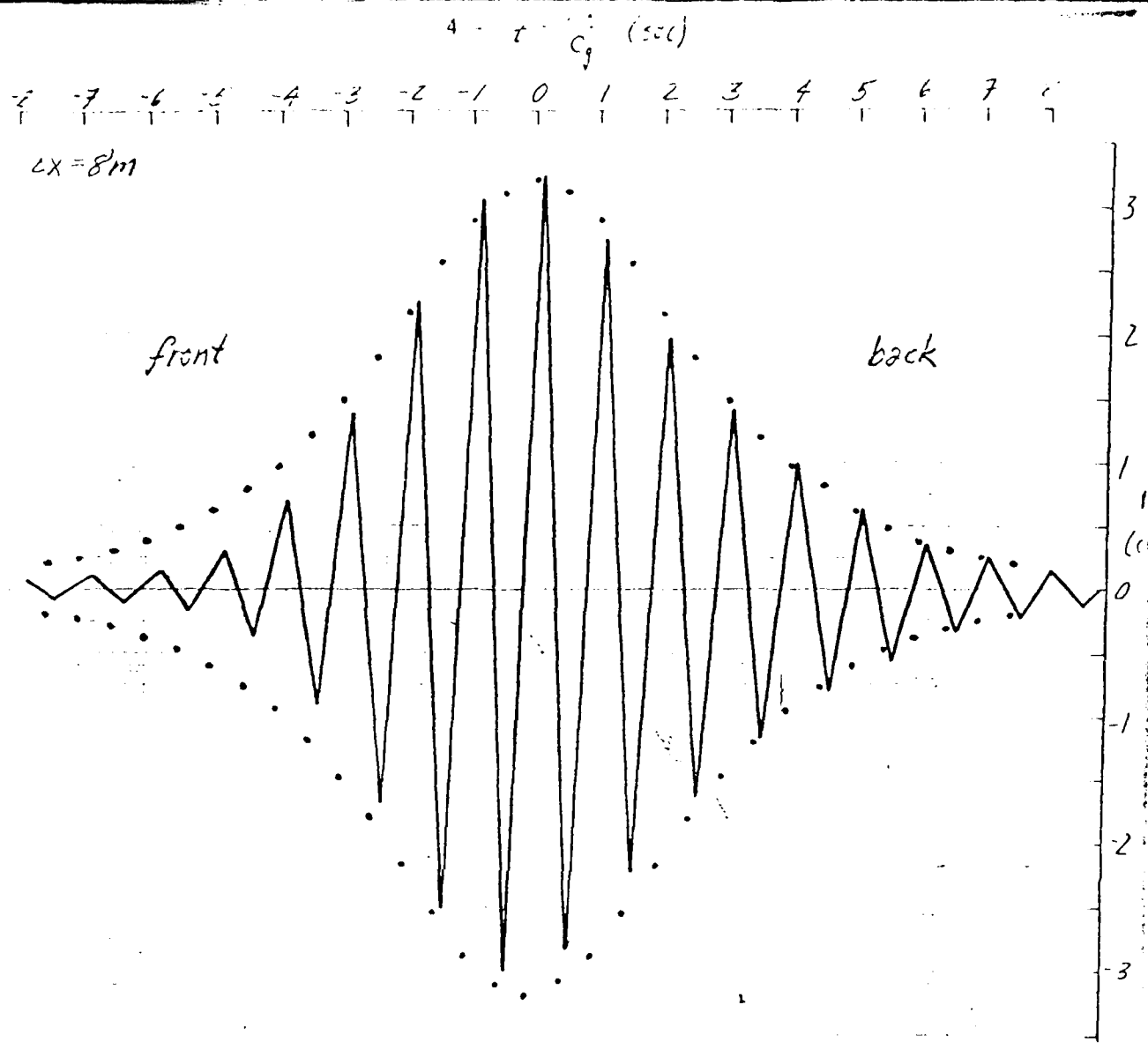


Figure 10:  $X=6m, T=10sec, k_1=10.5, A=108$

X=6m



$\pm$  uncertainty

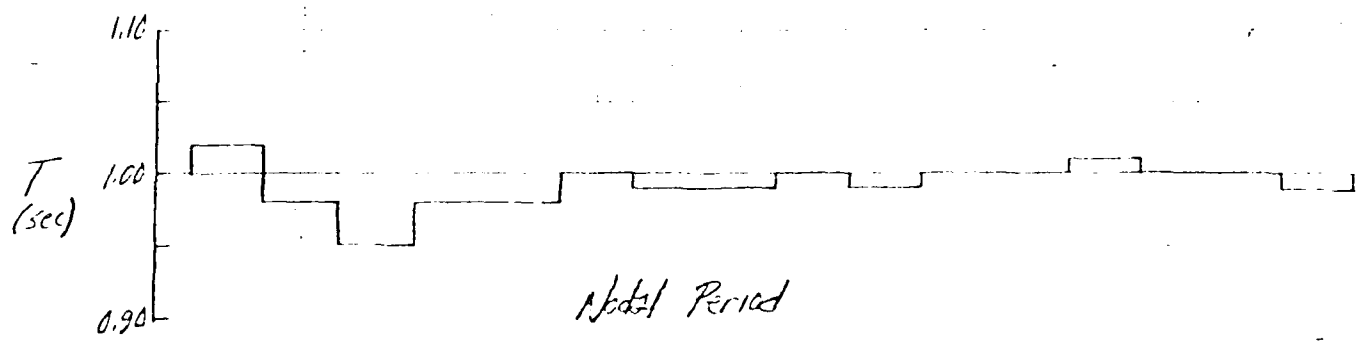


Figure 1b.  $X=17m$ ,  $T=1\text{ sec}$ ,  $T_m=20.8$ ,  $A=108$

15 Aug 79

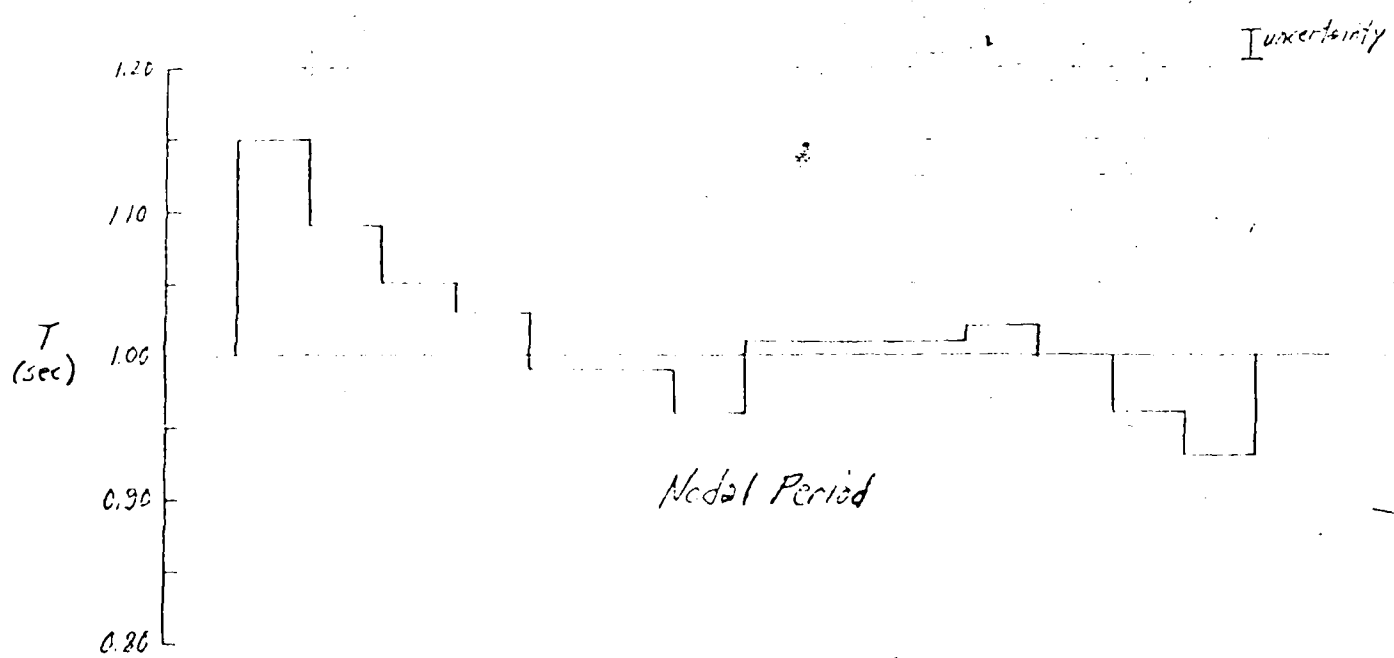
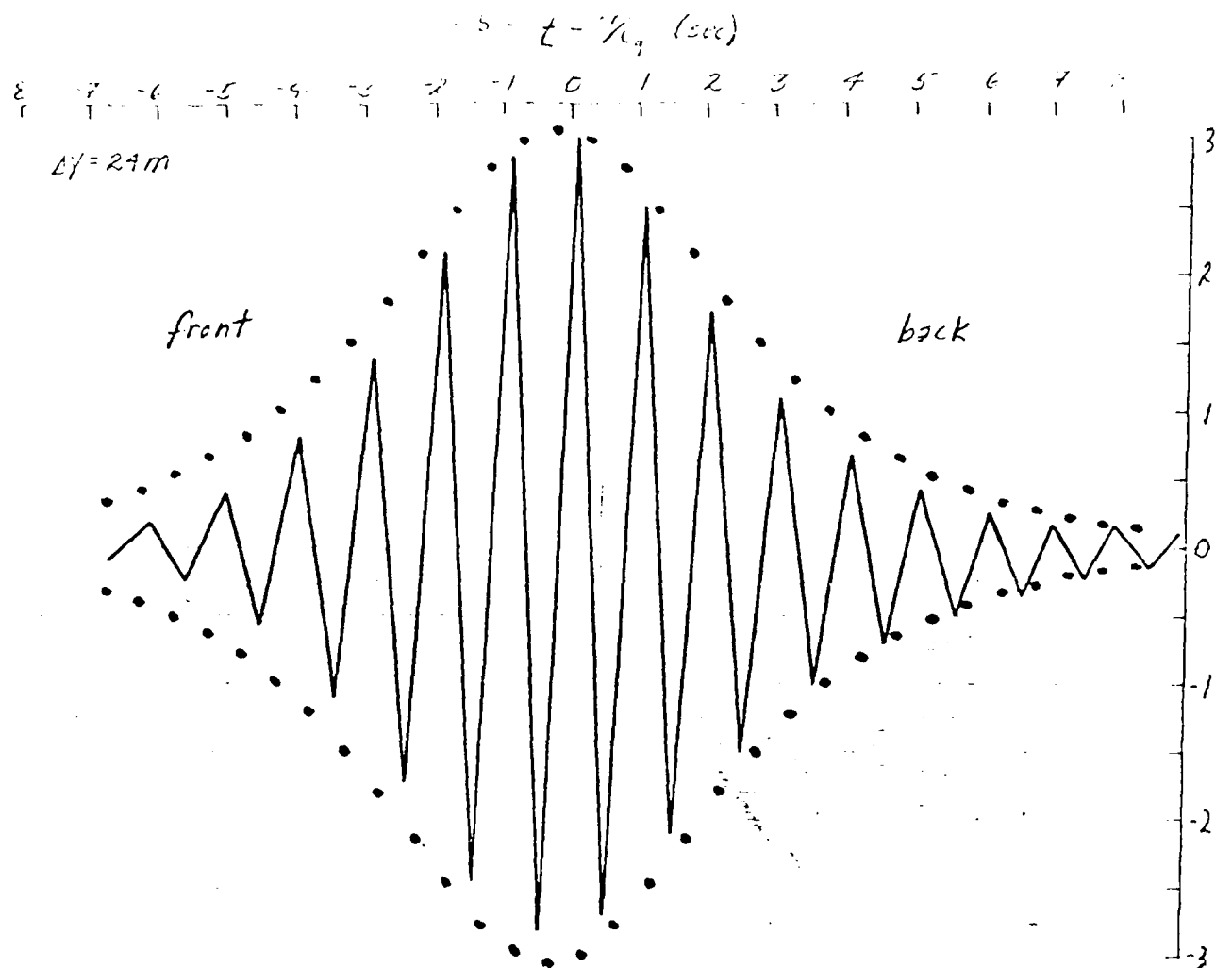


figure 1c,  $X=30\text{m}$ ,  $T=1.0\text{ sec}$ ,  $T_{c_0}=20.8$ ,  $\theta=105^\circ$   
15 Aug, 79

$x$   $\text{m}$

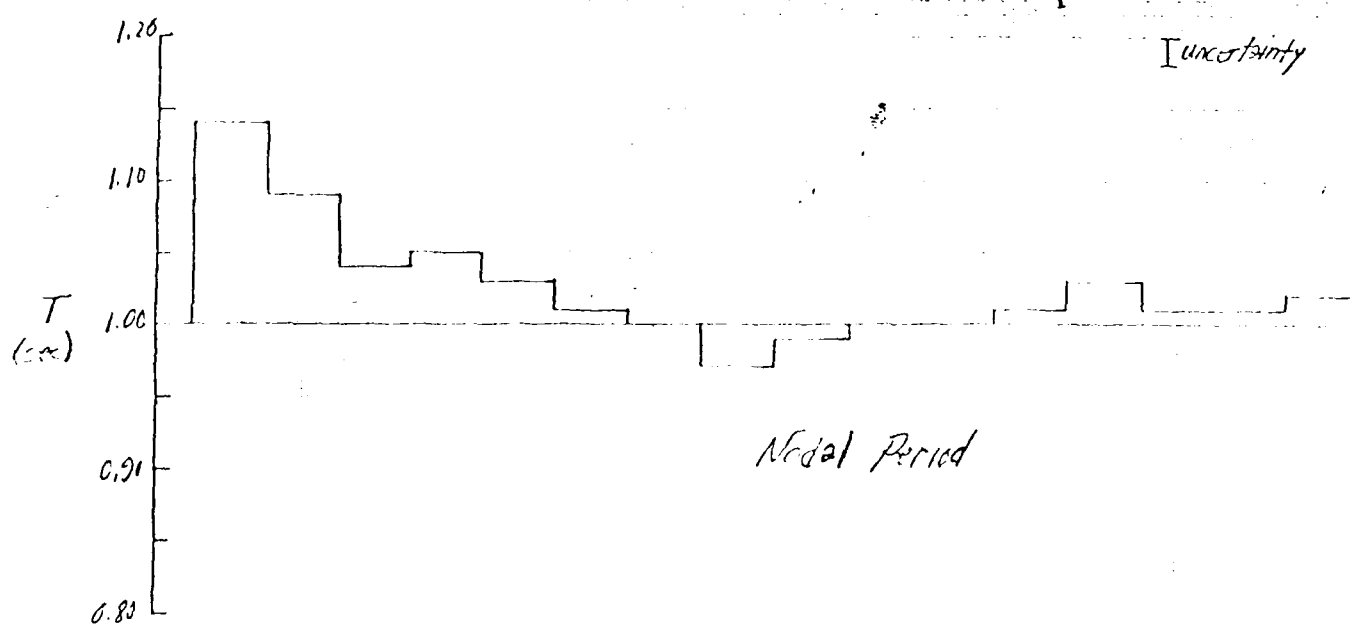
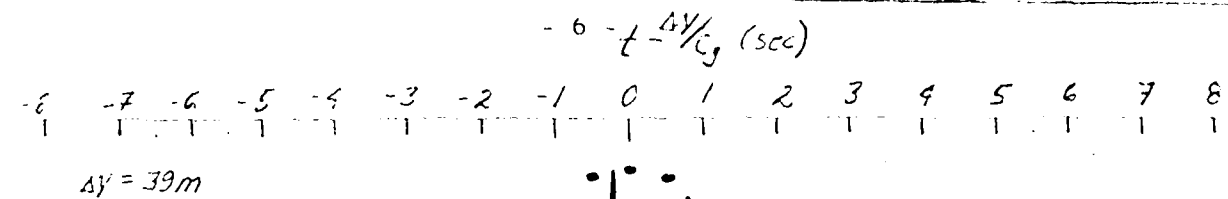


figure 1d.  $X = 45 \text{ m}$ ,  $T = 1.0 \text{ sec}$ ,  $T_m = 20.8$ ,  $A = 108$   
 $1/15 \text{ Aug } 79$

$X = 45 \text{ m}$

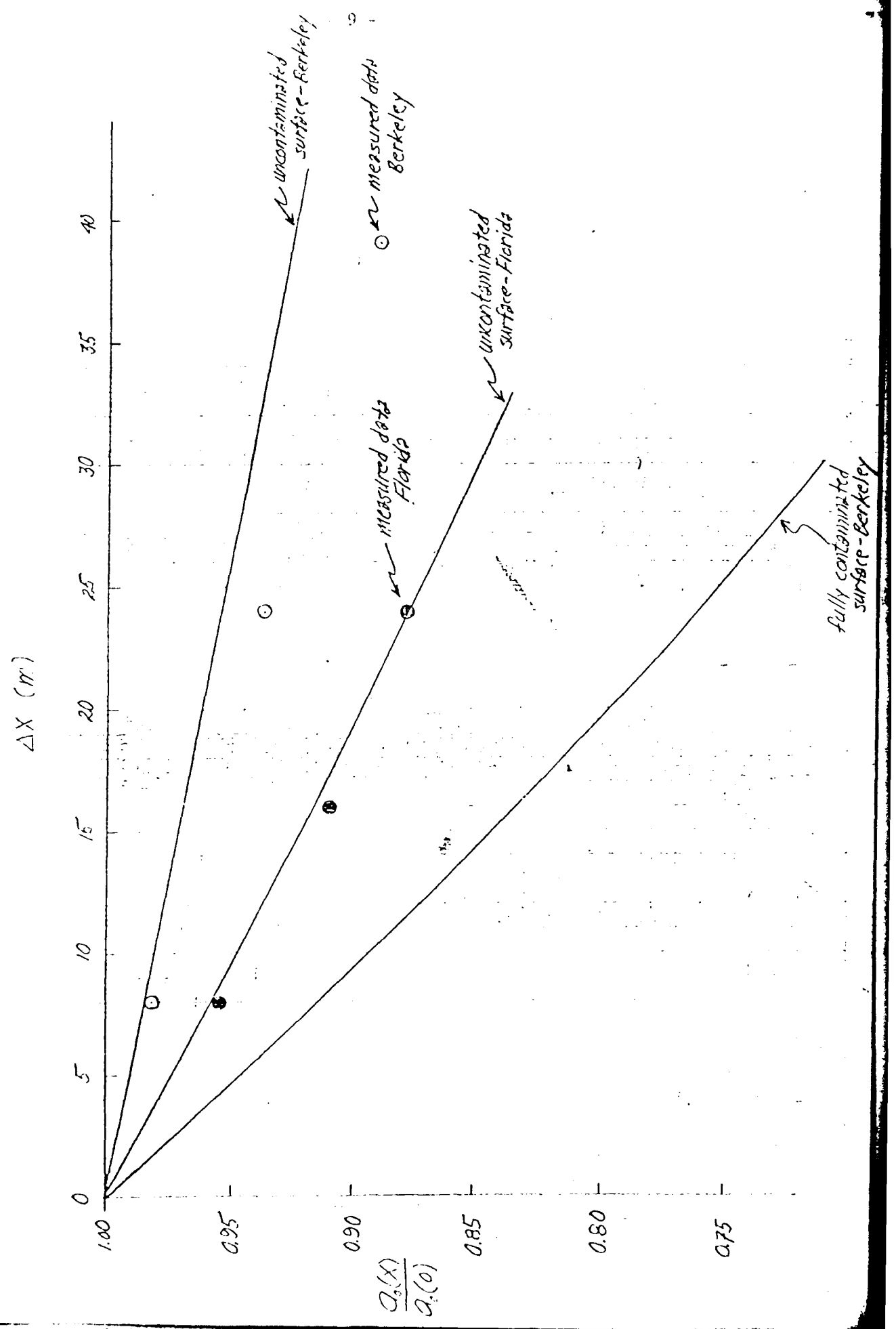
Below each wave trace in figure 1 I have also presented a histogram of the node-to-node wave periods through the wave packet. This rather crude attempt at complex demodulation provides some insight into the wave packet evolution. At the first two stations, local wave periods differ little from the programmed period of 1 sec. However, at the last two stations the leading waves are clearly developing periods up to 15% longer than the 1 sec period of waves near the center of the packet. The origin of the longer wave content is not clear although its emergence at the front of the packet is probably responsible for the changes between measured and predicted packet profiles. The most plausible explanation for the unwanted wave content of the packet is that it is a consequence of imperfect generation by the wave-maker. It is an unfortunate (theoretical and observed) property of short-wave solitons that these nonlinear waves propagate with the linear group speeds of their carrier waves. Hence, unlike their long-wave counterparts, short-wave solitons cannot separate from any background "noise" with the same frequency. (The background noise corresponds to the radiation or non-soliton component of the solution to the nonlinear Schrödinger equation.) The mergence and slow migration (at linear speeds) of the longer wave components in figure 1 may be a manifestation of this phenomenon. In this regard it is important to note that the radiation wave components remain dispersive even at nonlinear order and their amplitudes should decay in time  $t$  with an inviscid decay rate of  $t^{-\frac{1}{2}}$ . Since the inviscid soliton does not decay, when noise is present one expects the measured data to agree better with the theoretical profile with distance (or time) down the tank. Exactly the opposite

behavior is observed in figure 1; however, it must be remembered that growing distortions might still occur until the radiation attains its asymptotic character.

Although inviscid solitons do not decay with time, water-wave solitons are subject to viscous attenuation of their amplitude. Two models for the viscous damping of short-wave solitons have been developed independently by Dr. Harvey Segur and myself (with considerable assistance from N. K. Lin, a graduate student at Berkeley). Both models predict similar results even though the approaches to model development were quite different. Experimental verification of the models must be considered limited for large propagation distances due to the distortion discussed previously; short distance evolution according to these models is verified by the measured data. As in all viscous damping models, contamination of the water surface enters as an empirical coefficient ranging from zero for no contamination to unity for a fully contaminated (and immobile) surface. Theoretical results for these two limiting cases are shown in figure 2 with experimental data for the wave evolution in figure 1. Measurements suggest that some surface contamination is present in the Berkeley data which is expected since water remains in the tank continuously. Theoretical and experimental results for the same initial data observed in the Florida facility are also shown in figure 2. In Florida, well water was pumped to the wave tank immediately prior to the experiments; hence, surface contamination should be less; this expectation is verified by the data. (The narrower tank in Florida leads to greater wave attenuation with distance of propagation.)

It should also be noted that the viscous damping models for envelope solitons indicate that they decay twice as fast as a linear wave train of

Figure 2. Viscous decay of envelope solution



the same frequency. Unfortunately, water wave trains of sufficiently small amplitude were not measured to test this prediction. However, measurements of wave trains with the same degree of nonlinearity as the comparison soliton (prior to the visual onset of Benjamin-Feir instability) indicate that the solitons decay only one-half as rapidly as the uniform wave train.

The evolution of arbitrary packets of initial data was also investigated. An example of results is shown in figures 3a-b at two measurement stations; histograms of wave periods are shown in figures 4a-b for each measurement. The dominant wave packet in the downstream measurement of figure 3b clearly has evolved a soliton profile. The remaining wave packets do not have soliton profiles and represent the radiation component in the initial data. The period histogram of figure 4b clearly shows the linear dispersive nature of the constituent wave components which are rank ordered by their group speed. (Also see Appendix IV).

Experiments on the stability of 2-D envelope solitons to 3-D perturbations have proven to be inconclusive. Very small 3-D effects were measured in some experiments but without a consistency or magnitude sufficient to infer definitive behavior patterns. The experiments did highlight a deficiency in the analytical studies on this aspect of envelope soliton. All explicit criteria which provide definitive predictions on the tank (or crest) widths necessary for instability assume infinite water depths. However, the nonlinear description of these waves contains terms which decay algebraically--not exponentially--with depth. Hence, it is dangerous to apply these criteria to finite depth experiments, even for  $kh \sim 10$ .

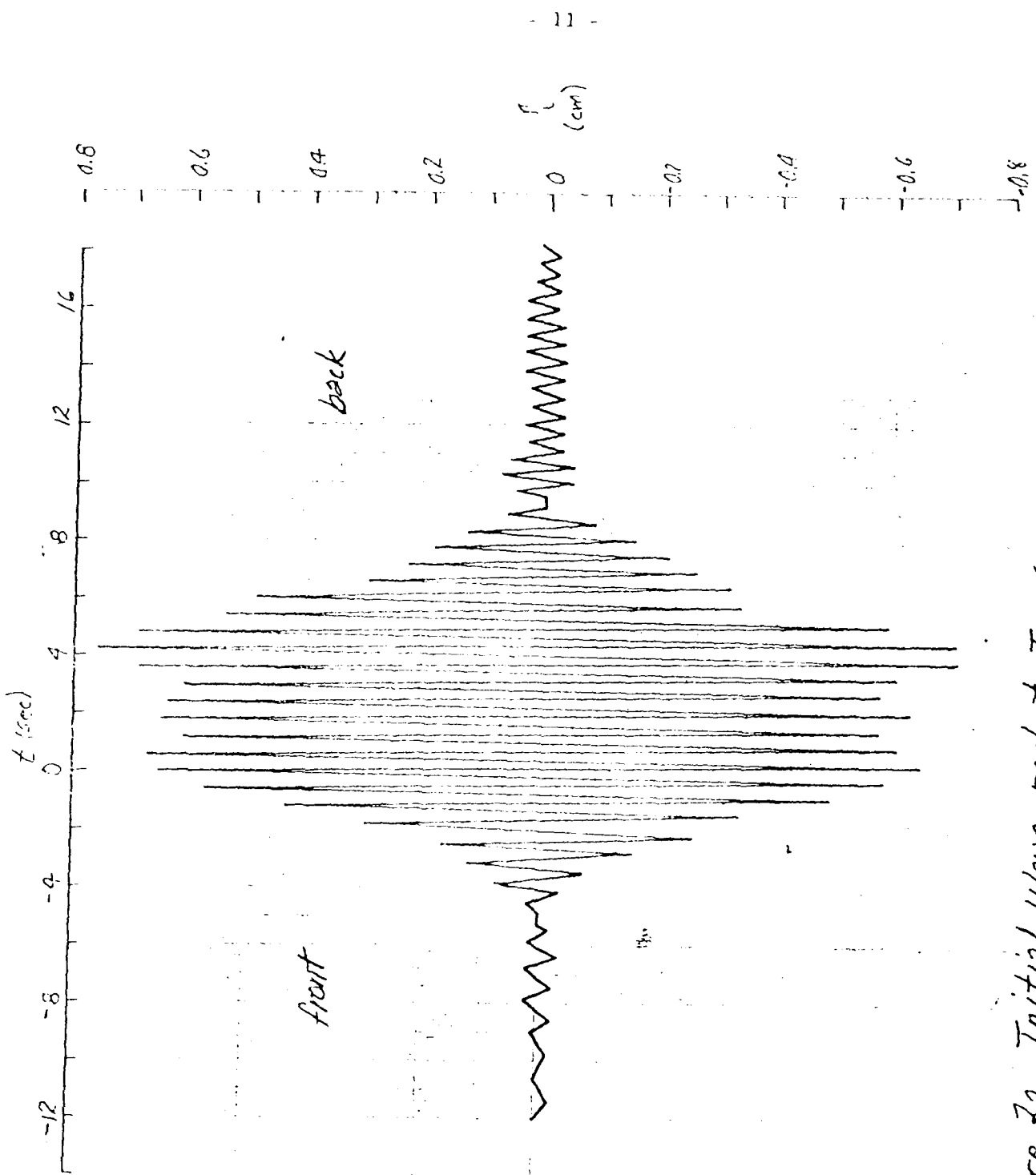


Figure 32. Initial wave packet.  $T = 0.6$  sec.

$X = 6$  m

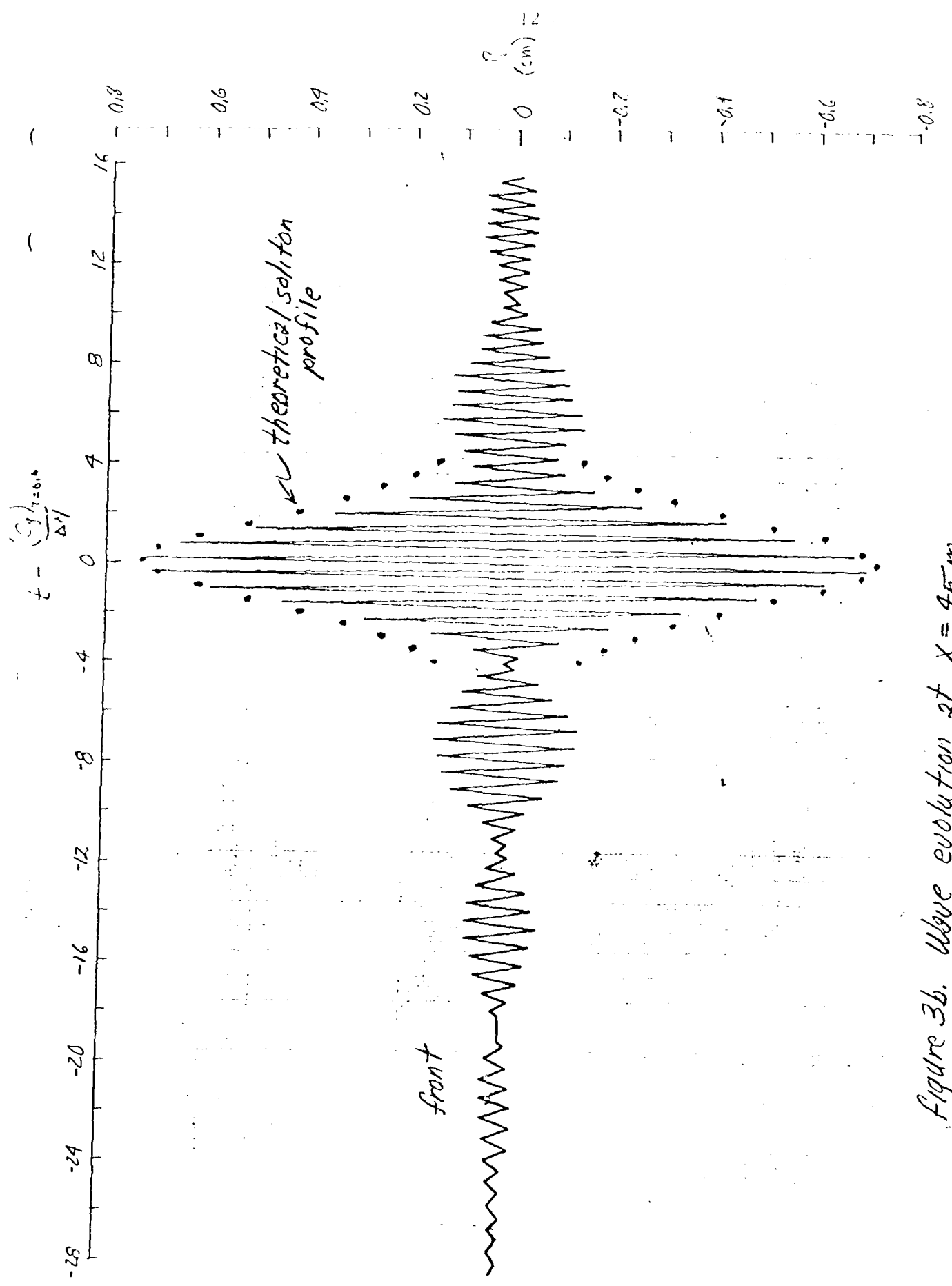


Figure 3b. Wave evolution at  $X = 45\text{ m}$ .

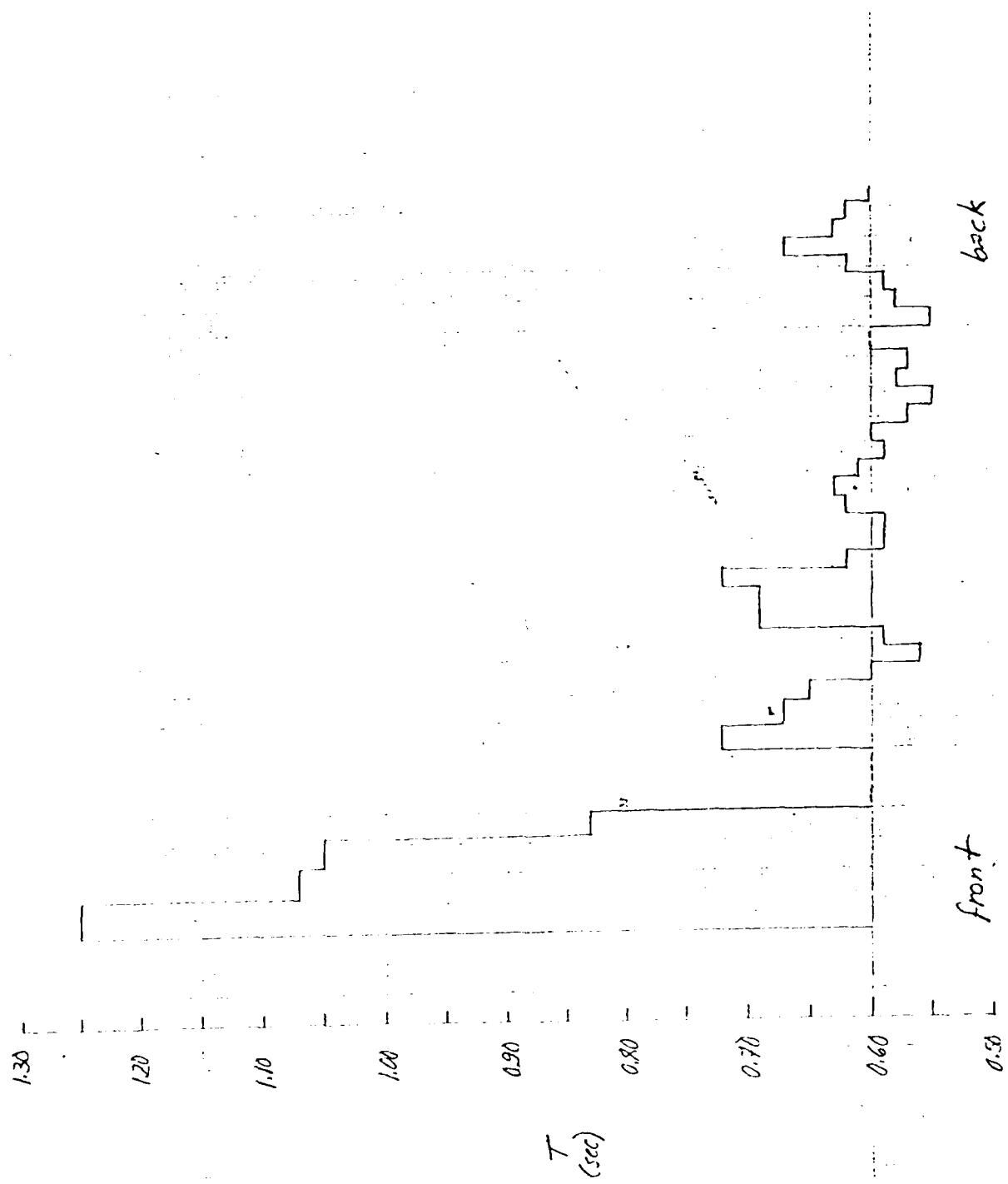


Figure 4a. Periodogram for wave packet of figure 3a

$x = 6 m$

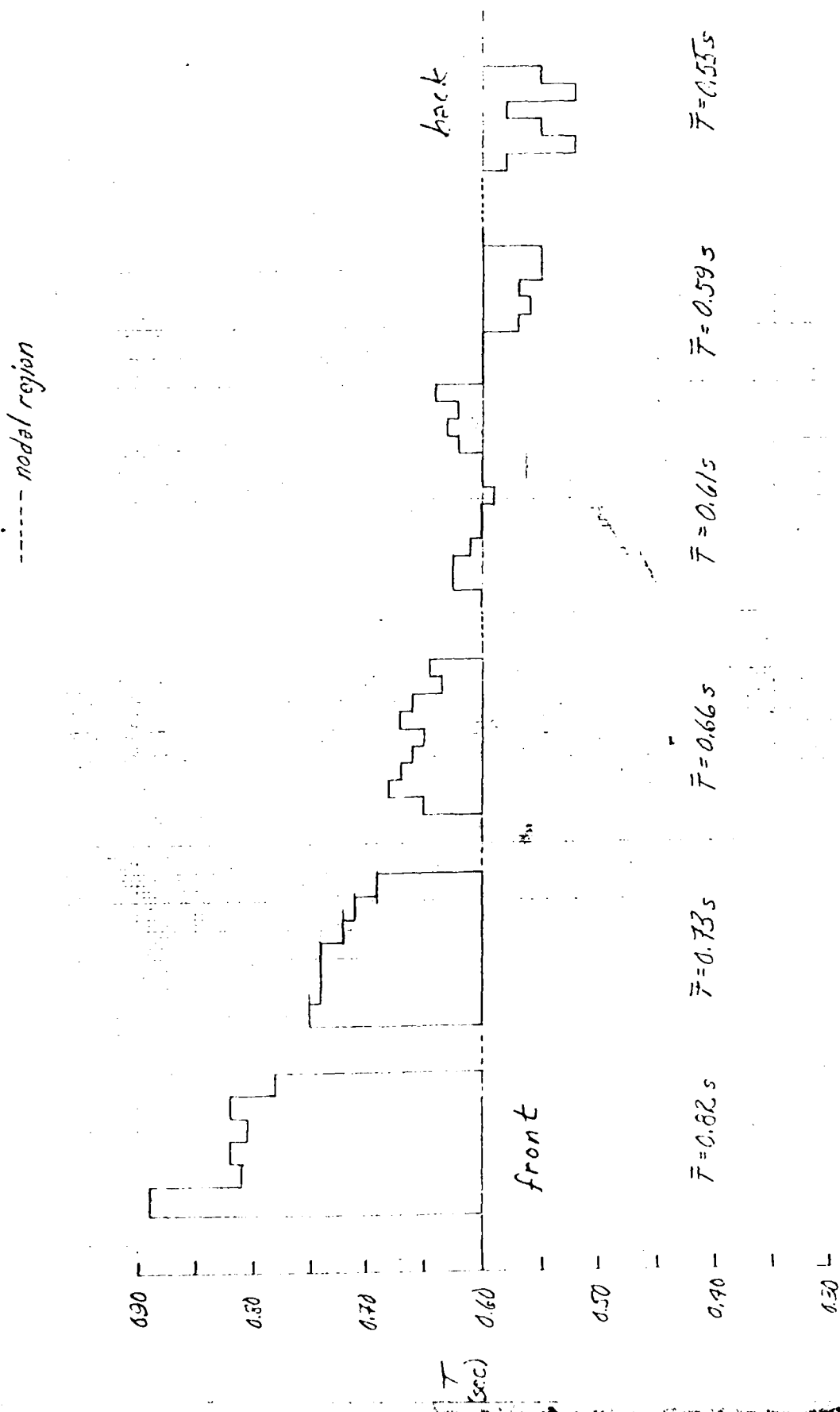


figure 4b. Periodogram for wave system of figure 36  
 $\frac{\bar{T}}{\bar{x}} = 1.5$  average packet carrier wave period

Finally, based on the data presented here as well as many other experiments on varying aspects of short-wave solitons, it is clear to me that the reality of these systems is more difficult to disentangle than that of their long-wave counterparts. However, even with the confusion arising from microscopic observation of these waves, it is also apparent that the macroscopic structure predicted by the nonlinear Schrödinger equation is present. All of these results emphasize the need for more analytical study coupled with delicate experiments capable of yielding quantitative measurement of third order (and higher) parameters.

Appendix II

Baroclinic Tsunami Generation  
(To appear in *Journal of Physical  
Oceanography*, September, 1980.)

## Baroclinic Tsunami Generation

JOSEPH L. HAMMACK

*Department of Civil Engineering, University of California, Berkeley 94720*

(Manuscript received 13 August 1979, in final form 2 May 1980)

### ABSTRACT

An analytical and experimental study of the baroclinic waves generated by a monopole dislocation of the sea floor is presented. Analytical results are based on a two-dimensional and linearized description of motion using a two-layer approximation for density variation; experiments utilize a stratification with finite (nonzero) pycnocline thickness. Scaling parameters which characterize the generation process and the potential role of nonlinear effects are discussed. It is shown that the barotropic modes are not affected by the small differences in potential density typical of ocean stratifications and all previous results for these waves are applicable. The two-layer approximation is found to provide an accurate representation of the (long) baroclinic waves typical of tsunamis. Like the barotropic response, baroclinic generation is impulsive and linear resulting in wave amplitudes proportional to the vertical offset of the sea floor. Near the generation region barotropic waves have amplitudes of one-half the sea floor displacement while the baroclinic waves are attenuated further by the ratio  $h_1/h$ , where  $h$  is the total fluid depth and  $h_1$  the upper layer thickness. Although Coriolis effects are not included in either the analytical or experimental models, these effects may often be significant for baroclinic waves. In general, the potential role of Coriolis forces is both earthquake and site specific. Regardless, the analysis herein remains applicable for times smaller than the local inertial period.

### 1. Introduction and major conclusions

Tsunami research to date has generally focused on the waves at the ocean's surface, ignoring vertical variations in potential density which typically exist. Submarine earthquakes which produce significant surface (barotropic) waves will also generate internal (baroclinic) tsunamis in stratified regions. These baroclinic modes were examined first by Cherkesov (1968) who presented a theoretical investigation of waves generated by a motion of the sea floor in an ocean with an exponential increase in potential density with depth. Subsequently, Fedosenko and Cherkesov (1968) presented similar results for a two-layer stratification which is more representative of actual ocean conditions. Solutions were based on a linearized description of motion for both two-dimensional and three-dimensional (axisymmetric) source regions; Coriolis forces were neglected. In both presentations, the integral solutions were evaluated only for the far-field at large distances from the source region. These results showed that a displacement of the sea floor produced (fast) barotropic waves and (slow) baroclinic waves which separated with time. Each wave system induced a coupled motion at the opposite interface. It was further claimed that the asymptotic amplitudes of the internal waves could exceed those at the free surface by a factor of 25 for ocean conditions. Neither the relevance of asymptotic linear analysis to actual tsunamis nor any limitation of the results due to omission of Coriolis forces were discussed by the authors. [Hammack and Segur (1978) have shown that linear asymptotic solutions never become applicable for barotropic tsunamis.]

The objective of the present paper is to examine the near-field behavior of baroclinic waves generated by vertical motions of the sea floor. Both analytical and experimental results are presented for a simple model of generation consisting of a block upthrust (or downthrow) according to a prescribed time-displacement history. Analytical results are based on a two-layer stratification of potential density while the experiments utilize a stratification with finite (nonzero) pycnocline thickness.

The organization of this paper and some of the major results are as follows. In Section 2 a brief description of tsunamigenic earthquakes is presented and the model to be examined herein is introduced. Nondimensional parameters which characterize the generation process are discussed in Section 3 where it is shown that the generation process of actual tsunamis is impulsive and linear for both the barotropic and baroclinic response. In Section 4 the linear solution for the baroclinic model is developed and other well-known properties of long internal waves at the interface of two liquids are reviewed. In the Boussinesq limit of small density differences, it is shown that the barotropic response is not affected by the stratification. In addition, both barotropic and baroclinic tsunamis have initial shapes similar to the permanent deformation of the sea floor. The maximum amplitude of the surface wave is one-half the vertical displacement of the sea floor while the maximum amplitude of the internal wave is additionally attenuated by the ratio of upper layer depth to total depth. Experimental equipment and procedures are described in Section 5 and theoretical results are compared with the experimental measurements in Section 6. Results indicate that the maximum amplitudes of the barotropic and baroclinic waves near a source region may be represented by a single (and simple) functional relation over the full range of their respective generation time scales (see Fig. 10). The potential role of Coriolis effects for baroclinic waves is discussed in Section 7, where it is demonstrated that time scales of baroclinic modes can at may often approach the inertial period.

## 2. Tsunamigenic earthquakes and the proposed model

Most large tsunamis are associated with sub-oceanic earthquakes, centered near plate margins, during which significant *vertical* offset of the sea floor occurs. In order to determine the waves generated by mechanisms of this type, a knowledge of the water depths, stratification and latitude at the source site as well as the spatial and temporal distributions of the sea floor dislocation is required. Since the objective herein is to delineate fundamental relations between the generation mechanism and wave structure, we seek a tractable model which embodies essential source parameters in a simple way. With this goal in mind we will assume a uniform depth  $h$  in the generation region and adopt a two-layer model to represent the ambient stratification in potential density. In addition we will neglect Coriolis forces (and their latitude dependence); limitations of the results due to this omission will be discussed *a posteriori*. Before introducing further simplifications, a brief description of features common to tsunamigenic earthquakes and their (dimensional) scales is presented.

It is both convenient and appropriate to define the source size of the tsunami (and earthquake) as the area affected by aftershocks immediately following the generative earthquake. This area is typically elongated and elliptical in shape with the ruptured portion of the fault joining the foci of the ellipse. Early efforts to correlate the source area  $S$  with Richter magnitude  $M_s$  proved unsatisfactory due to the marked scatter in the data. Kanamori and Anderson (1975) *inter alios* have shown that definitive correlations exist between  $S$  ( $\text{km}^2$ ) and the seismic moment  $M_0$  ( $\text{dyn cm}$ ). Representative values based on their results for interplate earthquakes are shown in Table 1. In order to provide perspective, it is still desirable to relate the seismic moment to Richter magnitude. As expected, results here are less definitive and no single empirical relation exists; however, Kanamori and Anderson (1975) do present correlations for three classes of earthquake magnitudes. Approximate values of  $M_s$  based on their results are shown in Table 1. As a first approximation, we may assume that the source areas of Table 1 represent regions of monopole vertical offset (upthrust or downthrow). With this simplification the source size can be characterized by a single length dimension  $L \sim S^{1/2}$ ; representative values are shown in Table 1. If we further assume the static and seismic moments are equal, magnitudes of the average (and permanent) vertical offset  $\zeta_0$  can be found by

$$|\zeta_0| \approx M_0/\mu S,$$

where  $\mu$  is the shear modulus (rigidity) of the fractured medium. Estimates of  $|\zeta_0|$  with  $\mu = 5 \times 10^{11}$  dynes  $\text{cm}^{-2}$  are presented in Table 1. The temporal history of the sea floor dislocation is characterized by a minimum of two time scales: a time  $t_c$  corresponding to the time required for the vertical offset to occur at a specific spatial location and a time  $t_R$  representing the period required for the rupture to propagate along the fault. Empirical results of Kanamori and Anderson (1975) suggests that  $t_R \sim 10t_c$  for tsunamigenic earthquakes ( $M_s \geq 6.5$ ) with estimates of the rupture time ranging from  $t_R \sim 10$  s for moderate earthquakes to  $t_R \sim 100$  s for earthquakes with fault lengths exceeding 100 km (based on rupture speeds  $V_R \sim L/t_R \sim 2-3$   $\text{km s}^{-1}$ ). As suggested previously, vertical offset is primarily responsible for tsunami generation; hence, the time  $t_c$  is most relevant for subsequent scaling.

In light of the above description, we will adopt the following simplifications for the generation model. First, the smallness of the linear source dimensions of Table 1 relative to the earth's radius permits a plane-earth approximation. Second, for monopole and uniform vertical offset, the elongation of the source dimension suggests that initial propagation of waves near the center of the source region is one-dimensional and normal to the fault. Hence, we arrive at the simple generation model shown in Fig. 1. The actual sea floor displacement used in computations is given by

$$\zeta(x,t) = \zeta_0(e^{-\alpha t} - 1)H(b^2 - x^2), \quad (1)$$

where  $H$  represents the Heavyside stepfunction. In the dislocation of (1), we have taken  $2b \approx L$  and, for experimental convenience, we will take

$$t_c = \frac{1.11}{\alpha}. \quad (2)$$

Physically,  $t_c$  represents the time required for two-thirds of the vertical offset to occur.

### 3. Scaling the generation process and a comment on nonlinearity

In order to provide a rational basis for choosing computational examples, nondimensional parameters which characterize generation and typical magnitudes for tsunamigenic earthquakes are required. With this objective in mind, a brief review of results by Hammack (1973) for generation of barotropic waves is useful. Three nondimensional parameters are required to characterize barotropic generation for simple models similar to that discussed in Section 2: an amplitude scale,  $|\zeta_0|/h$ ; a size scale,  $b/h$ ; and  $\tau = t_c C_1/b$  termed a time-size ratio where  $C_1 = (gh)^{1/2}$  is the speed of long barotropic modes. [Alternatively,  $\tau$  may be considered an inverse Froude number analogous to that used by Noda (1970) for landslide-generated waves.] The generation process may be classified according to the time-size ratio as impulsive for  $\tau \ll 1$ , creeping for  $\tau \gg 1$  and transitional for  $\tau \approx 1$ . The specific range of  $\tau$  for each classification is only a weak function of the size scale with the transitional regime essentially disappearing for large size scales ( $b/h \gg 1$ ). The amplitudes of waves propagating out of the generation region for an impulsive motion are proportional to the bed displacement ( $\eta \propto \zeta_0$ ) where the constant of proportionality depends only on the size scale. For  $b/h > 1$ , this constant attains its maximum value of one-half and the tsunami near the source region is similar in shape to the permanent deformation of the sea floor. For creeping bed motions, wave amplitudes are reduced in inverse proportion to the magnitude of the time-size ratio ( $\eta \propto \zeta_0/\tau$ ). Nonlinear effects become significant when generation is impulsive and  $|\zeta_0|/h \geq 0.2$ . Assuming depths in the generation region of  $h \approx 200$  m on the shelf and  $h \approx 4000$  m in deep water, size scales for tsunamigenic earthquakes are typically large (based on the lengths  $L \sim b$  given in Table 1); hence, energy is concentrated at long wavelengths. In addition, amplitude scales are small based on values of  $|\zeta_0|$  given in Table 1. Finally, using characteristic times up to  $t_c \sim 10$  s, the barotropic response is typically impulsive ( $\tau \ll 1$ ). Based on these characteristic values, the barotropic response is expected to be linear and the wave structure near the source region should resemble the permanent deformation of the sea floor with a 50% attenuation in amplitude. It is noteworthy, and fortunate, that the barotropic response is represented by the simplest possible limiting conditions of the generation parameters.

An examination of the independent variables  $(\rho_1, \rho_2, h_1, h_2, b, t_c, \zeta_0, g)$  for generation in a two-layer ocean (see Fig. 1) indicates that five nondimensional parameters are required to characterize generation. A possible parameter choice for small density differences is

$$\begin{aligned} & b/h \\ & |\zeta_0|/h \\ & \tau_1 = t_c C_1/b = t_c (gh)^{1/2}/b \\ & \tau_2 = t_c C_2/b = t_c (\epsilon gh_1 h_2/h)^{1/2}/b \\ & (h_1/h_2)^{-1} \end{aligned} \quad (3)$$

where  $h = h_1 + h_2$  and  $\epsilon = (\rho_2 - \rho_1)/\rho_2 \ll 1$ . Of these five parameters, the first four preserve the scaling characteristics of the barotropic mode and indicate the expectation of a similar role for a time-size ratio ( $\tau_2$ ) based on the internal (long) wave speed  $C_2$  (see Section 4). Notice that the two time-size ratios satisfy  $\tau_2/\tau_1 = O(\epsilon^{1/2})$ ; hence, bed motions which are classified creeping for the surface response ( $\tau_1 \gg 1$ ) may be impulsive for the interfacial response ( $\tau_2 \ll 1$ ). Since  $\tau_1 < 1$  for prototype tsunamis, the baroclinic response is always impulsive.

The fifth parameter  $[(h_1/h_2) - 1]$  is geometric in nature; the various roles of this parameter and its related forms  $h_1/h$  or  $h_2/h$  will appear in Sections 4 and 6. Its specific role as an indicator of the strength of nonlinear effects during generation can be established as follows. In a two-layer system, nonlinear effects may occur for both the surface and interfacial motion. For the free motion of long internal waves in a two-layer system with small density differences and uniform depth, it can be shown (see Keulegan, 1953) that the appropriate measure of small but finite nonlinearity is  $|\eta_2(h_1 - h_2)/h_1 h_2|$ . It will be demonstrated in Section 4 that  $\eta_2 \propto \zeta_0(h_1/h)$  for impulsive generation; hence, nonlinearity is measured by the parameter  $[(\zeta_0/h)(h_1/h_2 - 1)]$ . Since  $h_1/h_2 \leq 1$  for typical ocean stratifications and  $(\zeta_0/h)$  is small, both barotropic and baroclinic free motions are linear initially.

#### 4. Theoretical analysis

We consider a two-dimensional ocean as shown in Fig. 1 consisting of two fluid domains  $D_1$  and  $D_2$  bounded above by a free surface  $S_f$ , below by a solid boundary  $S_b$  and contacting at a liquid-liquid interface  $S_i$ . Both fluid regions are unbounded in the direction  $x$  of wave propagation. The upper and lower fluids have densities  $\rho_1$  and  $\rho_2$ , respectively, and are gravitationally stable ( $\rho_1 < \rho_2$ ). Initially, the two fluids are at rest with uniform depths  $h_1$  and  $h_2$ . Subsequently ( $t > 0$ ), the solid boundary  $S_b$  is permitted to move in a prescribed manner given by  $y = -h_2 + \zeta(x, t)$ , where  $\zeta(x, t)$  is given by (1). The resulting motion of the free surface  $\eta_1(x, t)$  and interface  $\eta_2(x, t)$  are required. Since both motions are probably linear for prototype tsunamis, a first-order (linear) description of motion is employed from the outset.

Assuming the fluids in each domain to be incompressible and their motion irrotational, velocity potentials  $\phi_1(x, y, t)$  and  $\phi_2(x, y, t)$  exist for  $D_1$  and  $D_2$ , respectively. Conservation of mass requires

$$\nabla^2 \phi_1 = 0 \quad \text{in } D_1, \quad (4a)$$

$$\nabla^2 \phi_2 = 0 \quad \text{in } D_2, \quad (4b)$$

where  $\nabla^2$  is the Laplacian operator. Assuming the fluids to be inviscid, the kinematic boundary conditions at each surface are

$$\phi_{1y} = \eta_{1y} \quad \text{on } y = h_1, \quad (5a)$$

$$\phi_{2y} = \eta_{2y} \quad \text{on } y = 0. \quad (5b)$$

By further neglecting surface energy at  $S_f$ , the condition for constancy of pressure across and along the free surface is

$$\phi_{1y} + g\eta_1 = 0 \quad \text{on } y = h_1. \quad (6a)$$

(The hydrostatic pressure  $\rho_1 gh_1$  has been adsorbed into  $\phi_1$ .) Continuity of pressure across  $S_i$  requires

$$\phi_{2y} + g\eta_2 = \frac{\rho_1}{\rho_2} (\phi_{1y} + g\eta_1) \quad \text{on } y = 0. \quad (6b)$$

The kinematic condition at the solid boundary is

$$\phi_{2y} = \zeta_t \quad \text{on } y = -h_2, \quad (7)$$

where it is assumed that motion of the solid boundary is not affected by fluid motion.

Combining the kinematic and dynamic boundary conditions at  $S_f$  and  $S_i$  yields

$$\phi_{1yy} + g\phi_{1y} = 0 \quad \text{on } y = h_1, \quad (8)$$

$$\phi_{2yy} + g\phi_{2y} = \frac{\rho_1}{\rho_2} (\phi_{1yy} + g\phi_{1y}) \quad \text{on } y = 0. \quad (9)$$

Using the Laplace transform in  $t$  and the Fourier transform in  $x$ , Eqs. (4), (8), (9) and (7) become

$$\tilde{\phi}_{1yy} - k^2 \tilde{\phi}_1 = 0 \quad \text{in } D_1, \quad (10a)$$

$$\tilde{\phi}_{2yy} - k^2 \tilde{\phi}_2 = 0 \quad \text{in } D_2, \quad (10b)$$

$$s^2 \tilde{\phi}_1 + g\tilde{\phi}_{1y} = 0 \quad \text{on } y = h_1, \quad (10c)$$

$$s^2 \tilde{\phi}_2 + g\tilde{\phi}_{2y} = \frac{\rho_1}{\rho_2} (s^2 \tilde{\phi}_1 + g\tilde{\phi}_{1y}) \quad \text{on } y = 0, \quad (10d)$$

$$\tilde{\phi}_{2y} = s\tilde{\zeta} \quad \text{on } y = -h_2, \quad (10e)$$

where the tilde of a function  $f(x, t)$  indicates

$$\bar{\eta}_1 = \frac{\bar{\zeta} s^4}{\theta \cosh kh_1 \cosh kh_2}, \quad (17a)$$

$$\bar{\eta}_2 = \frac{\bar{\zeta}}{\theta \cosh kh_2} [s^4 + s^2 gk T_1]. \quad (17b)$$

The transform of the bed motion given by (1) is

$$\bar{\zeta}(k, s) = 2\zeta_0 \frac{\sin kb}{k} \left[ \frac{\alpha}{s(s + \alpha)} \right]. \quad (18)$$

Substituting (18) into (17), performing the integration around the Bromwich contour, taking only the real part and noting that the integrands are even functions of  $k$ , the free surface and interfacial waves are found to be

$$\eta_1(x, t) = \int_0^{\infty} \frac{B_1 B_2}{\cosh kh_1 \cosh kh_2} \times [e^{-\alpha t} - B_3 B_4 + B_5 B_6] dk, \quad (19a)$$

$$\eta_2(x, t) = \int_0^{\infty} \frac{B_1 B_2}{\cosh kh_2} \left[ \left( 1 + \frac{gk T_1}{\alpha^2} \right) e^{-\alpha t} - \left( 1 - \frac{gk T_1}{\omega_1^2} \right) B_3 B_4 + \left( 1 - \frac{gk T_1}{\omega_2^2} \right) B_5 B_6 \right] dk, \quad (19b)$$

with

$$B_1 = \frac{-2\zeta_0 \sin kb \cos kx}{\pi k [1 + (\rho_1/\rho_2) T_1 T_2]}, \quad (20a)$$

$$B_2 = \frac{\alpha^4}{(\alpha^2 + \omega_1^2)(\alpha^2 + \omega_2^2)}, \quad (20b)$$

$$B_3 = \frac{\omega_1^2 (\alpha^2 + \omega_2^2)}{\alpha^2 (\omega_1^2 - \omega_2^2)}, \quad (20c)$$

$$B_4 = \cos \omega_1 t + \frac{\omega_1}{\alpha} \sin \omega_1 t, \quad (20d)$$

$$B_5 = \frac{\omega_2^2 (\alpha^2 + \omega_1^2)}{\alpha^2 (\omega_1^2 + \omega_2^2)}, \quad (20e)$$

$$B_6 = \cos \omega_2 t + \frac{\omega_2}{\alpha} \sin \omega_2 t, \quad (20f)$$

and  $\omega_i^2$  ( $i = 1, 2$ ) are the roots of the dispersion relation

$$(1 + \rho_1/\rho_2 T_1 T_2) \omega^4 - gk(T_1 + T_2) \omega^2 + \epsilon(gk)^2 T_1 T_2 = 0, \quad (21)$$

given by

$$\omega_{1,2}^2 = gk \left\{ \frac{(T_1 + T_2) \pm \sqrt{(T_1 + T_2)^2 - 4\epsilon(1 + \rho_1/\rho_2 T_1 T_2) T_1 T_2}}{2(1 + \rho_1/\rho_2 T_1 T_2)} \right\}. \quad (22)$$

(Note that  $\omega = -is$  in the above analysis.) Eq. (21) is well known for two-layer systems with  $\omega_1^2$  corresponding to the barotropic modes and  $\omega_2^2$  corresponding to the baroclinic modes (see e.g. 1 and 1932, p. 372).

||||||||||||||||||||||||||||||||||||||||||||||||||||

$$\tilde{f}(k, s) = \int_{-s}^s dx \int_{-s}^s e^{ikx} e^{-st} f(x, t) dt. \quad (11)$$

The function  $f(x, t)$  is recovered from (11) by inverting the Laplace and Fourier transforms, i.e.,

$$f(x, t) = \frac{1}{2\pi} \int_{-s}^s dk \times \left[ \lim_{r \rightarrow s} \frac{1}{2\pi i} \int_{\mu - ir}^{\mu + ir} e^{-ikx} e^{st} \tilde{f}(k, s) ds \right], \quad (12)$$

using the complex inversion integral for the Laplace transform. The transformed surface and interfacial waves are

$$\bar{\eta}_1 = -\frac{s}{g} \bar{\phi}_1 \quad \text{on} \quad y = h_1, \quad (13a)$$

$$\bar{\eta}_2 = \frac{s}{\epsilon g} [(\rho_1/\rho_2) \bar{\phi}_1 - \bar{\phi}_2] \quad \text{on} \quad y = 0. \quad (13b)$$

Solution of (10a,b) yields

$$\bar{\phi}_1(k, y, s) = A_1 \cosh ky + A_2 \sinh ky, \quad (14a)$$

$$\bar{\phi}_2(k, y, s) = A_3 \cosh ky + A_4 \sinh ky, \quad (14b)$$

and the coefficients  $A_i = A_i(k, s)$  with  $i = 1, 4$  are found from Eqs. (10c)–(10e) to be

$$A_1 = \frac{-\bar{\zeta} s^3}{\theta k \cosh kh_2} [s^2 T_1 + gk], \quad (15a)$$

$$A_2 = A_4 = \frac{s^3 \bar{\zeta}}{\theta k \cosh kh_2} [s^2 + gk T_1], \quad (15b)$$

$$A_3 = \frac{-s \bar{\zeta}}{\theta k \cosh kh_2} [s^4 \rho_1 T_1 + s^2 gk + \epsilon(gk)^2 T_1], \quad (15c)$$

with

$$\theta = s^4 \left( 1 + \frac{\rho_1}{\rho_2} T_1 T_2 \right) + s^2 (T_1 + T_2) gk + \epsilon(gk)^2 T_1 T_2, \quad (16a)$$

$$T_i = \tanh kh_i, \quad i = 1, 2. \quad (16b)$$

Finally, the transformed free surface and internal waves are found from (13) to be

Although the Fourier integral solutions given by (19) are algebraically complex and the wave structure is difficult to see, it is easily shown that these solutions contain more familiar results. For example, in the Boussinesq limit of small density differences ( $\epsilon \rightarrow 0$ ) we find

$$\eta_1 - \eta = \frac{\zeta_0}{\pi} \int_0^\infty \frac{\cos kx \sinh kb}{k \cosh kh} \left( \frac{\alpha^2}{\alpha^2 + \omega^2} \right) \times \left( e^{-\omega t} - \cos \omega t - \frac{\omega}{\alpha} \sin \omega t \right) dk, \quad (23)$$

$$\omega_1^2 \sim \omega^2 \equiv gk \tanh kh, \quad (24)$$

where  $\eta$  is the solution found by Hammack (1973) for a barotropic ocean. Hence, the surface waves in a two-layer system are not affected by the stratification in the Boussinesq limit. Since density differences are typically small for oceans ( $\epsilon \approx 0.002$ ), previous results for surface waves in a barotropic ocean are applicable to leading order.

It is also useful to approximate specific properties of the internal and surface waves for long modes such that

$$\epsilon \equiv \frac{\Delta \rho}{\rho_2} = O(kh_1) = O(kh_2) \ll 1. \quad (25)$$

Under these conditions the well-known phase speeds of the surface and internal waves are found [from Eq. (22)] to be, respectively,

$$C_1^2 = \omega_1^2/k^2 = gh \left[ 1 - \epsilon \frac{h_1 h_2}{h_2} + O(\epsilon^2) \right], \quad (26a)$$

$$C_2^2 = \omega_2^2/k^2 = g\epsilon \frac{h_1 h_2}{h} [1 + O(\epsilon^2)]. \quad (26b)$$

The significant difference in phase speeds for these long waves,  $C_2/C_1 = O(\epsilon^{1/2})$ , suggests that even though the surface and internal waves overlap spatially near the generation region, they will separate rapidly and nonlinear interactions between the two systems will not have time to become significant.

In addition to the phase speeds it is also of interest to examine the amplitude of the motion induced by each wave system at the opposite interface. Following Keulegan (1953), normal-mode analysis suggests that

$$\beta_2 = \frac{h_2}{h} N_1, \quad (27a)$$

$$\beta_1 = -\epsilon \frac{h_2}{h} N_2, \quad (27b)$$

where  $\beta_2$  is the coupled motion of the interface due to a wave  $N_1$  at the free surface and  $\beta_1$  is the coupled motion of the free surface due to an internal wave  $N_2$ . Here, the waves  $N_1$  and  $N_2$  represent the independent modes at the free surface and interface, respectively. (Note that  $N_1 = \eta_1$  and  $N_2 = \eta_2$  when the surface and internal waves do not overlap spatially.) The motion  $\beta_2$  is barotropic and would exist at the interface location even if the fluid was not stratified.

In order to see the wave structure in (19), numerical solutions at  $x = b$  for both barotropic and baroclinic waves propagating from the source region are shown in Fig. 2. Results are presented for impulsive response at the free surface and interface (Fig. 2a) and for impulsive interfacial response with creeping free surface response (Fig. 2b). Magnitudes of the nondimensional generation parameters used in computations for Fig. 2a are chosen to be asymptotically representative of prototype phenomena; dimensional quantities correspond to experiments which will be discussed in Section 5.

As expected, the surface waves do not appear to vary with layer-depth ratio in Fig. 2. In fact these results are identical to those for a homogeneous ocean computed by (23) except for a small residual lowering of the water level which persists until the internal wave passes. It should be emphasized that surface and internal waves overlap spatially in the generation region; hence, these results represent a linear combination of both the independent ( $N$ ) and induced motions ( $\beta$ ) at the interface and free surface. The residual lowering of the free surface is the  $O(\epsilon)$  motion  $\beta_1$  [see Eq. (27b)] induced by the internal wave. In fact, this induced motion differs for each depth ratio; however, the small differences are not discernable at figure scale. The impact of the surface wave at the interface,  $\beta_2$ , is more pronounced and clearly evident in Fig. 2a. This induced motion is easily estimated from (27a) using the free surface solution [since  $N_1 = \eta_1 + O(\epsilon)$ ]. When  $\beta_2$  is eliminated from the internal wave computations,  $N_2$  results and is also shown in Fig. 2a. The leading waves of the independent internal and surface modes are similar to the permanent deformation of the sea floor. The maximum amplitude of the surface wave is one-half the sea floor uplift, i.e.,  $(N_1)_{\max} = \zeta_0/2$ , as found previously for a homogeneous ocean. The maximum amplitude of the independent internal waves  $(N_2)_{\max}$  for these impulsive motions appears to vary with the layer-depth ratio according to

$$(N_2)_{\max} = (h_1/h)(N_1)_{\max} = (\zeta_0/2)(h_1/h). \quad (28)$$

This important result and further clarification of the effects produced by varying the size scale  $b/h$  as well as relative thickness of the upper layer may be established in the following manner. Restricting attention to (mathematically) impulsive bed motions, the initial ( $t = 0^+$ ) amplitudes at  $x = b$  can be evaluated in closed form to yield in the Boussinesq limit

$$\eta_1(b, 0^+) = \frac{2\zeta_0}{\pi} \arctan \left( \tanh \frac{\pi}{2} \frac{b}{h} \right), \quad (29)$$

$$\eta_2(b, 0^+)$$

$$= \frac{\zeta_0}{\pi} \arctan \left[ \sinh(\pi b/h) / \cos \left( \frac{\pi}{2} \frac{h_1}{h} \right) \right]. \quad (30)$$

The result for the surface wave (29) is identical to that for a homogeneous ocean (Sells, 1965) and clearly shows that  $\eta_1 \sim N_1 \sim \eta \sim \zeta_0/2$  for  $b/h > 1$ . Eqs. (29) and (30) are shown in Fig. 3 as a function of  $b/h$  and  $h_1/h$ . [Note that (29) and (30) are equivalent when  $h_1/h \rightarrow 0$ .] Results for the internal wave are identical to the surface wave for  $b/h > 1$  regardless of the layer-depth ratio. For  $b/h < 1$ , the internal wave amplitude exceeds that at the free surface as  $h_1/h$  increases (e.g.,  $h_1/h > 0.25$ ). In all cases, the amplitudes become inversely proportional to the size scale as  $b/h$  decreases. Noting that  $N_2(b, 0^+) = \eta_2(b, 0^+) - \beta_2(b, 0^+)$ , where  $\beta_2$  is given by (27a), Eqs. (29) and (30) may be used to determine the behavior of the internal mode with size scale; the result is

$$N_2(b, 0^+) = \frac{\zeta_0}{\pi} \left\{ \arctan \left[ \frac{\sinh(\pi b/h)}{\cos \left( \frac{\pi}{2} \frac{h_1}{h} \right)} \right]^{-2} \left( \frac{h_2}{h} \right) \times \arctan \left[ \tanh \left( \frac{\pi}{2} \frac{b}{h} \right) \right] \right\}. \quad (31)$$

For  $b/h > 1$ , Eq. (31) yields, in closed form, the numerical results found previously for the internal wave amplitude given by (28). Hence, even though the free surface and interface are lifted (lowered) the same amount by an impulsive bed motion with  $b/h > 1$ , part of the potential energy gained at the interface is associated with the barotropic motion  $\beta_2$ . Consequently, the amplitude of the internal wave is less (by the factor  $h_1/h$ ) than that of the surface wave where all of the potential energy gained, to  $O(\epsilon)$ , is available to the barotropic mode.

## 5. Experimental equipment and procedure

A series of experiments was conducted in a laboratory wave tank which is approximately 32 m long, 60 cm deep and 40 cm wide. The tank is equipped at one extremity with a wave generator consisting of a movable bed section (piston) whose time-displacement history is controlled by an electro-hydraulic-servo system. The wave generator can accurately model the bed motion described by (1). Both the wave generator and tank have been described in detail by Hammack (1972).

In order to model the density stratification of Fig. 1, freshwater and brine are used. The miscibility of these fluids produces a finite pycnocline thickness  $\delta$ ; thus, this stratification provides a better test of the two-layer model as a useful approximation for thin pycnocline regions. The tank is stratified by first introducing a layer of freshwater with a depth  $h_1$ . Brine is then introduced beneath the freshwater at ports distributed along the tank bed until a total depth  $h$  is attained. The volume of the reservoir used to mix the brine limits the depth  $h_2$  to a maximum of 10 cm. For the experiments presented herein, the total depth  $h$  is fixed at 15 cm while the depth of the brine is varied with  $h_2 = 5, 7.5$  and 10 cm. A density difference of  $\sim 5\%$  is utilized in all experiments. This difference is sufficiently large to provide stability of the stratification during filling yet sufficiently small to provide an adequate test of analytical results based on small density differences. The length  $b$  of the movable bed section is constant (61 cm) for all experiments. Hence, the experimental size scale,  $b/h = 4.07$ , is sufficiently large for results to be typical of the tsunamigenic case. Density stratifications are measured using a conductivity probe at two locations before and after each series of experiments; typical results are presented in Fig. 4 where  $h_1 = 5$  cm and  $h_2 = 10$  cm. The similarity of initial stratifications at both locations demonstrates the uniformity of this stratification along the wave tank. A thickness  $\delta$  for the pycnocline region is calculated based on the definition

$$\delta = -\Delta\rho \left( \frac{d\rho}{dy} \right)_{\max}^{-1}, \quad (32)$$

yielding initial values of  $\delta_0 = 0.9$  and 1.0 cm and final values of  $\delta_1 = 2.1$  and 1.8 cm for the upstream and downstream positions, respectively. Actual stratifications are qualitatively similar to theoretical solutions of the diffusion equation for an initial density profile with a simple discontinuity at one level. Using this solution  $\{\rho = \rho_1 + \Delta\rho \operatorname{erfc}[y/(4Dt)^{1/2}]\}$  with the initial discontinuity occurring at  $y = 0$ , the characteristic thickness  $\delta$  defined by (32) is related to the diffusion coefficient  $D$  by

$$\delta = (4\pi Dt)^{1/2}. \quad (33)$$

Hence, an apparent diffusion coefficient can be calculated for the time interval of the experiments by

$$D = \frac{1}{4\pi} \left( \frac{(\delta_1)^2 - (\delta_0)^2}{\Delta t} \right). \quad (34)$$

The apparent diffusion coefficients for the measurements of Fig. 4 are  $D = 2.3 \times 10^{-5} \text{ cm}^2 \text{ s}^{-1}$  at the upstream position and  $D = 1.7 \times 10^{-5} \text{ cm}^2 \text{ s}^{-1}$  at the downstream position. The more intense mixing at  $x = b$  results from the shedding of a vortex at the edge of the bed section during its motion (see Hammack, 1972). The mixing of the interface at this position was visually detected by adding blue dye to the brine. At the downstream position the apparent diffusion coefficient is only slightly greater than the molecular diffusion coefficient ( $D_m = 1.5 \times 10^{-5} \text{ cm}^2 \text{ s}^{-1}$ ) for salt in water. Hence, the shear layer developed during the passage of internal waves is laminar and does not mix the fluids appreciably. Each series of experiments was stopped when the interfacial thickness at  $x = b$  reached  $\sim 2 \text{ cm}$ .

In order to quantitatively measure the internal waves, a laser-optics detector system is used. A schematic drawing of the internal wave gage is shown in Fig. 5. The light beam from a helium-neon gas laser (wavelength = 632.8 nm with 0.5 mW output) is aligned perpendicular to the glass sidewalls of the wave tank. A system of cylindrical lenses transforms the circular beam into a sheet of light with a constant vertical dimension of 4.5 cm which is directed horizontally across the wave tank. After traversing the tank, the light is focused onto a photodiode which provides an output voltage proportional to the incident light intensity. By dyeing the brine dark blue and permitting the interface to intercept the light sheet when the fluids are quiescent, subsequent motions of the interface induce changes in the output signal of the photodiode which are displayed on an oscilloscope recorder. It should be noted that the dyed interface seen by the internal wave gage appears in the upper region of the diffuse salinity interface as indicated in Fig. 4. The laser, optics and detector system are mounted on a continuous frame shaped in an inverted U over the wave tank; hence, the wave gage is calibrated by raising and lowering the frame differing amounts during quiescent fluid condition. Calibration curves are inherently nonlinear for this measurement system. Internal waves with maximum heights  $< 4.5 \text{ cm}$  are easily measured; however, large-amplitude motions are generally avoided during wave measurements at  $x = b$  due to the vortex-induced mixing at the position. The vortex generates a high-frequency signal at the photodiode which is superposed on the signal corresponding to the internal wave. In addition, the background signal for quiescent conditions may change appreciably before and after an experiment. Surface waves are electronically recorded using conventional parallel-wire resistance probes and an oscilloscope recorder.

## 6. Comparison of theoretical and experimental results

In order to examine the near-field wave structure, the temporal behavior at the edge of the generation region ( $x = b$ ) is examined. Wave motions at this location are primarily free (unforced) and provide the initial condition for propagation models which may be patched to the generation model. Results are presented for a wide range of time-size ratios in order to more clearly delineate the tsunamiogenic case (impulsive with  $h_1 \leq h_2$  and  $b/h \gg 1$ ).

### a. Wave profiles

Comparisons of theoretical wave profiles at  $x = b$  with experimental data are shown in Figs. 6 and 7. Results are shown for positive (uplift) and negative (downthrust) bed motions. Linear computations for the free surface motion agree well with measurements. (Surface wave measurements are coincident for the two cases of bed uplift.) Linear results for the internal waves also agree well with measurements; however, there are differences which require explanation. Measured waves at the interface exhibit a high-frequency noise of small-amplitude superposed on the main wave. The source of this high-frequency noise is twofold. First, as mentioned in Section 5, a vortex is shed at the downstream edge of the piston ( $x = b$ ) during rapid motions. The effect of this vortex on the amplitude measurement at the interface is most pronounced for positive motions with thin lower layers ( $h_2 < h_1$ ) and was visually observed to be responsible for the large depression in amplitude near  $t(g/h)^{1/2} \approx 12$  in measurement (d) of Fig. 6. Second, gas bubbles formed in the thin gap between the piston and its confining tank walls. These bubbles were freed during bed motion and subsequently those from the gap along  $x = b$  penetrated the light sheet of the measurement transducer. (Brine was especially prone to bubble formation resulting from aeration during mixing and chemical reactions at unavoidable scratches in the anodized aluminum of the piston.)

The time required for the lead wave to propagate past  $x = b$  differs from the linear prediction for both surface and internal waves in Fig. 6. This behavior was observed previously for surface waves by Hammack (1973) and may be partially attributed to nonlinear effects arising from both finite wave amplitudes and finite changes in depth in the generation region. Based on amplitude considerations alone, differences between linear analysis and measurements are expected to be maximum when  $h_1 \gtrsim h_2$  and minimum when  $h_1 = h_2$ . This expected behavior is exhibited in Fig. 6 even though amplitude nonlinearity is too small to account for all of the observed discrepancy. Another contributing factor is the eddy shed at  $x = b$  during piston motion. Fluid mixed by the eddy often remains in this region for some time after the waves had departed. (Eventually, this fluid spreads into its layer of neutral buoyancy.) It was confirmed qualitatively by visual observation that this phenomenon causes an apparent increase in both the wave amplitude near its leeward portion and the lead wave period similar to the behavior observed in measurement (d) of Fig. 6 (where  $h_1 > h_2$ ).

Mode separation and motions induced at the opposite interface are more clearly demonstrated by the downstream ( $x = b + 20h$ ) results shown in Fig. 8. Both experimental measurements and linear computations are presented for an impulsive bed motion with  $\zeta_0 = 1.5$  cm,  $h_1 = 5$  cm and  $h_2 = 10$  cm. The surface wave arrives first at the downstream station at  $t(g/h)^{1/2} \approx 20$  corresponding to the speed  $C_1$  given by (26a); the induced motion  $\beta_2$  at the surface is clearly evident. Observed and predicted behavior of the surface wave and its induced motion agree well. Both the interface and free surface become quiescent prior to the arrival of the internal wave. Predicted and measured shapes of the internal wave are similar; however, the maximum amplitude of the measured wave is 20% less than predicted. In addition, the time required by the observed wave to reach the downstream station corresponds to an average speed which is 10% less than the linear prediction for  $C_2$ . These discrepancies probably result from the viscous and nonlinear effects present in the experiments.

#### b. Maximum amplitudes

It is instructive to examine the variation in lead wave amplitude with the time-size ratio of the bed motion. In fact, results of this type provide the basis for classification of the generation process (impulsive, creeping and transitional). Fig. 9 shows experimental and theoretical results at  $x = b$  for both the surface and internal waves. The maximum amplitudes of the independent modes ( $N_1$  and  $N_2$ ) are shown as a function of their respective time-size ratio and layer-depth ratio. Experimental measurements for both positive and negative bed motions are presented. (Nonlinear effects for all experiments shown in Fig. 9 are expected to be small based on the discussion in Section 3.) The time-size ratio for the surface response ( $\tau_1$ ) spans the classification range of impulsive to creeping while the internal response ( $\tau_2$ ) ranges from impulsive to transitional.

Surface wave amplitudes in Fig. 9 are identical for each layer-depth ratio (since the size scale  $b/h$  is constant) and equivalent to that found for a homogeneous ocean. Both experimental and analytical results in Fig. 9 demonstrate that  $(N_1)_{\max} = \zeta_0/2$  for impulsive motions while  $(N_1)_{\max} \propto \zeta_0/\tau_1$  in the creeping regime; previous results indicate that this behavior is independent of size scale when  $b/h > 1$ . The theoretical and experimental results for the internal wave amplitudes agree well. In addition, the variation of  $(N_2)_{\max}/\zeta_0$  with  $\tau_2$  is similar to that of the surface waves except for an amplitude reduction by the factor  $h_1/h$  which appears to be valid even for time-size ratios exceeding the impulsive regime. This behavior permits the barotropic and baroclinic results to be collapsed into a single curve as shown in Fig. 10 for the full range of  $\tau_1$  and  $\tau_2$  (when the size scale satisfies  $b/h > 1$ ). The weak dependence (narrowing) of the transitional regime with larger size scales ( $b/h \gg 1$ ) is also indicated in Fig. 10.

#### 7. A comment on Coriolis effects and the two-layer approximation

It is customary and appropriate to neglect Coriolis effects for barotropic tsunamis since their energy is concentrated at periods (say,  $\tau_1 \approx 30-60$  min) small compared to possible inertial periods. (Alternatively, the length scale  $L$  of the barotropic mode is small compared to the Kelvin-Rossby radius of deformation.) However, the sluggishness of the baroclinic response indicated by  $C_2/C_1 \sim \epsilon^{1/2} \approx 0.04$  immediately suggests the possibility of mesoscale periods for these modes. Since the length scale  $L$  for both barotropic and baroclinic modes is the same and fixed by the source mechanism, a first estimate of the dominant baroclinic period is

$$t_2 \sim \frac{C_1}{C_2} t_1 \sim \epsilon^{-1/2} t_1 \sim 25 t_1.$$

When  $t_2$  is of order or greater than one inertial period [ $t_1 = 12$  h ( $\sin\Phi$ ) $^{-1}$  where  $\Phi$  is the source latitude] the baroclinic modes must be considered as inertio-gravity waves. In fact, Coriolis effects will limit the period of these inertio-gravity waves to  $t_2 < t_1$  with  $t_2 \rightarrow t_1$  as  $L \rightarrow \infty$  (e.g., see Kraus, 1972, p. 215). Neither the results of the preceding analysis nor the waveguide (one-dimensional propagation) approximation are applicable for describing the long-term (an inertial period or greater) dynamics of these waves. However, the preceding results still remain applicable for propagation times much less than an inertial period. In either case, the variability of both source lengths for tsunamigenic earthquakes and the inertial period (with latitude) suggest that the potential role of Coriolis effects is earthquake and site specific.

Finally, it should be noted that the two-layer stratification adopted herein permits an unbounded frequency spectrum for the baroclinic modes. In actuality, the continuous stratification of oceans will limit free baroclinic oscillations to frequencies less than the maximum Brunt-Vaisala frequency, say  $N_m$ . [As noted by Kraus (1972, p. 218), the two-layer model is equivalent to the first baroclinic mode of a continuous stratification with equivalent phase speeds.] For a typical ocean stratification with  $N_m \approx 0.01$  s $^{-1}$ , baroclinic wave energy will be restricted to periods  $t_2 > 10$  min. As already implied, energy generally will be concentrated at periods much greater than this lower bound.

**Acknowledgments.** Experiments for this study were performed at the W. M. Keck Laboratory of Hydraulics and Water Resources at the California Institute of Technology. Special debts of gratitude are owed to Mr. Elton Daly and his staff who assisted in the design, construction and maintenance of experimental facilities and to Professor Frederic Raichlen for his assistance throughout every phase of the investigation. Financial support for this study was provided by the National Science Foundation under Grant GI-28741X at Caltech and the Office of Naval Research, Fluid Dynamics Division, under Grant N00014-78-C-0889 at the University of California. The author would also like to thank the Center for Studies of Nonlinear Dynamics of La Jolla Institute for providing time necessary to complete the manuscript.

## REFERENCES

Cherkesov, L. V., 1968: On the problem of tsunamis in a sea with continuously varying density. *Izv. Atmos. Ocean. Phys.*, **4**, 1101–1106.

Fedosenko, V. S., and L. V. Cherkesov, 1968: Internal waves from submarine earthquakes. *Izv. Atmos. Ocean. Phys.*, **4**, 1197–1203.

Hammack, J. L., 1972: Tsunamis: a model of their generation and propagation. W. M. Keck Lab. Hydraul. Water Res., Calif. Inst. Tech., Rep. KH-R-28.

—, 1973: A note on tsunamis: Their generation and propagation in an ocean of uniform depth. *J. Fluid Mech.*, **60**, 769–699.

—, and H. Segur, 1978: Modelling criteria for long water waves. *J. Fluid Mech.*, **84**, 359–373.

Kanamori, H., and D. L. Anderson, 1975: Theoretical basis of some empirical relations in seismology. *Bull. Seismol. Soc. Amer.*, **65**, 1073–1095.

Keulegan, G., 1953: Characteristics of internal solitary waves. *J. Res. Nat. Bur. Stand.*, **51**, No. 3, 133–140.

Kraus, E. B., 1972: *Atmosphere-Ocean Interaction*. Oxford University Press, 555 pp. (see pp. 217–218).

Lamb, H., 1945: *Hydrodynamics*, 6th ed. Dover Publications, 372 pp.

Noda, E., 1970: Water waves generated by landslides. *J. Waterways, Harbors Div., ASCE*, **96**, 835–855.

Sells, C. C. L., 1965: The effect of a sudden change of shape of the bottom of a slightly compressible ocean. *Phil. Trans. Roy. Soc. London*, **A258**, 495–528.

FIG. 1. Fluid domain and sea floor dislocation model:  
(a) spatial, (b) temporal.

FIG. 2. Theoretical wave profiles at  $x = b = 61$  cm for  $\epsilon = 0.05$  and  $h = 15$  cm:  
(—) free surface waves (all  $h_1/h$ ); broken curves represent internal waves:  
(—)  $h_1/h = 2/3$ ; (—)  $h_1/h = 1/2$ ; (—)  $h_1/h = 1/3$ ; (----)  $N_2$ . (a)  $\tau_1 = 0.1$ ,  $\tau_2 = 0.01$ ; (b)  $\tau_1 = 5.2$ ,  $\tau_2 = 0.5$ .

FIG. 3. Theoretical variation of maximum wave amplitudes with source size scale  $b/h$  at  $x = b$  for impulsive response: (solid line),  $(\eta_1)_{\max}/\zeta_0$ ; dashed line,  $(\eta_2)_{\max}/\zeta_0$ .

FIG. 4. Experimental density profiles for  $h_1 = 5$  cm and  $h_2 = 10$  cm: line with open circles, initial profile; line with closed circles, final profile. (a)  $x = b$ ,  $\Delta t = 205$  min; (b)  $x = b + 120h$ ,  $\Delta t = 185$  min.  $S$  indicates elevation of observed (dyed) interface.

FIG. 5. Schematic drawing of internal wave gage.

FIG. 6. Theoretical and experimental waves at  $x = b = 61$  cm with  $h = 15$  cm and  $\epsilon = 0.05$ : solid line, theory; dashed line, experiment. (a) Free surface; (b) interface;  $h_1 = 5$  cm,  $\zeta_0 = 1.00$  cm,  $\tau_1 = 0.13$ ,  $\tau_2 = 0.014$ ; (c) interface;  $h_1 = 7.5$  cm,  $\zeta_0 = -1.00$  cm,  $\tau_1 = 0.25$ ,  $\tau_2 = 0.027$ ; (d) interface;  $h_1 = 10$  cm,  $\zeta_0 = 1.00$  cm,  $\tau_1 = 0.12$ ,  $\tau_2 = 0.012$ .

FIG. 7. Theoretical and experimental waves at  $x = b = 61$  cm with  $h = 15$  cm and  $\epsilon = 0.05$ : solid line, theory; dashed line, experiment. (a) Free surface; (b) interface  $h_1 = 5$  cm,  $\zeta_0 = -1.00$  cm,  $\tau_1 = 5.13$ ,  $\tau_2 = 0.53$ ; (c) interface,  $h_1 = 7.5$  cm,  $\zeta_0 = -0.97$  cm,  $\tau_1 = 4.53$ ,  $\tau_2 = 0.50$ ; (d) interface;  $h_1 = 10$  cm,  $\zeta_0 = 2.00$  cm,  $\tau_1 = 4.87$ ,  $\tau_2 = 0.50$ .

FIG. 8. Theoretical and experimental waves at  $x = b + 20i$ :  
 $h = 15$  cm,  $h_1 = 5$  cm,  $b = 61$  cm,  $\epsilon = 0.05$ ,  $\zeta_0 = 1.5$  cm.  
 $\tau_1 = 0.12$ ,  $\tau_2 = 0.012$ ; solid line, free surface; dashed line, interface. (a) Linear theory; (b) experiment.

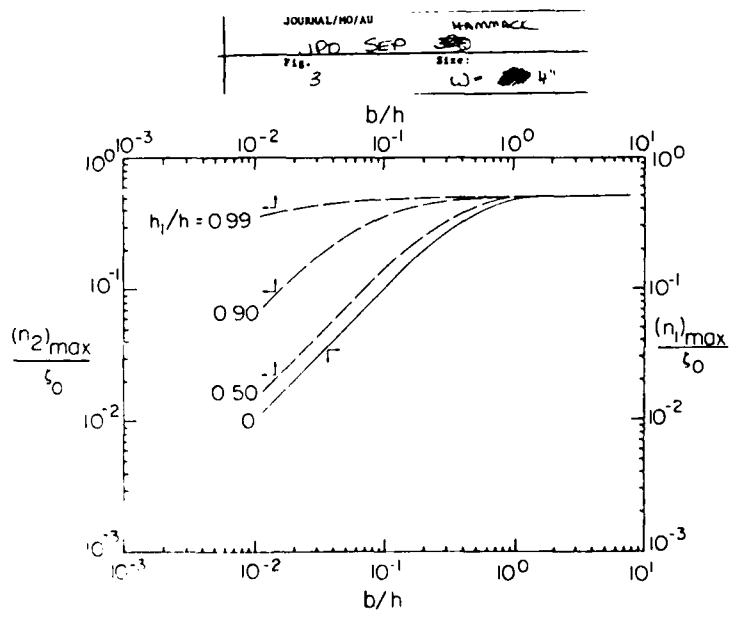
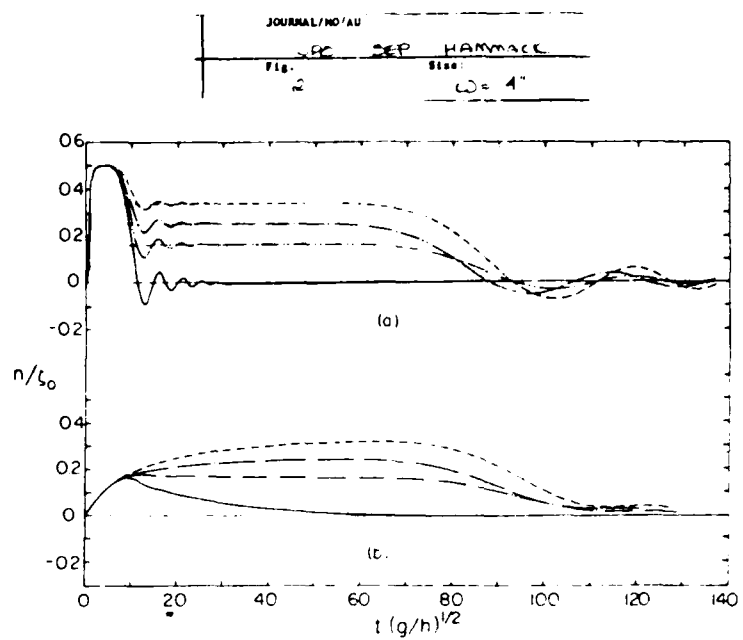
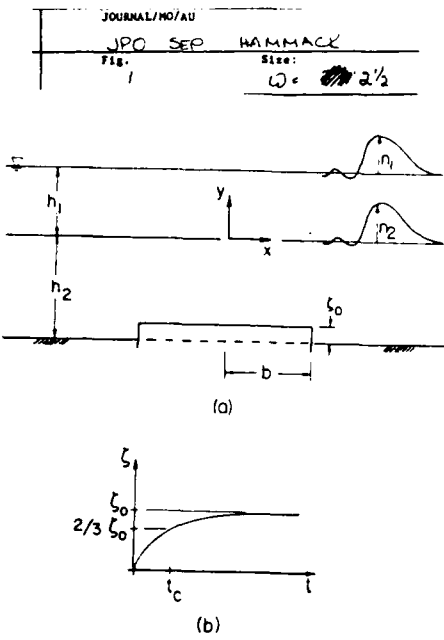
FIG. 9. Variation of  $(N_1)_{\max}/\zeta_0$  with  $\tau_1$  and  $(N_2)_{\max}/\zeta_0$  with  $\tau_2$  at  $x = b = 61$  cm for  $h = 15$  cm,  $\epsilon = 0.05$ . Solid curve represents surface wave calculation (for all  $h/h_1$ ) using linear theory. Vertical slash indicates experimental data for surface waves.

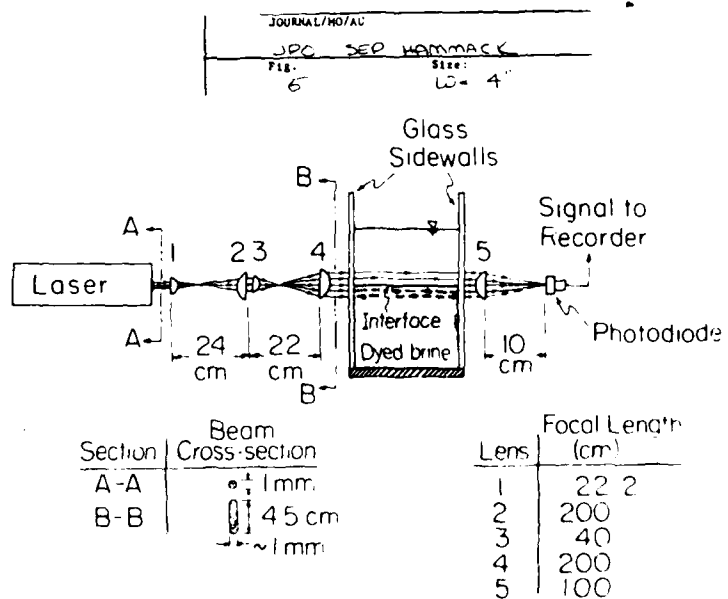
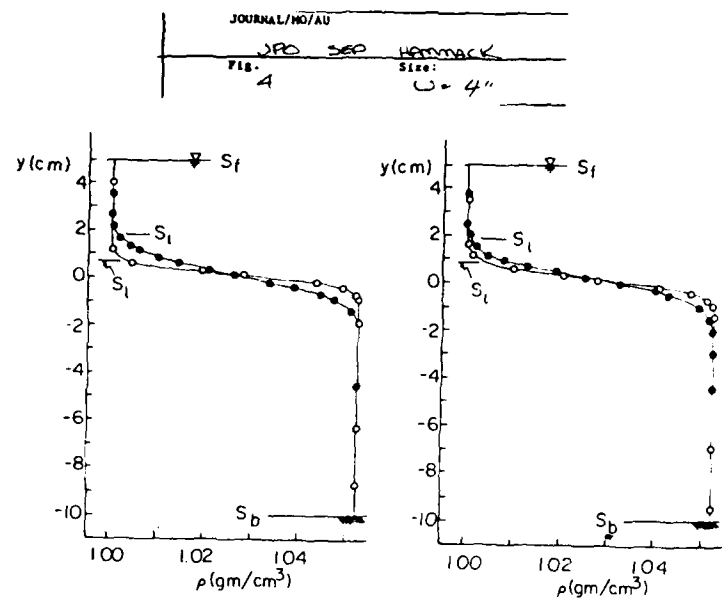
FIG. 10. Theoretical variation of  $(N_1)_{\max}/\zeta_0$  with  $\tau_1$  and  $[(N_2)_{\max}/\zeta_0](h/h_1)$  with  $\tau_2$  at  $x = b$ . Dashed curve indicates asymptotic results for  $h/h_1 \gg 1$ .

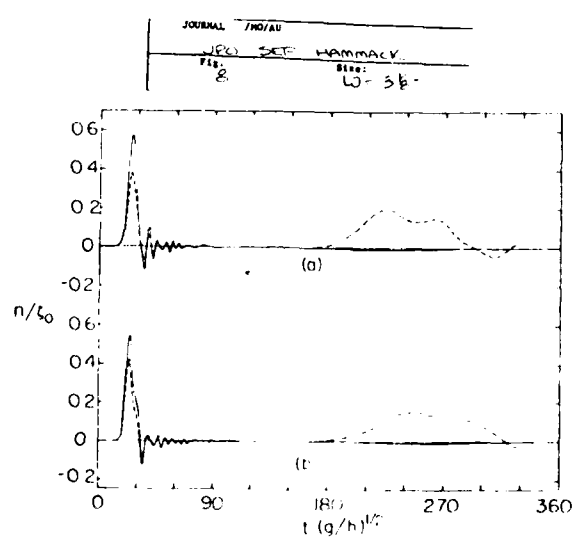
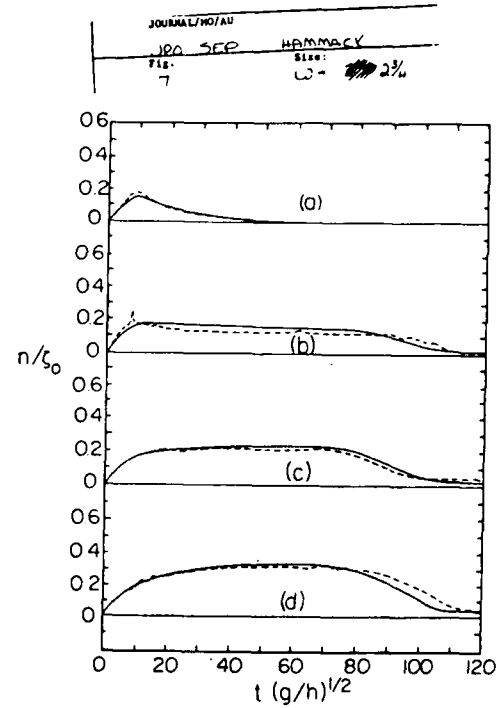
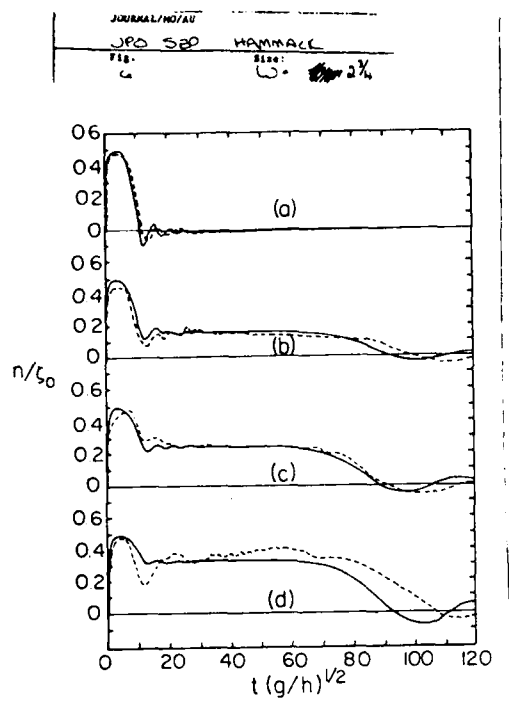
## Hammack, Table 1

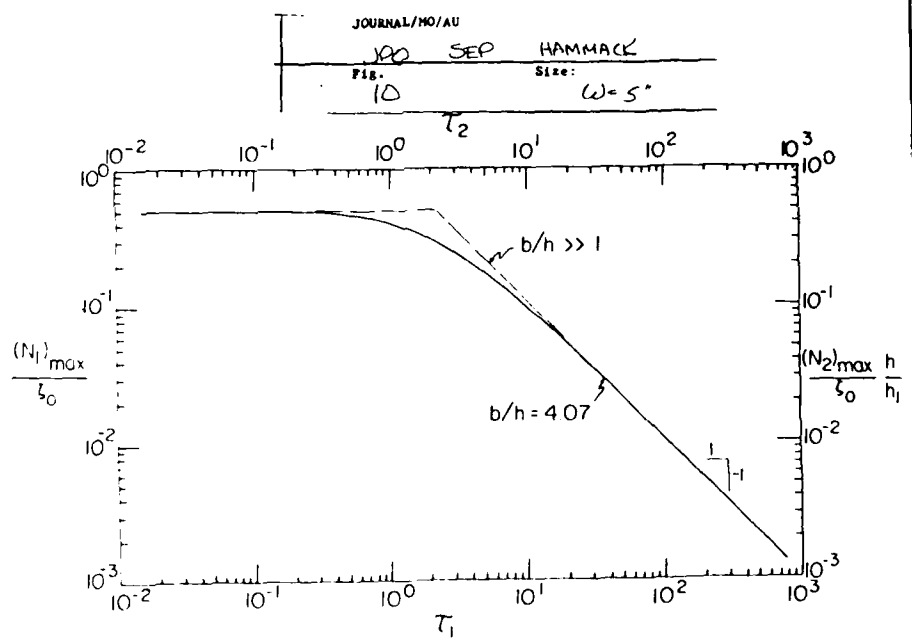
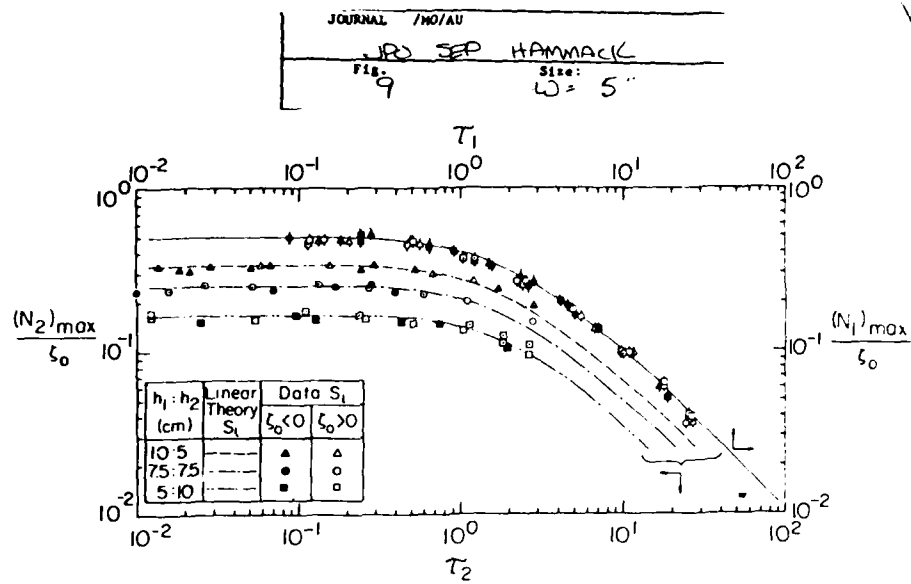
TABLE 1. Characteristic source area of tsunamigenic earthquakes as a function of seismic moment  $M_0$  based on Kanamori and Anderson (1975).

$M_0$ (dyn cm)	$S$ (km $^2$ )	$M_s$	$L$ (km)	$ \zeta_0 $ (m)
$2 \times 10^{25}$	185	6	14	0.2
$6 \times 10^{25}$	1850	7	43	0.7
$1 \times 10^{26}$	54 000	8	233	4.0









Appendix III

Long Waves Generated By Complex  
Bottom Motions

(To appear in *Proceedings, International  
Conference on Coastal Engineering,  
March, 1980, Sydney, Australia*)

## LONG WAVES GENERATED BY COMPLEX BOTTOM MOTIONS

J. L. Hammack

Associate Professor of Civil Engineering  
University of California, Berkeley, U.S.A.

and

F. Raichlen

Professor of Civil Engineering  
California Institute of Technology, Pasadena, U.S.A.

### 1. Introduction

Studies of tsunami generation often employ simple models of the sea floor dislocations to permit tractable analytical solutions. Although these solutions provide basic insight into the generation process, they are incapable of producing explicit results for prototype events where both the spatial and temporal distributions of the sea floor dislocation may be quite complicated. Herein we exploit the apparent linearity of the generation process and demonstrate both the use and validity of the superposition principle to construct solutions for complex bed motions. Analytical and experimental results are presented for a monopolar dislocation (block upthrust or downthrow) with a complex time-displacement history. The time history used in the computations is obtained from an integrated accelerogram recorded at Pacoima Dam, near Los Angeles, during the earthquake of February 9, 1971. A complex spatial deformation is not used in order to enable experimental verification of the analytical results. This is unfortunate since it appears that the details of the time-displacement history are not important for prototype phenomena where the motion may be considered instantaneous. However, it is important to note that the analysis treats both space and time variations in an identical manner; hence, confirmation of this approach for complex time variations strongly suggests analogous behavior for complex spatial variations.

Finally, we examine and compare several alternative time-displacement histories for the mean motion. It is shown that the results for each mean motion can be unified by introducing a velocity as a descriptive parameter which is based on the kinetic energy input of the moving bottom to the overlying fluid.

### 2. Time-Displacement History

To define a complicated time-displacement history with relevance to earthquake-induced ground motions, we have chosen an accelerogram for the vertical component of motion recorded at Pacoima Dam (near Los Angeles) during the earthquake of February 9, 1971. The accelerogram

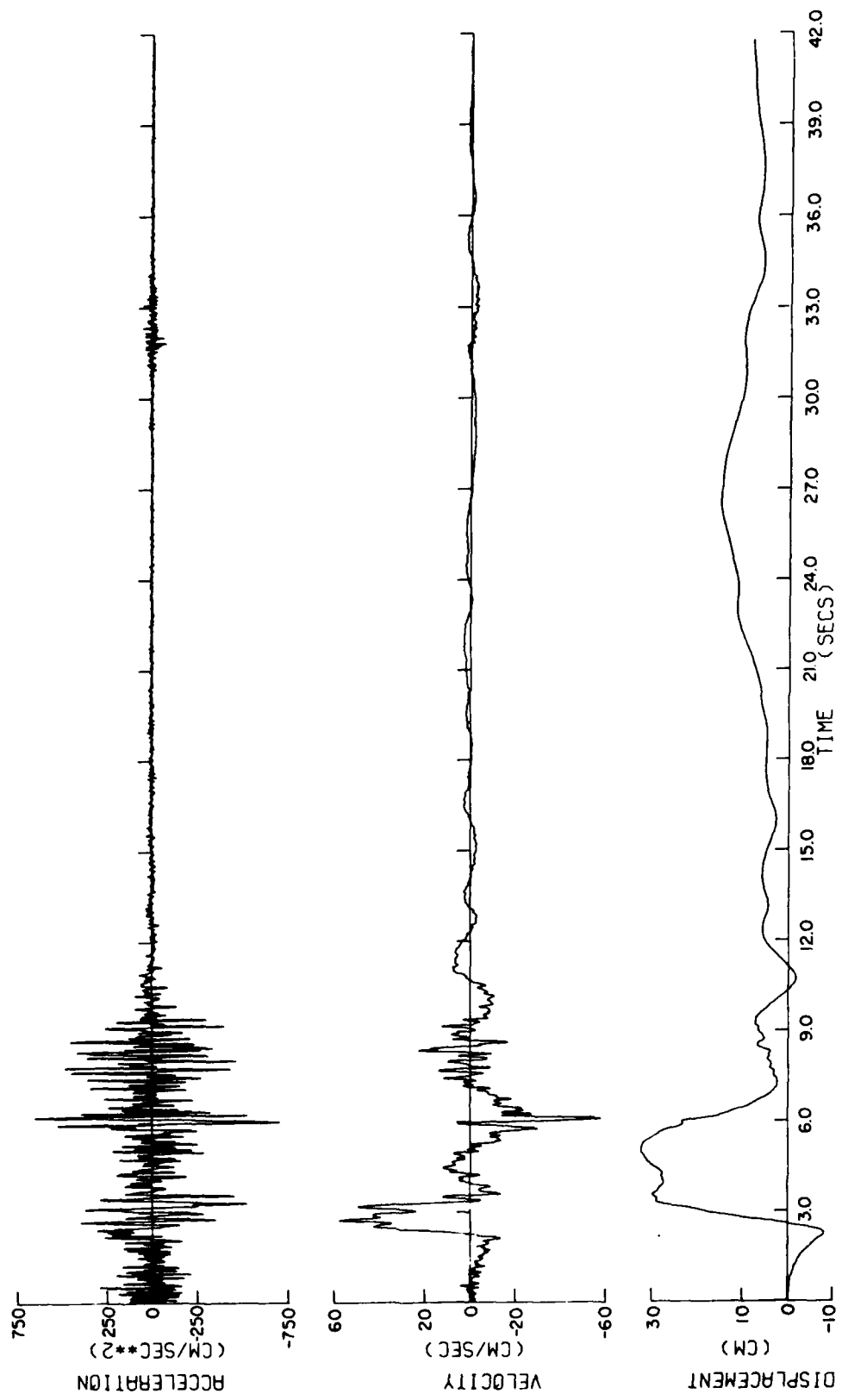


Figure 1. Vertical component of ground acceleration recorded 2/9/71 0600 PST Pacoima Dam, California, with integrated velocity and ground displacement.

shown in Figure 1 may be integrated numerically using appropriate precautions (e.g., see Nigam and Jennings, 1968), to yield a time history of the vertical ground displacement. Results of the integration process for the "smoothed" velocity history and the corresponding ground displacement history are shown below the accelerogram in Figure 1.

An analytical representation of the algebraically complex time-displacement history of Figure 1 over a finite record interval,  $0 \leq t \leq T$ , may be constructed using a Fourier series of the form:

$$\zeta(t) = C_0 + \sum_{n=1}^{N} C_n \sin(K_n t + \beta_n). \quad (1)$$

In (1)  $C_n$  are the amplitudes of the Fourier components with  $C_0$  representing the mean (permanent) ground displacement,  $K_n$  are the component wave frequencies, and  $\beta_n$  are the component phase angles. The accuracy of (1) in representing the integrated displacement of Figure 1 is determined by the number of components  $N$  retained in the Fourier sum. Results of computations with  $N = 18$  are illustrated in Figure 2; this truncated sum will be adopted in the subsequent analysis.

It should be emphasized that both the instrument characteristics and the numerical integration techniques used to obtain ground displacements from acceleration measurements necessarily distort (filter) information in long period components. In particular, the mean (and permanent) displacement of the integrated motion shown in Figure 1 (and, of course, its Fourier representation in Figure 2) is not expected to accurately model the actual permanent deformation. To compensate for this distortion, we may again exploit the superposition principle and add a nonsinusoidal component to the Fourier series representation of (1). As an example of this approach, consider the ramp motion in time of the form:

$$\zeta_r(t) = \zeta_0 t/T \quad (2)$$

during the time interval  $0 \leq t \leq T$ ; other choices for the mean motion are discussed and compared in section 5. In practice, the sum of the mean component resulting from the Fourier synthesis,  $C_0$ , and the additional component  $\zeta_0$  from (2) should be chosen to equal the actual permanent ground offset. Hence, a general representation for a complicated time-displacement history becomes:

$$\zeta(t) = C_0 + \zeta_0 t/T + \sum_{n=1}^{N} C_n \sin(K_n t + \beta_n). \quad (3)$$

### 3. Solutions of the Water Wave Problem

Consider a two-dimensional  $(x, y)$  and incompressible ocean of uniform depth  $h$  initially in equilibrium with the earth's gravitational field  $g$  which acts in the negative  $y$  direction. At time  $t = 0$  a section of the

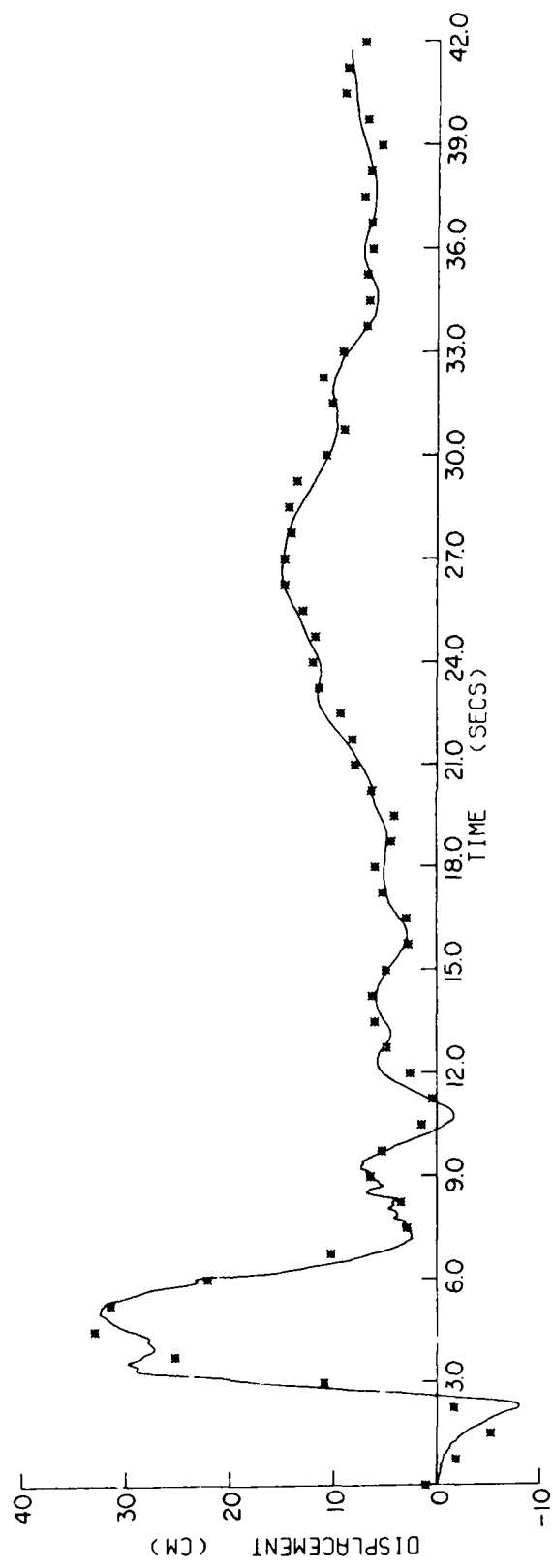


Figure 2. Vertical ground displacement (—) and Fourier synthesis (\*) using eighteen components.

sea floor begins to deform vertically with a time and spatial variation given by  $\zeta(x, t)$ . We seek the inviscid, irrotational, and barotropic deviations  $\eta(x, t)$  of the ocean free surface from its equilibrium position. With the coordinate system at the equilibrium position of the free surface, the linearized description of motion in terms of a velocity potential  $\phi = \phi(x, y, t)$  is:

$$\phi_{xx}(x, y, t) + \phi_{yy}(x, y, t) = 0 \quad (4)$$

$$\phi_y(x, -h, t) = \zeta_t(x, t) \quad (5)$$

$$\phi_y(x, 0, t) = \eta_t(x, t) \quad (6)$$

$$\phi_t(x, 0, t) = -gn(x, t) \quad (7)$$

where subscripted variables indicate partial differentiation. It is convenient to eliminate  $\eta(x, t)$  in (6) and (7) by combining to yield a single condition for the velocity potential:

$$\phi_{tt}(x, 0, t) + g\phi_y(x, 0, t) = 0 \quad (8)$$

Using the Laplace transform in  $t$  and the Fourier transform in  $x$ , equations (4), (5) and (8) become:

$$\bar{\phi}_{yy}(k, y, s) - k^2 \bar{\phi}(k, y, s) = 0 \quad (9)$$

$$\bar{\phi}_y(k, -h, s) = s \bar{\zeta}(k, s) \quad (10)$$

$$\bar{\phi}_y(k, 0, s) + \frac{s^2}{g} \bar{\phi}(k, 0, s) = 0 \quad (11)$$

where the overbar of a function  $f(x, t)$  indicates:

$$\bar{f}(k, s) = \int_{-\infty}^{\infty} dx \int_{-\infty}^{\infty} e^{ikx} e^{-st} f(x, t) dt. \quad (12)$$

Solving (9), (10), and (11) for  $\bar{\phi}(k, y, s)$  and noting from (7) that

$$\bar{\eta}(k, s) = - (s/g) \bar{\phi}(k, 0, s) \quad (13)$$

we find:

$$\bar{\eta}(k, s) = s^2 \bar{\zeta}(k, s) / (s^2 + \omega^2) \cosh kh \quad (14)$$

where  $\omega^2 = gk \tanh kh$ . Inverting the Laplace and Fourier transforms yields:

$$\eta(x, t) = \frac{1}{2\pi} \int_{-\infty}^{\infty} \left\{ \lim_{\Gamma \rightarrow \infty} \frac{1}{2\pi i} \int_{\mu-i\Gamma}^{\mu+i\Gamma} \frac{s^2 e^{-ikx} e^{st} \bar{\zeta}(k, s)}{(s^2 + \omega^2) \cosh kh} ds \right\} dk \quad (15)$$

Again, the final integration over wavenumber  $k$  must be evaluated numerically.

#### 4. Comparison of Theory and Experiment

As noted earlier, the simple block deformation of the sea floor was chosen to enable experimental verification of the analytical model developed for complicated time-displacement histories. The experimental facility used in these tests has been described in detail by Hammack (1972, 1973). Basically, the wave-maker consists of a rectangular piston in the bottom of a wave tank (and spanning its width) whose motion is controlled by an electro-hydraulic-servo system. The servo system converts a time-voltage command signal into a proportional vertical displacement of the piston. For the experiments reported herein, the piston length in the direction of wave motion is  $b = 61$  cm while the quiescent water depth above the piston is  $h = 10$  cm. Before presenting results of the tests, we describe the motivation for choosing other experimental scales.

A "global" time scale for the forcing of the overlying ocean by the sea floor is the period  $T$ . The appropriate time scale for the gravitational response of the long barotropic wave modes is  $b/(gh)^{1/2}$  which corresponds to the time required for waves to escape the generation region. For prototypical earthquakes the ratio of the forcing and response time scales,  $\tau = T(gh)^{1/2}/b$ , termed the time-size ratio, is small so that details of the time-displacement history generally are not important. However, our interests herein require that the details of the temporal motion have a significant impact on the generated wave structure. Hence, the period  $T$  for the experimental tests must be scaled so that  $\tau$  exceeds unity; in fact, for the experiments a period  $T = 4$  secs was chosen which yields  $\tau = 6.5$ . Previous experiments by Hammack (1973) also indicate that the generation process for prototypical tsunamis is linear and that nonlinearity remains insignificant for vertical displacements which do not exceed about 20% of the overlying ocean depth. This criterion is adhered to in the experiments by restricting the instantaneous displacement of the piston to less than 2 cm.

In the first test we examine experimental and theoretical results for the time-displacement history shown in Figure 2 using experimental parameters  $T = 4$  secs and a chosen permanent (mean) displacement of  $C_0 = 0.38$  cm, with the amplitudes  $C_n$  and frequencies  $K_n$  of the eighteen Fourier components used in Figure 2 scaled appropriately. (In Figure 2 the corresponding parameters of the actual ground displacement are  $T = 40$  secs and  $C_0 = 7.63$  cm.) The scaled Fourier components are then summed and the result is converted to an analogue (time-voltage) signal which is used to command the wavemaker. The resulting wave motion at the leading edge of the piston ( $x = b$ ) is measured, and the results are shown in Figure 3. Theoretical results at  $x = b$  are evaluated for each of the eighteen (scaled) Fourier components according to (17) and summed to yield

$$\eta(b,t) = C_0 + \sum_{n=1}^{18} \eta_n(b,t); \quad (25)$$

the results also are shown in Figure 3. The excellent agreement between the predicted and measured data is self-evident.

Similar results are shown in Figure 4 where a ramp mean motion with an amplitude of  $\zeta_0 = 1.33$  cm is added to the Fourier synthesis of Figure 2. The total permanent displacement of the piston is  $\zeta_0' = C_0 + \zeta_0 = 1.71$  cm which has been used to normalize the measured and theoretical wave amplitudes. The theoretical result is equivalent to (25) with an added component for the ramp computed from (24). Again, the agreement between measured and computed data is excellent with the wave structure clearly showing the added volume (mass) resulting from the enhanced mean displacement.

### 5. A Comment on Mean Motions

In previous studies (Hammack, 1972, 1973) two additional models for the mean displacement of a block section of the sea floor have been examined. These time histories are:

- a. exponential:  $\zeta_e(t) = \zeta_0[1 - \exp(-1.1t/T_e)]$
- b. half-sine:  $\zeta_s(t) = \zeta_0[(1 - \cos \pi t/T_s)H(T_s - t)/2 + H(t - T_s)]$

and we repeat for completeness the mean motion introduced here:

- c. ramp:  $\zeta_r(t) = \zeta_0[tH(T_r - t)/T_r + H(t - T_r)].$

The three mean motions listed above span a wide range of displacement characteristics. We note that the choice of characteristic time scales  $T_e$ ,  $T_s$  and  $T_r$  are, in fact, arbitrary to a certain extent even though "natural" choices are apparent. (This flexibility is most obvious for the exponential motion where  $T_e$  was chosen for experimental convenience to represent the time for two-thirds of the displacement to occur.) It has been found that the properties of waves generated by these motions correlated strongly with the time-size ratio  $\tau$  based on these time scales. For example, the maximum wave amplitude, say  $\eta_0$ , occurring at  $x = b$  when normalized by the permanent displacement  $\zeta_0$  exhibits a simple and similar functional dependence on  $\tau$  for each bed motion. With the size scale  $b/h$  of the dislocation fixed and for  $\tau \ll 1$ , the normalized amplitude,  $\eta_0/\zeta_0$ , reaches a maximum value of one-half for all size scales exceeding unity. Bed motions with  $\tau \ll 1$  are termed impulsive. For  $\tau$  very large, termed creeping generation,  $\eta_0/\zeta_0$  decreases at a rate which is inversely proportional to  $\tau$ . The constant of proportionality for creeping generation varies with the specific choice of the characteristic time scale for the mean motion. Since it is unlikely that any of these mean motion models is "correct" from a geophysical point of view, there is a need to seek a unification of results by generalizing the concept of characteristic time scale. One generalization which closely

where the complex inversion integral for the Laplace transform has been used. In (15)  $\omega$  is the wave frequency ( $\omega = is$ ) and  $k$  is the wavenumber. Explicit results for specific deformations of the sea floor  $\zeta(x, t)$  will be developed now.

### 3.1 Solution for a single Fourier component

Consider a block section of the sea floor of length  $2b$  whose time-displacement history corresponds to a single Fourier component of (1). With the coordinate system centered above the block section, we have

$$\zeta_n(x, t) = C_n H(b^2 - x^2) [\sin(K_n T + \beta_n) H(t - t) + \sin(K_n t + \beta_n) H(t - T)] \quad (16)$$

where  $H(\cdot)$  is the Heaviside step function. Finding the transform of (16), substituting into (15), performing the integration around the Bromwich contour, taking only the real part of the resulting integral, and noting that the integrand is an even function of  $k$ , we find:

$$\eta_n(x, t) = \frac{2C_n}{\pi} \int_0^\infty \frac{\cos kx \sin kb}{k \cosh kh} \left\{ A + B - H(t-T)[C + D + E] \right\} dk \quad (17)$$

where

$$A = \sin \beta_n [(\omega^2 \sin \omega t - K_n^2 \sin K_n t) / (\omega^2 - K_n^2)] \quad (18)$$

$$B = K_n \cos \beta_n [(\omega \sin \omega t - K_n \sin K_n t) / (\omega^2 - K_n^2)] \quad (19)$$

$$C = \sin(K_n T + \beta_n) \left\{ [\omega^2 \cos \omega(t-T) - K_n^2 \cos K_n(t-T)] / (\omega^2 - K_n^2) \right\} \quad (20)$$

$$D = K_n \cos(K_n T + \beta_n) \left\{ [\omega \sin \omega(t-T) - K_n \sin K_n(t-T)] / (\omega^2 - K_n^2) \right\} \quad (21)$$

$$E = -\sin(K_n T + \beta_n) \cos \omega(t-T). \quad (22)$$

The final integration over wavenumber  $k$  in (17) is obtained by numerical quadratures.

### 3.2 Solution for ramp mean motion

The ramp time-displacement history of (2) for the block deformation is described by

$$\zeta(x, t) = \zeta_0 H(b^2 - x^2) [tH(T - t)/T + H(t - T)]. \quad (23)$$

Following the same procedure outline in section 3.1, we obtain (again after considerable algebra) the water surface motion  $\eta_r$  due to the ramp

$$\eta_r(x, t) = \frac{2\zeta_0}{\pi} \int_0^\infty \frac{\cos kx \sin kb}{k \cosh kh} \left( \frac{1}{\omega T} \right) [\sin \omega t - H(t - T) \sin \omega(t-T)] dk. \quad (24)$$

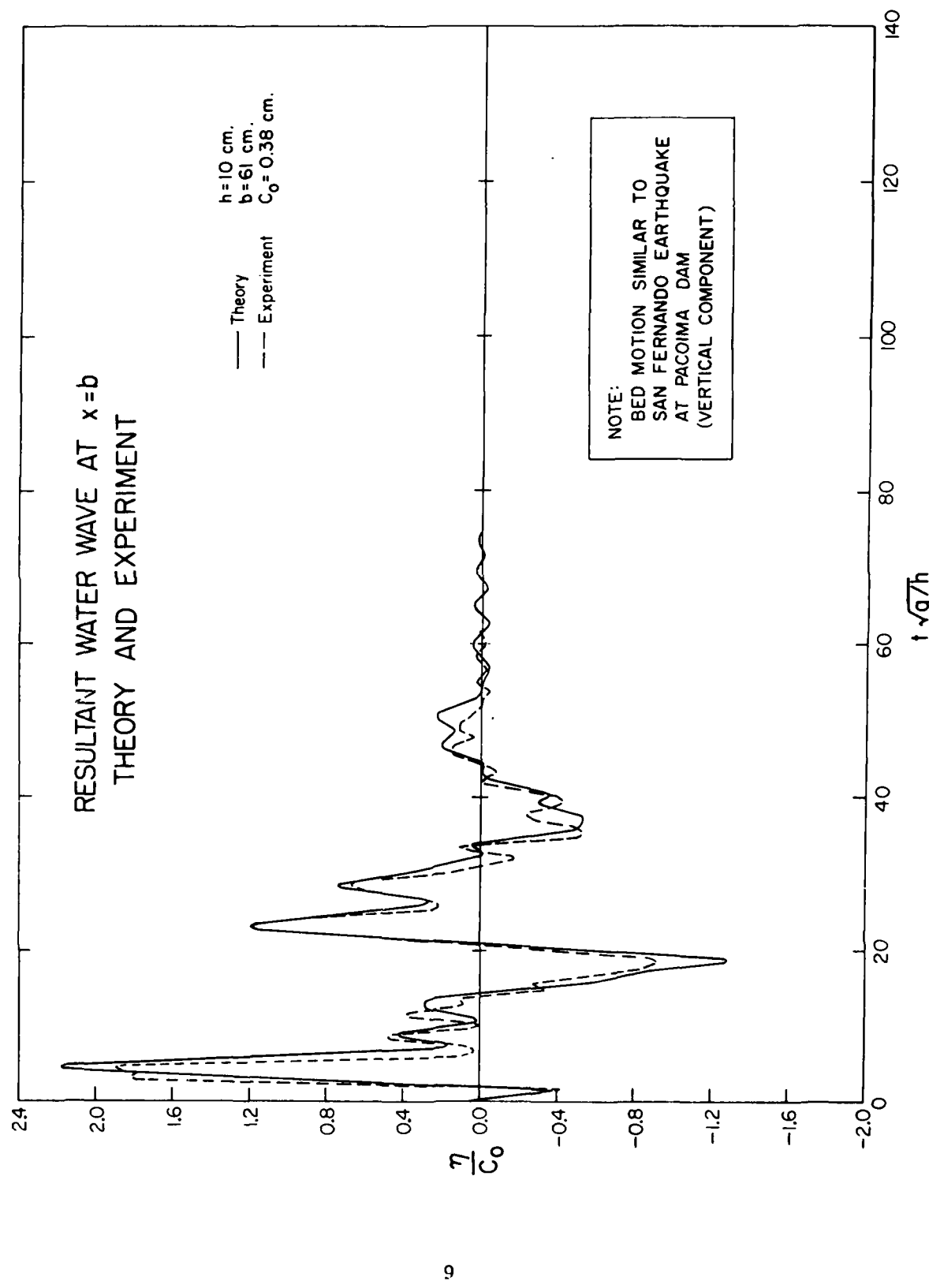


Figure 3. Theoretical (—) and experimental (---) wave records at  $x = b$ .

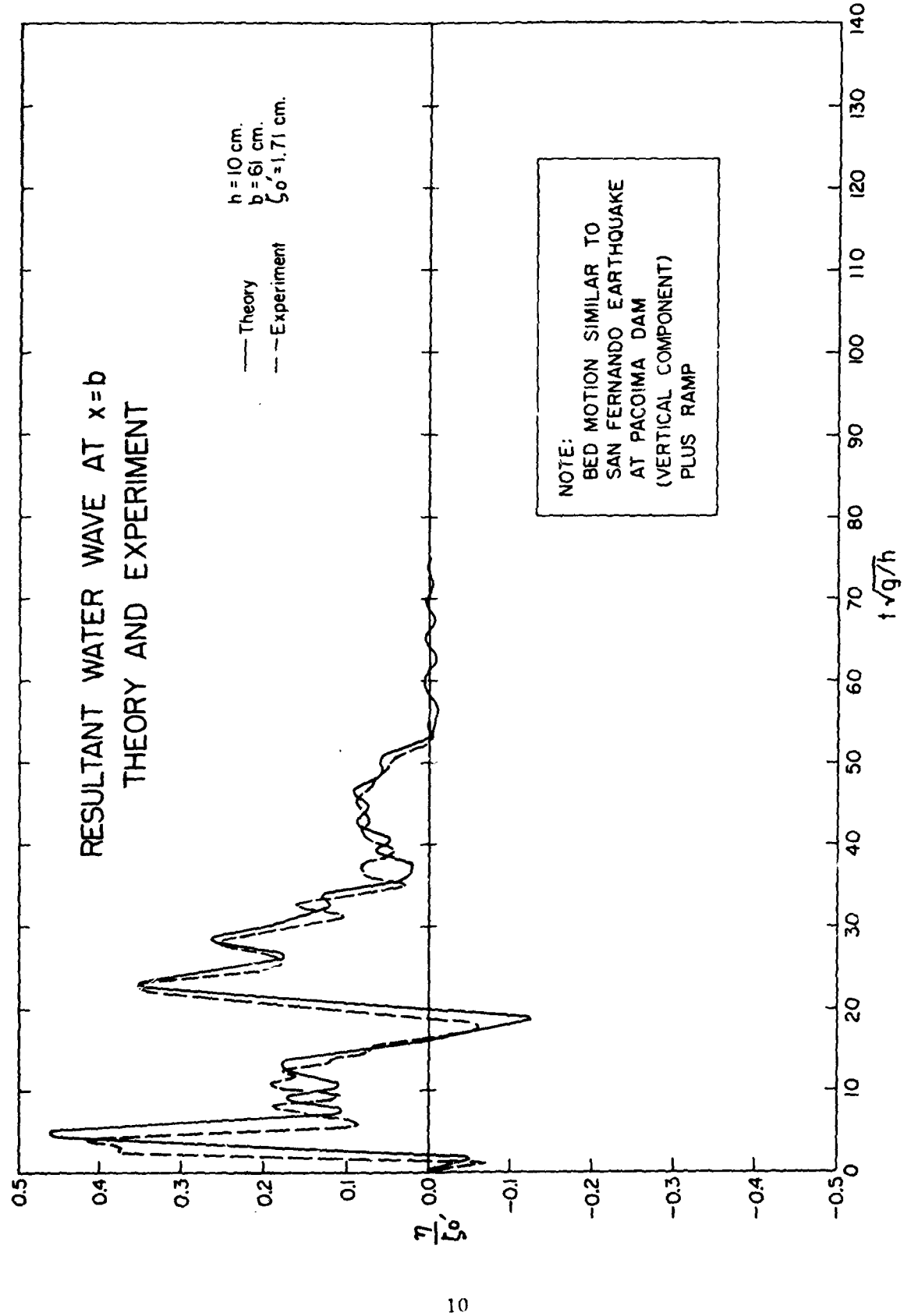


Figure 4. Theoretical (—) and experimental (---) wave records at  $x = b$  with ramp mean motion.

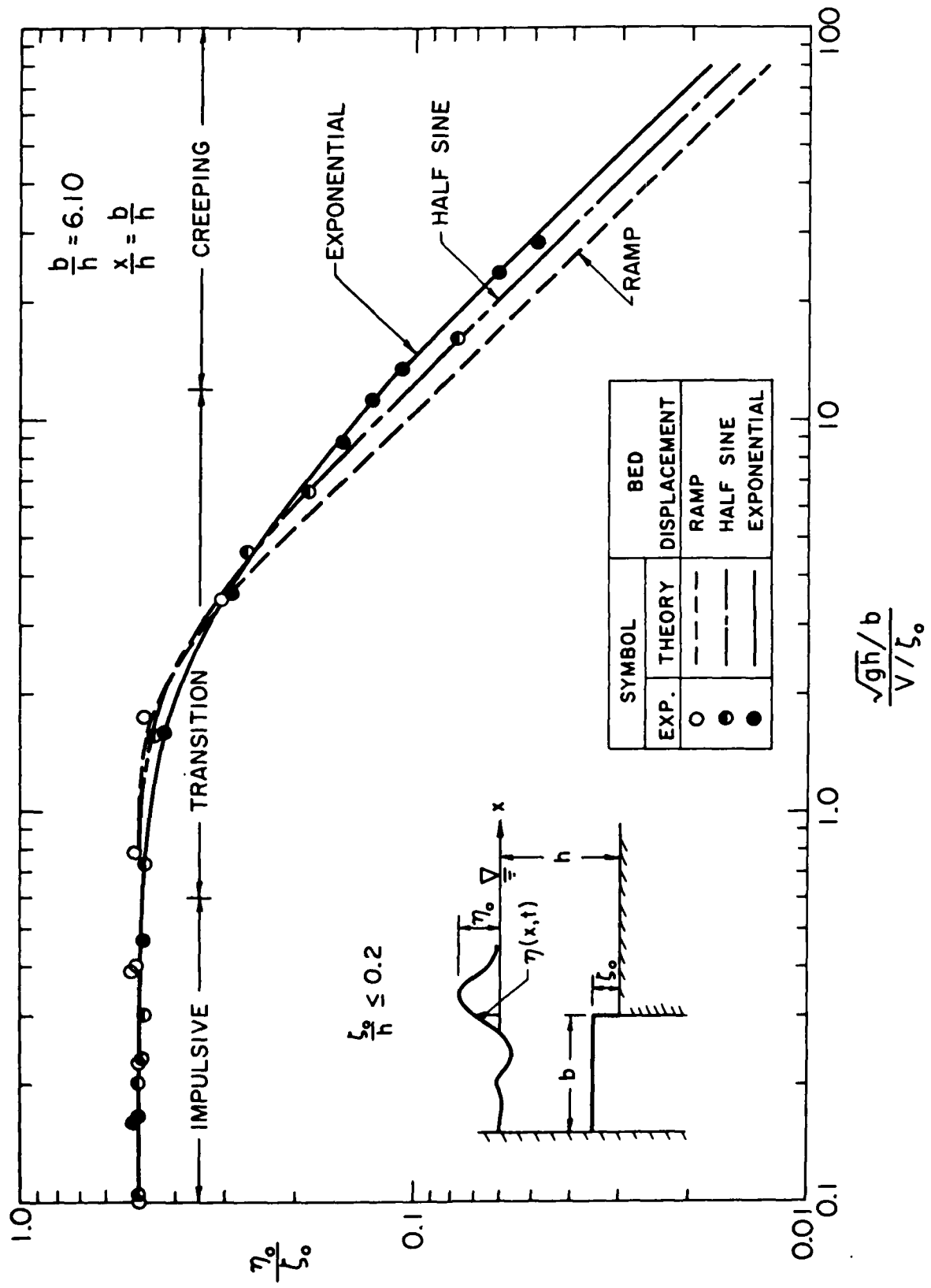


Figure 5. Theoretical and experimental variation of normalized wave amplitude at  $x = b$  with generalized time-size ratio for three mean motions.

produces the desired unification is the following. Consider a velocity  $V$ , where  $V^2$  is the kinetic energy imparted to the fluid by the sea floor divided by one-half the total mass of fluid displaced during bed motion ( $\frac{1}{2}gb\zeta_0$ ); then  $V$  is given by:

$$V = \frac{1}{\zeta} \int_0^{\zeta_0} \zeta_t^2 d\zeta \quad (26)$$

and a corresponding time scale  $T = \zeta_0/V$ . In terms of this time scale the time-size ratio becomes

$$\tau^* = T(gh)^{\frac{1}{2}}/b = \zeta_0(gh)^{\frac{1}{2}}/bV \quad (27)$$

The variation of  $\eta_0/\zeta_0$  at  $x = b$  for  $b/h = 6.1$  with  $\tau^*$  is shown in Figure 5 for each of the mean motions; both theoretical and experimental results are presented. For all of the experimental data we have taken  $\zeta_0/h < 0.2$  to avoid significant nonlinear effects. The collapse of results for such a wide range of mean motion characteristics shown in Figure 5 is good although a small spread still exists.

## 6. Conclusions

We have demonstrated both the application and validity of a strategy which employs multiple uses of the superposition principle to develop theoretical solutions for waves generated by sea floor motions with complicated time-displacement histories. Although a more useful test for prototypical phenomena would utilize complicated spatial distributions for the sea floor dislocation, the tests herein were restricted to simple block dislocations due to experimental limitations. However, it is emphasized that the solution method does not distinguish between space and time, and the validity established herein strongly suggests that the methods could be extended to complicated spatial deformations. Finally, we have demonstrated that wave properties (in particular the maximum amplitude of waves escaping the generation region) for a wide range of mean motion characteristics may be (almost) collapsed into a single functional relationship in terms of a time-size ratio based on an average vertical velocity of the sea floor obtained from energy considerations.

## 7. Acknowledgments

The authors gratefully acknowledge the support of the National Science Foundation under Grant AEN 72-03587-A02 at the California Institute of Technology and the Office of Naval Research under contract N00014-78-C-0889 at the University of California. One author (JLH) would also like to thank the La Jolla Institute, Center for Studies of Nonlinear Dynamics, where portions of this study were completed.

#### 8. References

Hammack, J. L., "Tsunamis: A Model of Their Generation and Propagation," *Report KH-R-28*, W. M. Keck Laboratory of Hydraulics and Water Resources, California Institute of Technology, Pasadena, 1972.

Hammack, J. L., "A Note on Tsunamis: Their Generation and Propagation in an Ocean of Uniform Depth," *Journal of Fluid Mechanics*, Vol. 60, No. 4, 1973, pp. 769-800.

Nigam, N. C., and Jennings, P. C., "Digital Calculation of Response Spectra from Strong-motion Earthquake Records, Earthquake Engineering Research Laboratory Report, California Institute of Technology, Pasadena, 1968.

Appendix IV

Lecture notes on "Small-Scale Ocean Waves"  
International School of Physics  
"Enrico Fermi"  
Course LXXX, Summer 1980  
Topics in Ocean Physics

International School of Physics  
"Enrico Fermi"  
Course LXXX, Summer 1980  
Topics in Ocean Physics

SMALL-SCALE OCEAN WAVES

J. L. Hammack

Department of Civil Engineering, University of California - Berkeley, California

I. — Introduction.

Presented below are three lectures on various aspects and types of ocean waves. In all cases we are concerned with small-scale waves for which gravitation provides the dominant restoring force. The relevant length and time scales of these waves are small compared to the Kelvin-Rossby radius of deformation and inertial period, respectively, and Coriolis effects may be neglected. In addition, the small length scales (relative to Earth's radius) permit us to ignore the curvature of the ocean surface and adopt a plane-earth approximation. Various other approximations will be adopted as appropriate in order to obtain model equations which are tractable analytically. (Fortunately, these tractable models appear to remain relevant for geophysical phenomena!) In particular, we are interested in weakly nonlinear systems in which the nonlinear effects manifest slowly; both nonlinear self-interacting and resonant-triad systems are considered.

An outline of these lectures is as follows. In Part II we examine two nonlinear model equations for the evolution of gravity waves: the Korteweg-deVries (KdV) equation for long barotropic and baroclinic waves and the nonlinear Schrödinger (NLS) equation for short barotropic waves. After a brief review of the asymptotic (large time) solution of these equations by inverse scattering theory, experimental data are presented which demonstrate the reality of soliton predictions--at least on laboratory scales. In Part III

we exploit the exact solution of the KdV equation and its linear approximations in order to derive rather precise criteria for modelling the evolution of long-wave initial data on geophysical or laboratory scales. The modelling criteria of Part II are then applied to a typical oceanic tsunami in order to choose relevant model equations for propagating the (barotropic) wave from its generation region to specific target sites. Finally, in Part IV we examine the nonlinear excitation of "edge" waves nearshore by linear wave trains incident from deep water. Both theoretical and experimental results are presented which document the excitation of two progressive edge-wave modes through a nonlinear resonant-triad interaction with the wave reflected after normal incidence from offshore.

Much of the material in Parts II and III has appeared previously in the literature. Hence, many of the details concerning experimental equipment, procedures, and analysis is omitted; a thorough discussion may be found in the cited references. The material presented in Part IV on edge waves is recent and not presently available in the literature. For clarity, a more detailed discussion of this material is presented. We also note here that the notation between Parts II, III, and IV is not necessarily consistent.

## II. — Water Wave Solitons.

### 1. — Long Gravity Waves

Consider two fluid layers with uniform densities  $\rho_1 \leq \rho_2$  resting in a gravitationally stable configuration (see Figure 1) on a horizontal and impermeable bed of infinite lateral extent. The upper layer possesses a free surface  $S_f$  along which pressure is constant; surface energy effects on

$S_f$  and the fluid-fluid interface  $S_i$  are negligible. Required are the two-dimensional, inviscid, irrotational motions which are bounded everywhere and evolve from given initial distribution of velocities, free surface deformation, and interfacial deformation--the classical water wave problem. In particular, we are interested in the barotropic displacement  $n_1$  of  $S_f$  from its static equilibrium position and the baroclinic displacement  $n_2$  of  $S_i$  from its equilibrium position. To derive the KdV equation as the appropriate model for both displacements from the governing equations, the following assumptions are necessary. First, characteristic wave lengths  $k^{-1}$  (an inverse wave number) must be long relative to the total fluid depth; i.e.,  $(kh)^2 \ll 1$ , so that dispersive effects are weak. Second, characteristic wave amplitudes  $a$  are small relative to the total depth; i.e.,  $a/h \ll 1$ , so that nonlinearity is weak. Third, both weak effects of dispersion and nonlinearity are approximately equal; i.e.,  $\epsilon \equiv a/h \sim (kh)^2$ . For simplicity, we will further assume at the outset that density differences in our two-layer ocean are small (as in its geophysical counterpart) so that  $\Delta \equiv (\rho_2 - \rho_1)/\rho_2 \ll 1$ . Expanding the dependent parameters in the governing equations in a power series in  $\epsilon$  and introducing the multiple time scales  $t_0 = t$ ,  $t_1 = \epsilon t$ , . . . , one finds at leading order that the evolution equations for the initial wave are hyperbolic (nondispersive) and linear. At this order, which corresponds to the fast time scale  $t_0$ , an initial disturbance decomposes into four modes consisting of left- and right-running, barotropic and baroclinic modes. The phase speeds  $c_1$  and  $c_2$  of these modes are

(1a) Barotropic (surface) waves:  $c_1^2 = gh$

(1b) Baroclinic (interfacial) waves:  $c_2^2 = g'h_1 h_2/h$

where we have invoked the Boussinesq limit  $\Delta \rightarrow 0$  with  $g\Delta \equiv g' \ll g$  remaining finite. All wave modes propagate with permanent form and do not interact with each other or themselves; the baroclinic modes propagate much slower,  $0(\varepsilon^{1/2})$ , than the barotropic modes.

At the next order ( $\varepsilon^2$ ) weak nonlinear effects and dispersion occur. Each wave mode experiences a self-interaction on the slow time scale  $t_1 = \varepsilon t$ , but no interactions between modes occur due to their rapid separation by the phase speed differences of (1). The self-interaction of the right-running barotropic mode is governed by a dimensional equation of the form

(2)  $n_1_t + c_1 n_1_x + \frac{3}{2} c_1 n_1 n_1_x + \frac{1}{6} c_1 h^2 n_1_{xxx} = 0$

A more convenient choice of nondimensional variables for describing these waves are

(3) 
$$\left\{ \begin{array}{l} x = (x - c_1 t)/h, \quad \tau = \frac{1}{6}(g/h)^{1/2} t \\ f(x, \tau) = \frac{3}{2} n(x, t)/h \end{array} \right.$$

In terms of these variables, (2) reduces to the KdV equation with the common form

(4)  $f_\tau + 6ff_x + f_{xxx} = 0$

In a similar manner, the dimensional equation governing the self-interaction of the right-running baroclinic waves is

$$(5) \quad \eta_2_t + c_2 \eta_2_x + \frac{3}{2} c_2 \left( \frac{1}{h_2} - \frac{1}{h_1} \right) \eta_2 \eta_2_x + \frac{1}{6} c_2 h_1 h_2 \eta_2_{xxx} = 0$$

Introducing the normalized variables

$$(6) \quad \left\{ \begin{array}{l} x = (x - c_2 t) / (h_1 h_2)^{1/2} \\ \tau = \frac{1}{6} (g'/h)^{1/2} t \\ f = \frac{3}{2} \left( \frac{1}{h_2} - \frac{1}{h_1} \right) \eta \end{array} \right.$$

equation (5) reduces to the KdV equation given by (4).

The asymptotic solution of the KdV equation for arbitrary initial data  $f(x,0) \equiv f_0$  by inverse scattering theory has been described in detail by Segur<sup>1</sup> inter alios. Here, we briefly list features of the asymptotic solution to be illustrated in the laboratory experiments.

- i) An initial disturbance evolves into a finite number of permanent waves (solitons) ordered by their amplitude. When the solitons are well separated, the local shape of each is given by

$$(7) \quad f = \alpha \operatorname{sech}^2 \{ (\alpha/2)^{1/2} (x - x_0 - 2\alpha\tau) \}$$

where  $\alpha$  and  $x_0$  are constants. The rank ordered solitons are followed by a dispersive train (radiation) of oscillatory waves.

- ii) The number  $N$  of solitons evolving from initial data of finite extent, say  $f_0 = 0$  for  $x < x_1$  and  $x > x_2$ , is equivalent to the number of zeros of  $\phi$  for  $x > x_1$  where  $\phi$  satisfies

$$(8) \quad \left\{ \begin{array}{l} \frac{d^2 \phi}{dx^2} + f_0(x) \phi = 0 \\ \phi(x_1) = 1, \frac{d\phi}{dx}(x_1) = 0. \end{array} \right.$$

iii) When the net volume  $V$  (or mass) in the initial wave is finite and positive, i.e.,

$$(9) \quad V = \int_{-\infty}^{\infty} f_0(x) dx > 0$$

at least one soliton emerges.

iv) When  $f_0 \leq 0$  everywhere, no solitons emerge and the asymptotic solution consists (only) of the radiation components.

v) Two other important classes of data are those for which  $V < 0$  with  $f_0 \neq 0$  for all  $x$  and those for which  $V = 0$ . No general statements regarding the asymptotic solution for these cases is provided theoretically. Experiments demonstrate that the evolution of solitons depends on the detailed structure of the initial data.

1.1 Experimental Procedures In order to illustrate the applicability of the KdV equation as a model for long water waves, a series of experiments is conducted in a laboratory wave tank 31.6 m long, 61 cm deep, and 39.4 cm wide. For studying the barotropic motions in a system with small density differences, the density stratification plays no role; hence, in these experiments a uniform density fluid of depth  $h$  is used. A detailed description of these experiments is given by Hammack and Segur.<sup>2</sup> In order to study the evolution of baroclinic waves, the tank is stratified with fresh water and brine. Details of these experiments can be found in Hammack<sup>3</sup> as well as Hammack and Segur.<sup>4</sup>

In the long wave experiments reported here, the wavemaker consists of a rectangular piston located in the tank bottom adjacent to an upstream end-wall. The piston spans the tank width and has a length  $b$  in the direction

of wave motion (see Figure 2); lengths of  $b = 30.5$  cm and 61 cm are used. The vertical motion of the piston is controlled by an electro-hydraulic-servo system and completely user specified. In a typical experiment, the piston is moved for a finite time interval. Differences between the initial and final position of the piston permit the net volume  $V$  in the generated wave train to be calculated. Various initial data are generated by varying the time-displacement history of the piston.

Both surface and internal wave amplitudes are measured at fixed locations (stations) along the tank. We note here that differences between the temporal variation in wave amplitude at a fixed spatial position and the spatial variation in wave amplitude at a corresponding fixed time are small,  $O(\epsilon)$ , and neglected in all calculations.

### 1.2 Results for Barotropic Wave Evolution

#### 1.2.1 Initial data with $V > 0$ .

Figures 3 and 4 illustrate the evolution of two barotropic waves with a net positive volume. Normalized wave amplitudes are presented at four succeeding stations along the tank in a coordinate system which moves with the linear (nondispersive) speed  $C_1$ . Note that the leading portion of the wave system appears at the left in these figures. Shifts of the waves to the left (right) at succeeding stations indicate phase speeds greater (less) than  $C_1$  in this coordinate system.

The initial wave at  $(x - b)/h = 0$  in Figure 3 is rectangular and positive and appears to sort itself into three positive waves identified by separate crests (local maxima) during propagation. These three waves are rank ordered by amplitude and are followed by a weak train of dispersive waves whose speed

is much less than  $C_1$ . In order to examine the local shape of the leading two waves, theoretical soliton profiles defined by (7) have been superposed on the measured data at the last measurement station (using the measured wave amplitudes for specifying the parameter  $\alpha$ ). These profiles are not extended into regions where the two waves are still interacting strongly with adjacent wave structure. Clearly, the measured waves appear to be locally KdV solitons. Further evidence that the three lead waves at the last measurement station are solitons is provided by numerically integrating (8) using the wave profile at  $(x - b)/h = 0$  as the initial data  $f_0$ . Computations indicate that  $N = 3$  solitons should evolve in agreement with the observed pattern of evolution.

The evolution of a more complicated initial wave with  $V > 0$  is shown in Figure 4 where a leading negative wave is followed by a (larger) positive wave. After only twenty depths of propagation, the positive wave has separated into three separate crests while the negative wave remains essentially unchanged. During subsequent propagation the three labelled crests of the positive wave appear to retain their integrity as they progress through the leading negative wave and emerge at the front of the wave train. At the last measurement station, labelled waves 1 and 2 clearly resemble KdV solitons. The third wave is still interacting with the once-leading negative wave at the last station and cannot be unmistakably identified as a soliton. However, computations with (8) using the wave at  $(x - b)/h = 0$  as  $f_0$  yield  $N = 3$  strongly suggesting the third wave is indeed a soliton. We note that other experiments also indicate that solitons evolve from the positive waves in the initial wave and can be identified long before asymptotic conditions are achieved.

### 1.2.2 Initial waves with $V < 0$

Results for the evolution of two barotropic wave systems with  $V < 0$  are shown in Figures 5 and 6. The initial wave in Figure 5 is the negative counterpart of the experiment shown in Figure 3 where three solitons appeared to evolve. Over similar distances of propagation, no solitons appear to evolve in Figure 5 -- just as expected for initial data with  $f_0 \leq 0$  for all  $x$ . Instead, a negative wave evolves whose frontal slope decreases and lengthens with time. This lead wave is followed by a train of strongly dispersive waves with phase speeds much less than  $C_1$ . In fact, the wave structure of Figure 5 represents the radiation solution of the KdV equation as shown with quantitative tests by Hammack and Segur.<sup>5</sup>

Further evidence for the evolution of complicated waves with  $V < 0$  is shown in Figure 6. In this case the lead positive wave evolves into one or possibly two waves while the negative wave evolves in a manner similar to that observed in Figure 5. Computations using the initial wave in (8) indicate that one soliton should develop asymptotically. Hence, the second labeled wave is expected to eventually disappear as it appears to be doing.

### 1.2.3 Initial waves with $V = 0$

Figure 7 illustrates the evolution of initial data with  $V = 0$  consisting of a positive wave preceded and followed by negative waves. Applications of (8) to the initial wave suggest that two solitons should evolve. The large positive wave in the initial data quickly separates into two crests which appear to migrate through the lead negative wave during subsequent propagation. At the last station, labeled wave 1 has progressed to the front and clearly has the shape of a soliton everywhere. The second labeled wave still appears

to be interacting with the frontal slope of the once leading negative wave.

A trailing train of dispersive waves similar to that of Figure 5 also evolves.

1.3 Results for Baroclinic Wave Evolution The evolution of baroclinic long waves at the interface of a stratified fluid with  $h_1 = 45$  cm,  $h_2 = 5$  cm, and  $\Delta = 0.05$  is shown in Figure 8. Wave amplitudes recorded at seven stations along the tank in a coordinate system that moves with the linear speed  $C_2$  are presented. The initial wave is positive, and according to calculations by (8), should evolve two solitons. The observed evolution is in agreement with this prediction. (A strongly damped train of oscillatory waves has been omitted in Figure 8.) A more quantitative comparison of the lead wave profile with the theoretical shape (7) at the last four stations of measurements is shown in Figure 9. The agreement with the measured data in Figure 9 is excellent. Further results for baroclinic wave evolution are presented in Hammack and Segur.<sup>4</sup>

## 2. — Short Gravity Waves

We now turn our attention to the evolution of short gravity waves; i.e., waves whose characteristic length  $k^{-1}$  is comparable to or greater than the local ocean depth; only barotropic modes are considered. In fact, our interest in solitons requires  $kh > 1.36$  which we adopt as the definition of the short-wave regime herein. In order to derive the nonlinear Schrödinger (NLS) equation as an evolution model, we consider a wave train with a dominant and identifiable (mean) wave number  $k_0$ . As for long waves, we require weak nonlinearity, which is now characterized by the wave steepness  $\epsilon \equiv ak_0 \ll 1$ . The wave system is permitted to have weak modulations such that the variation in wave number  $\delta k$  is small; i.e.,  $\delta k/k_0 \ll 1$ . In other words, we are concerned

with "narrow-band" wave systems that are weakly nonlinear. Thirdly, we postulate a balance of both small effects so that  $\epsilon = ak_0 \sim \delta k/k_0$ . Multiple scale analysis of the governing equations again yields a hierarchy of problems at different orders of  $\epsilon$ . At lowest order we recover the linear dispersive waves of Stokes<sup>6</sup> with an amplitude a that is constant. At the next time scale,  $t_1 = \epsilon t$ , the wave amplitude is modulated, and we find that the amplitude modulations propagate with the linear group speed  $c_g$ . Continuing to the third order with a time scale  $t_2 = \epsilon^2 t$ , one finds that the complex amplitude modulation a must satisfy the NLS equation. Defining non-dimensional coordinates as

$$(10) \quad \left\{ \begin{array}{l} x = \epsilon k_0 (x - c_g t) \\ \tau = \epsilon^2 (gk_0)^{1/2} t \\ A = k_0^{-2} (gk_0)^{-1/2} a \end{array} \right.$$

the NLS equation takes the form

$$(11) \quad iA_\tau + \lambda A_{XX} + \nu |A|^2 A = 0$$

where  $\lambda$  and  $\nu$  are known functions of the water depth  $h$ , gravitation  $g$ , and carrier wave number  $k_0$  (or frequency  $\omega_0$ ). Details of the derivation for finite depth can be found in Hasimoto and Ono<sup>7</sup> inter alios.

Like the KdV equation, the NLS equation can be solved exactly for arbitrary initial data by inverse scattering theory. When  $k_0 h > 1.36$ , envelope solitons can occur; the one-soliton solution of (11) is

$$(12) \quad A = \alpha \left| \frac{2\lambda}{v} \right|^{1/2} \operatorname{sech} \{ \alpha \chi \} \exp \{ i \lambda \alpha^2 \tau \}$$

where  $\alpha$  is an arbitrary constant related to the envelope amplitude. In general, initial data of finite extent will evolve a finite number of envelope solitons, rank ordered by the group velocities of their dominant carrier waves and embedded in a dispersive train (radiation) of oscillatory waves which decays in amplitude with time. It is important to note that the speeds of both the solitons and the radiation components are not impacted by nonlinearity at this order. Hence, unlike their long wave counterparts of the KdV equation, these solitons and radiation components do not separate with time. This suggests that in order to observe clearly the evolution of envelope solitons even in a contrived laboratory experiment, one must design the initial data such that the wave content of the radiation spectrum at the dominant frequency of the soliton carrier waves is small. Alternatively, one must observe evolution until the inviscid decay of the radiation (by frequency dispersion) combined with viscous decay has progressed sufficiently.

Although a quantitative comparison of theory and experiment for the NLS equation analogous to that of the KdV equation has not been performed, qualitative tests by Yuen et al<sup>8</sup> provide evidence for its applicability to narrow band systems. We present in Figure 10 an (unpublished) experiment which illustrates the evolution of an initial wave packet whose envelope amplitude and carrier wave frequency are modulated; the mean wave frequency is  $\omega_0^{-1} = 0.6$  sec. The experiment is conducted in a tank approximately 50 m long, 2.5 m wide, and a water depth of  $h = 1$  m. After 45 m of propagation, the initial packet evolves into a collection of wave groups which are

ordered by the group speed of their dominant carrier wave. Energy is concentrated in the group with carrier waves at the dominant period  $\omega^{-1} \approx 0.6$  sec of the initial data. The envelope of this group clearly has the shape of the soliton profile (12) shown superposed on the measured wave. The envelopes for the other wave groups do not agree with (12), and apparently these groups represent the radiation components in the initial data.

Although testing of the NLS equation is not complete, there is growing evidence (see Yuen and Lake<sup>9</sup>) that the dynamics of short-water waves is much more complicated than that of long waves, and more complicated models are required. The restriction of the NLS equation to narrow band systems and its (probable) instability to transverse perturbations appear especially severe for many geophysical applications.

### III. — Modelling Criteria for Long Water Waves.

Even with all the assumptions implicit in the classical water-wave problem introduced in Part II, the general equations remain intractable analytically. Hence, we resort to further approximations such as those required to yield the KdV and NLS equations. Generally, approximations are formalized by perturbation expansions in terms of a small parameter(s). In application of these approximate models, questions naturally arise as to when the inequalities used in ordering the physics are actually satisfied; i.e., how small is small? For evolution models, the relevant question distills into "during what time interval does a particular approximation correctly represent the general solution?" Closely related to this topic are questions of similitude between laboratory models and their geophysical-scale counterparts. The answers to all

of these questions involve determination of nondimensional parameters which characterize the phenomenon in question. In practice these parameters are often deduced through the ingenious use of dimensional analysis, by examination of the governing equations, or using the most preferred but least available method, examination of exact solutions of the general and approximate model equations. Here we examine the KdV equation and exploit exact solutions of its various approximations in order to develop rather precise criteria for modelling the propagation of long water waves. These criteria are then applied to the problem of tsunami propagation across ocean basins--the topic which precipitated the analysis. Further details are presented by Hammack and Segur.<sup>10</sup>

1. — Analysis.

In order to obtain definitive results, we adopt the following point of view. If the initial wave  $f_0$  is sufficiently smooth and localized, and if  $\epsilon_1 = a/h$  and  $\epsilon_2 = (kh)^2$  based on the initial data are both small, then the KdV equation (4) will be the approximate model eventually. (In fact, we know that (4) is appropriate when  $\epsilon_1 = 0(\epsilon_2)$ .) If  $\epsilon_1$  and  $\epsilon_2$  are not the same order of magnitude initially, then simpler forms of the KdV equation may be applicable for some time interval, e.g.,

$$(13) \quad f_\tau = 0 \quad (\text{linear, nondispersive model})$$

$$(14) \quad f_\tau + f_{XXX} = 0 \quad (\text{linear, dispersive model})$$

$$(15) \quad f_\tau + ff_X = 0 \quad (\text{nonlinear, nondispersive model})$$

Ursell<sup>11</sup> showed that the nondimensional parameter

$$(16) \quad u = \epsilon_1/\epsilon_2 = ak^{-2}/h^3$$

which we shall call the Ursell number, is an important indicator to determine which of these models is appropriate. One should use (14), (4), or (15), depending on whether  $U \ll 1$ ,  $U = 0(1)$ , or  $U \gg 1$ , respectively. Ursell also provided evidence that  $U$  is time dependent and will tend to an order-one limit so that all waves in this category eventually propagate according to (4) as postulated previously. Although there is general agreement with Ursell's results, there is disagreement on how to interpret "order unity" and how to define the relevant length scale  $k^{-1}$  for the evolving waves. To make his criteria more precise, we examine here initial data for which  $\epsilon_1 \ll \epsilon_2 \ll 1$  initially so that the linearized models (13) and (14) are the relevant approximations of (4). The dimensional length scale  $k_0^{-1}$  for the initial data is defined as its overall length, and the dimensional amplitude scale is  $a_0$ . Further, we will focus on criteria for modelling the leading wave only. Results for the trailing wave structure and the nonlinear approximation (15) are given in Hammack and Segur.<sup>10</sup>

1.1 Linear Dispersive Theory Since nonlinearity is small for the postulated initial data, we assume a small parameter  $\mu \ll 1$  exists and seek a formal series solution of the KdV equation (4) in the form

$$(17) \quad f = \mu f_1 + \mu^2 f_2 + O(\mu^3)$$

(The required definition of  $\mu$  will come out of the analysis.) Substituting (17) into (4) yields a hierarchy of problems.

$$(18) \quad (f_1)_\tau + (f_1)_{XXX} = 0, \mu f_1(x,0) = f_0$$

$$(19) \quad (f_2)_\tau + (f_2)_{XXX} = -6f_1(f_1)_X f_2(x,0) = 0$$

etc.

The solution of (18), which is equivalent to (14), is well known:

$$(20) \quad \mu f_1 = \frac{1}{2\pi} \int_{-\infty}^{\infty} \hat{f}_0(\kappa) \exp[i(\kappa x + \kappa^3 \tau)] d\kappa$$

where

$$(21) \quad \hat{f}_0(\kappa) = \int_{-\infty}^{\infty} f_0(x) \exp(-i\kappa x) dx$$

is the Fourier transform of the initial data. For practical reasons, we are most interested in the asymptotic form ( $\tau \rightarrow \infty$ ) of the solutions for both the linear and nonlinear models. As  $\tau \rightarrow \infty$  with  $|x|/\tau \rightarrow 0$  in order to remain at the wave front, the asymptotic form of (20) is

$$(22) \quad \mu f_1(x, \tau) = \hat{f}_0(0) (3\tau)^{-1/3} \text{Ai}(\xi) - i \hat{f}'_0(0) (3\tau)^{-2/3} \text{Ai}'(\xi) \\ - \frac{1}{2} \hat{f}''_0(0) (3\tau)^{-1} \text{Ai}''(\xi) + O[(3\tau)^{-4/3}]$$

where  $\xi = x/(3\tau)^{1/3}$  and  $\text{Ai}(\xi)$  is the Airy function. The coefficients in (22) have simple interpretations:

$$(23a) \quad \hat{f}(0) = \int_{-\infty}^{\infty} f_0 d = V$$

$$(23b) \quad -i\hat{f}'(0) = \int_{-\infty}^{\infty} x f_0 dx = \beta_1 U_0$$

$$(23c) \quad -\frac{1}{2}\hat{f}''(0) = \int_{-\infty}^{\infty} x^2 f_0 dx = \beta_2 \frac{U_0^2}{V}$$

where  $V$  is the nondimensional volume of the initial wave,  $U_0$  is an Ursell number for the initial wave, and  $\beta_1, \beta_2$  are constants that depend on the details of the initial wave. Thus (22) becomes

$$(24) \quad \mu f_1(x, \tau) = v(3\tau)^{-1/3} \{Ai(\xi) + \beta_1 \left( \frac{U_0}{V} \right) (3\tau)^{-1/3} Ai'(\xi) + \beta_2 \left( \frac{U_0}{V} \right)^2 (3\tau)^{-2/3} Ai''(\xi) + \dots\}$$

From (24) it follows that the time required for this representation to become asymptotic (second term smaller than first, etc.) is at least

$$(25) \quad (3\tau)^{1/3} \gg U_0/|v|$$

A particular solution of (19) is

$$(26) \quad \mu^2 f_{2p}(x, \tau) = - \left\{ \int_{-\infty}^x \mu f_1(z, \tau) dz \right\}^2$$

and defining

$$(27) \quad \theta(x) = \frac{1}{V^2} \left\{ \int_{-\infty}^x f_0(z) dz \right\}^2$$

the homogeneous solution of (19) is

$$(28) \quad \mu^2 f_{2h}(x, \tau) = V^2 \int_{-\infty}^x Ai(z) dz + \frac{V^2}{2\pi} \int_{-\infty}^{\infty} \{ \hat{\theta}(\kappa) - (i\kappa)^{-1} \} \cdot \exp[i(\kappa x + \kappa^3 \tau)] d\kappa$$

Thus, as  $\tau \rightarrow \infty$ ,  $|x|/\tau \rightarrow 0$

$$(29) \quad \mu^2 f_2(x, \tau) = V^2 \left\{ - \left[ \int_{-\infty}^{\xi} Ai(z) dz \right]^2 + \int_{-\infty}^{\xi} Ai(z) dz + \dots \right\}$$

Comparing (24) and (29), the appropriate definition of  $\mu$  is found to be simply

$$(30) \quad \mu = V$$

In other words, linear dispersive theory along with its large-time asymptotics requires the dimensionless wave volume  $V$  to be small. (Note that  $V$  is independent of time.) Since the solution of (29) remains  $O(1)$  as  $\tau \rightarrow \infty$ , the series (17) cannot remain asymptotic after

$$(31) \quad (3\tau)^{1/3} \sim |V|^{-1}$$

Thus, if the initial wave has a dimensionless volume  $V$  (assumed  $\neq 0$ ) and Ursell number  $U_0$  based on its initial (given) dimensions, asymptotic linear dispersive theory is valid in an interval no longer than

$$(32) \quad U_0/|V| \ll (3\tau)^{1/3} \ll 1/|V|.$$

1.2 Nondispersive Linear Theory. Since our initial wave is postulated to be linear, then  $U_0 \ll 1$  and necessarily  $|V| \ll 1$ , as well. The derivation of the KdV equation outlined in Part II indicated that linear nondispersive theory (13) occurs on the first time scale of evolution. Hence we may write

$$(33) \quad 3\tau \ll \varepsilon_2 = (k_0 h)^2 = (U_0/V)^2$$

for (13) to be applicable.

## 2. Summary and Application of Criteria to Tsunamic Propagation

In summary, we have examined the evolution of long-wave initial data which is parameterized by an initial Ursell number  $U_0 \ll 1$  and volume (or mass)  $V \ll 1$ . We may model the evolution of this initial data using linear nondispersive theory ( $f_\tau = 0$ ) during a time interval

$$(34) \quad 0 \leq 3\tau \ll \tau_1 = \left( \frac{U_0}{V} \right)^2.$$

The next relevant model is linear dispersive theory ( $f_{\tau} + f_{XXX} = 0$ )

which is valid during

$$(35) \quad \tau_1 \ll 3\tau \ll \tau_2 = \left( \frac{U_0}{V} \right)^3$$

with its asymptotics becoming valid during

$$(36) \quad \tau_2 \ll 3\tau \ll \tau_3 = \frac{1}{V^2}.$$

Subsequently, we must use the KdV equation ( $f_{\tau} + 6ff_x + f_{XXX} = 0$ ) for

$$(37) \quad 3\tau \gg \tau_3$$

(The question of the time scale for applicability of KdV asymptotics is discussed by Hammack and Segur<sup>10</sup>.) As an example of the application of these results, consider the dimensional scales adopted by Carrier<sup>12</sup> for major tsunamis which impact entire ocean basins:  $a_0 \approx 10$  ft.,  $h \approx 1.5 \cdot 10^4$  ft.,  $k_0^{-1} = 2 \cdot 10^5$  ft.

Then  $U_0 \approx 0.1$  and  $V \approx 0.01$  and linear nondispersive theory is valid for times corresponding to propagation distances (using  $c_1^2 = gh$ ) of

$$0 < x \ll 600 \text{ miles.}$$

Linear dispersive theory is appropriate for

$$600 \text{ miles} \ll x \ll 6,000 \text{ miles}$$

indicating that dispersion may affect this wave over much of typical ocean

trajectories. Even so, linear asymptotics do not apply until  $x \gg 6,000$  miles, which exceeds the length of realistic trajectories. Hence, linear dispersive asymptotics and the KdV equation are not required for describing the lead wave of the tsunami discussed here. (The KdV equation may be used, but it is unnecessarily complicated.) Of course, other factors may be required to accurately model long-term tsunami propagation (such as the variable bathymetry along trajectories and three-dimensional spreading of wave energy); the intent of the analysis here is only to develop insight into the relative importance of dispersion and nonlinearity.

#### IV. — Excitation of Standing Edge Waves on Beaches

##### 1. — Introduction

In recent years considerable attention has been focused on the occurrence of ocean waves which become trapped and capable of concentrating energy in localized regions (wave guides). Wave trapping can occur whenever gradients exist in a parameter which affects the wave's phase speed, e.g., Coriolis parameter, Brunt-Vaisala frequency, current speeds, and water depth. Stokes<sup>13</sup> provided the first theoretical evidence of trapping for surface (gravity) waves near the shoreline of a plane sloping beach. Stokes found a normal mode solution for the (barotropic) departure  $\eta$  of the water surface from its static equilibrium position (see figure 11a) of the form

$$(38) \quad \eta_m(x, y, t) = a \sin \beta \exp(-k_m y \cos \beta) \cos k_m x \sin \omega_m t$$

where  $-\tan \beta$  is the beach slope,  $x$  points in the longshore direction, and  $y$  points offshore. The (linear) dispersion relation for the various longshore mode number  $m = 1, 2, \dots$  is

$$(34) \quad 0 \leq 3\tau \ll \tau_1 = \left( \frac{U_0}{V} \right)^2.$$

The next relevant model is linear dispersive theory ( $f_{\tau} + f_{XXX} = 0$ )

which is valid during

$$(35) \quad \tau_1 \ll 3\tau \ll \tau_2 = \left( \frac{U_0}{V} \right)^3$$

with its asymptotics becoming valid during

$$(36) \quad \tau_2 \ll 3\tau \ll \tau_3 = \frac{1}{V^2}.$$

Subsequently, we must use the KdV equation ( $f_{\tau} + 6ff_X + f_{XXX} = 0$ ) for

$$(37) \quad 3\tau \gg \tau_3$$

(The question of the time scale for applicability of KdV asymptotics is discussed by Hammack and Segur<sup>10</sup>.) As an example of the application of these results, consider the dimensional scales adopted by Carrier<sup>12</sup> for major tsunamis which impact entire ocean basins:  $a_0 \approx 10$  ft.,  $h \approx 1.5 \cdot 10^4$  ft.,  $k_0^{-1} = 2 \cdot 10^5$  ft. Then  $U_0 \approx 0.1$  and  $V \approx 0.01$  and linear nondispersive theory is valid for times corresponding to propagation distances (using  $C_1^2 = gh$ ) of

$$0 < x \ll 600 \text{ miles.}$$

Linear dispersive theory is appropriate for

$$600 \text{ miles} \ll x \ll 6,000 \text{ miles}$$

indicating that dispersion may affect this wave over much of typical ocean

$$(39) \quad \omega_m^2 = gk_m \sin \beta$$

where  $k_m = m\pi/b$  is fixed by the beach width  $b$ . Note that the Stokes' mode of (38) is periodic in the longshore direction with crests pointing offshore which decay in amplitude with an e-folding distance  $y_e = (k_m \cos \beta)^{-1}$ . The crest amplitude is maximum at the shoreline with a magnitude  $\alpha \sin \beta$  where  $\alpha$  is referred to as the run-up amplitude. (Of course, run-up phenomena cannot be represented by linear solutions; however, the reality of run-up is acknowledged since  $\alpha$  is the up-beach length of the horizontal projection of the vertical shoreline amplitude.) Ursell<sup>14</sup> demonstrated that the Stokes' mode is only the lowest ( $j = 0$ ) of a discrete set  $j = 0, 1, \dots, J$  of trapped modes where  $J$  is the greatest integer satisfying

$$(40) \quad (2J + 1) \beta \leq \frac{\pi}{2}.$$

These higher discrete modes are algebraically complicated but retain longshore periodic behavior. Their crest amplitude is maximum at the shoreline but oscillates in the offshore direction with  $j$  nodes while decaying exponentially (see figure 11b). To complete the set of normal modes, Hanson<sup>15</sup> showed that there exists a continuous spectrum of waves with wave-number magnitude  $k$  satisfying  $\omega^2 > gk$ . These modes are even more complicated to describe algebraically but resemble simple deep-water wave trains far offshore. An example of one of these modes with crests parallel to the shoreline is shown in figure 11b. We emphasize here that the continuous spectrum modes are not trapped like the discrete modes.

Oceanographic interest in edge waves appears to have originated in Isaacs *et al.*<sup>16</sup> suggestion that these waves might be responsible for "surf beat" phenomena. Since then, edge waves have been indicted as a potential mechanism for numerous features of coastal dynamics such as beach cusps (Guza and Inman)<sup>17</sup>, crescentic bars (Bowen and Inman)<sup>18</sup>, and rip currents (Bowen and Inman)<sup>19</sup>. The lack of direct observational evidence of edge wave modes on beaches (i.e., wave crests pointing offshore!) naturally raises questions as to how and if these modes can be excited. The most important mechanism for extensive generation opportunities of edge waves was provided by Guza and Davis<sup>20</sup> who demonstrated theoretically that Stokes' modes could be excited by simple wave trains normally incident onto a perfectly reflecting beach from deep water. Basically, the nonlinear coupling between the incident/reflected wave of frequency  $W$  and background edge wave "noise" of subharmonic frequency  $\omega = W/2$  leads to a resonant interaction and growth of the edge wave noise. Eventually other nonlinear processes develop to limit growth; however, at steady state the edge wave amplitude exceeds that of the incident/reflected wave. The entire evolution of the edge wave has been investigated theoretically by Guza and Bowen<sup>21</sup> (hereafter referred to as G-B), Minzoni and Whitman<sup>22</sup> (hereafter referred to as M-W), and Rockliff<sup>23</sup>.

Herein we present quantitative experimental measurements on edge wave excitation by normally incident wave trains. Some of the predictions of G-B and M-W are tested and necessary modifications for imperfectly reflecting beaches are presented. An outline of the presentation is as follows. In Sect. 2 we review the theoretical results with emphasis on the prediction which can be explicitly tested by the experiments. In Sect. 3 a brief description of the experimental

facilities and data analysis techniques are discussed. A comparison of measured and predicted data appears in Sect. 4 followed by a summary of the major results in Sect. 5. More details of each aspect of this note may be found in Lin and Hammack.<sup>24</sup>

## 2. — Review of the Theories

The first description of both edge wave excitation and subsequent evolution was developed by Guza and Bowen<sup>21</sup> using the shallow-water equations; hence, their results are limited to small beach angles ( $\beta \ll 1$ ). With clever but intuitive reasoning, G-B isolate several processes, analyze each separately, and combine linearly to yield a complete evolution model. (More recently, Rockliff<sup>23</sup> has reproduced some of the G-B results relying more formally on the governing shallow-water equations.) Minzoni and Whitham<sup>22</sup> use the full equations and provide the most formal (mathematically) description of the edge wave evolution process; their results remain valid for arbitrary beach slopes  $\beta \leq \pi/2$ . The greater formality of the M-W formulation permits more justifiable ordering of different processes. Hence, the outline below of edge wave evolution is based primarily on their formalism. Following the qualitative description, a quantitative listing of relevant parameters predicted by both M-W and G-B will be presented.

The classical water-wave problem for the inviscid, irrotational, barotropic motions of an incompressible ocean in the wedge-shaped region of figure 11a may be formulated in terms of a complex velocity potential  $\phi$ . Initially, we have a linear wave train normally incident onto the beach from deep water; the incident wave amplitude far offshore is  $a_i$ . We also take the incident wave to be perfectly reflected from the beach. (The reflection coefficient is  $R = a_r/a_i = 1$  where  $a_r$  is reflected wave amplitude.) Hence, the forcing for the onshore edge wave noise is a standing wave mode which is a member of the continuous spectrum of normal modes

discussed in Sect. 1. To simplify (somewhat) the standing wave description, it is further assumed that the beach slopes are a member of the denumerably infinite set  $\beta = \pi/2N$  with  $N = 1, 2, \dots$ . The complex potential for the standing wave may be written as  $\phi_s \sim \exp(i\omega t)$ , and we note that  $|\phi_s| \sim \epsilon \ll 1$ . In addition to the primary standing wave, we assume three-dimensional perturbations by Stokes edge wave with complex potential  $\phi_e \sim \exp(i\omega t)$  where  $|\phi_e| \ll \epsilon \ll 1$  initially. On a very short time scale (stage 1), nonlinear interactions between the primary wave and the edge wave noise are negligible. However, on a longer time scale (stage 2), quadratic interactions arise as a consequence of the nonlinear boundary condition at the free surface and become significant. Assuming the edge wave noise that satisfies the resonance condition  $\omega = \omega/2$  to dominate, quadratic interactions  $\phi_s \phi_e^*$  (where  $*$  denotes complex conjugate) give rise to terms of the form  $\exp(i\omega t/2)$  and contribute to the growth of the subharmonic edge wave noise. This interaction between the linear standing wave and linear edge wave noise produces exponential growth of the form  $a \sim \exp(\gamma t)$  where  $a$  is the (real) edge wave amplitude at any crest location (i.e.,  $a = a(x, y, t)$ , and we take  $a(x, 0, t) \equiv A(x, t)$  as the shoreline amplitude) and  $\gamma$  is the initial growth rate. The edge wave noise grows until a later time scale (stage 3) is reached where its finite amplitude leads to the development of processes which limit further growth. First, quadratic self-interactions of the edge wave with the form  $\phi_e \phi_e \sim \exp(i\omega t)$  contribute to the offshore standing wave; this is termed radiation by G-B and corresponds to the fact that nonlinear (even second order) standing edge waves leak energy at frequency  $2\omega$  to deep water. Since  $|\phi_s| \sim \epsilon$  for the disturbed standing wave in stage 3, radiation feedback suggests that a steady state may be reached when  $|\phi_e| \sim \epsilon^{\frac{1}{2}}$ , i.e., the edge wave becomes larger locally than the forcing wave. Second, cubic self-interaction terms of the form

$\phi_e \phi_e \phi_e^* \sim \exp(iWt/2)$  contribute further to edge wave nonlinearity by modifying its dispersion relation. Hence, the system is retuned and the resonant frequency is shifted. If the forcing was perfectly resonant initially, it will now be off resonance and an effective reduction of the on-resonance growth rate  $\gamma$  will occur. (Of course, if the initial forcing is slightly off-resonance, a similar modification in  $\gamma$  is required.) When combined, all of these processes lead to an evolution for (inviscid) edge waves of the form

$$(41) \quad \frac{dA}{dt} = (\gamma^2 - \kappa^2)^{\frac{1}{2}} A - \mu A^3$$

where  $\gamma$  is the initial on-resonance growth rate,  $\kappa$  is a measure of the reduction in forcing efficiency due to nonlinear retuning, and  $\mu$  is a feedback coefficient due to both radiation and retuning. (Note that in (41) we tacitly assume that the edge wave phase remains constant through stage 3. Theoretically, this assumption is invalid; however, the experimental data support its applicability.)

At the risk of misquoting G-B and M-W and possibly introducing numerical errors, we now list quantitative expressions distilled from their studies for the parameters appearing in (41). The initial (on-resonance) growth rate predicted for the edge waves is

$$(42a) \quad \text{G-B:} \quad \gamma = \frac{0.0424 a_i w^3}{g\sqrt{\beta} \beta^2},$$

$$(42b) \quad \text{M-W} \quad \gamma = \frac{0.0426 a_i w^3}{g\sqrt{\beta} \tan^2 \beta}.$$

where the M-W result is accurate to within 3% for  $\beta \leq \pi/4$ . These predictions are in agreement in the shallow-water limit ( $\beta \rightarrow 0$ ). Modification of the

initial growth rate by nonlinear retuning in steady state may be conveniently written to the same order of small parameter  $\epsilon_0 = \alpha_0 k$  (where  $\alpha_0$  is the steady-state run-up amplitude of the edge wave) as

$$(43) \quad \kappa = \omega^{(2)} - \omega^{(0)}$$

with  $\omega^{(2)}$  and  $\omega^{(0)}$  representing the nonlinear and linear natural frequencies of the edge wave, respectively. The shallow-water limits for  $\omega^{(2)}$  given explicitly by G-B and inferred from the presentation of M-W are

$$(44a) \quad \text{G-B:} \quad \omega^{(2)} = \omega^{(0)} [1 + 0.055 \epsilon_0^2]$$

$$(44b) \quad \text{M-W:} \quad \omega^{(2)} = \omega^{(0)} [1 + 0.012 \epsilon_0^2];$$

$\omega^{(0)} = (g k \beta)^{1/2}$  in both cases. The different results of (44a) and (44b) do not appear reconcilable. Predictions for the feedback coefficient  $\mu$  in the shallow-water limit also differ at the same order of approximation according to

$$(45a) \quad \text{G-B:} \quad \mu = 0.001795 \frac{W^5}{g^2 \beta^4}$$

$$(45b) \quad \text{N-W:} \quad \mu = 0.002323 \frac{W^5}{g^2 \beta^4}$$

Finally, we note that the steady-state amplitude of the edge wave at the shoreline is found from (41) to be

$$(46a) \quad A_0 = \left[ \frac{(\gamma^2 - \kappa^2)^{1/2}}{\mu} \right]^{1/2}$$

### 3. — Experimental Facilities and Procedures

A set of five experiments are conducted to study the excitation of standing edge waves on a beach by waves normally incident from offshore. Experiments are performed in a laboratory basin 1.83 m wide, 4.0 m long and 30 cm deep as sketched in figure 12. The tank is equipped with a mechanical wave generator and a smooth beach whose slope can be varied. An actual beach width of  $b = 1.60$  m was used in the experiments by incorporating internal sidewalls over the beach section as indicated in figure 12. This enables the offshore tank section of uniform depth to be surrounded by energy-absorbing material to minimize unwanted reflections and simulate open-ocean conditions. Extensive precautions were taken to insure that the shoreline and wavemaker were parallel and to prevent beach "pumping" during actual experiments.

An offshore water depth of  $h = 25.4$  cm was used in all five experiments while the beach slope was varied from  $\beta = 15^\circ$  ( $N = 6$ ) to  $\beta = 22.5^\circ$  ( $N = 4$ ); one experiment, run 4, was conducted at  $\beta = 20^\circ$  which does not correspond to a slope of  $\pi/2N$  for any integer  $N$ . It is immediately apparent that the offshore uniform depth region does not conform to the (unrealistic) mathematical model where the water depth increases linearly offshore. However, the offshore distance over the sloping beach section always exceeded three e-folding distances ( $> 95\%$  decay) for the edge wave modes excited (assuming Stokes' modes). Based on Minzoni,<sup>25</sup> it is not expected that the edge wave dispersion relation is affected by the uniform depth offshore in any of the experiments.

In all experiments wave amplitudes are measured at three locations; one gage onshore over the sloping beach and two gages offshore in the uniform depth region. The onshore gage is always positioned at a longshore location

corresponding to an edge wave antinode. The reality of edge waves very near the shoreline requires that they deviate from the profile predicted by (38); hence, the onshore gage is located approximately one e-folding distance away from the shoreline and always outside of the surf zone.

The procedures adopted for each of the five experimental runs are as follows. First, the frequency  $\omega$  of the desired edge wave is calculated based on the beach width  $b = 1.6$  m; the offshore wavemaker is then adjusted to a frequency  $W = 2\omega$ . The incident and reflected wave amplitudes ( $a_i$  and  $a_r$ ) of the partial standing wave systems are then determined from simultaneous measurements at the offshore gages in the absence of edge wave excitation. Edge wave excitation is suppressed by inserting a thin plate perpendicular to the shoreline which penetrates the surf zone; the plate introduces boundary conditions which destroy the resonance condition necessary for rapid edge wave growth. The thin plate is then removed permitting the evolution of the edge wave. Once the edge wave attains a steady state the wavemaker is stopped and the (unforced) decay of the edge wave over the sloping beach is measured. Hence, each experiment produces a time series of the water surface elevation onshore and offshore containing stage 1, stage 2, stage 3, and additional stage 4 where edge wave forcing is terminated and viscous damping forces dominate.

#### 4. — Comparison of Experiment and Theory

Table 1 summarizes the measured data for the partial standing waves generated by the wavemaker/beach system in the absence of edge waves. The incident and reflected wave amplitudes are presented along with the respective reflection coefficients which range from  $R = 0.134$  to  $R = 0.500$ . (Recall that

theoretical results assume perfect reflection with  $R = 1.$ ) It should be noted that wave breaking near the shoreline was observed in each experiment and was especially strong in run 1.

A typical time series (run 2) taken onshore and offshore during edge wave excitation, evolution, and eventual damping is shown in figure 13. The onshore record clearly shows the effect of edge wave growth as it alternates between construction and destructive interference with successive crests of the incident/reflected wave system. (This behavior is a direct consequence of subharmonic excitation with  $W = 2\omega.$ ) A periodogram computed using the Fast Fourier Transform of the onshore wave record for run 2 is shown in figure 14. The first peak in the spectrum corresponds to the excited edge wave mode while the second peak corresponds to the standing wave generated from offshore. The equally spaced peaks at higher frequencies represent the superharmonics of both the edge wave and standing wave. The centering of wave content about well-separated and narrow bands with identifiable dominant frequencies ( $\omega, 2\omega, 3\omega, \dots$ ) such as that exhibited in figure 14 permits the use of complex demodulation techniques to view the real time evolution of both the amplitude and phase of each dominant wave component (see Bloomfield<sup>26</sup>). Using the periodogram, an initial guess, say  $\omega_g$ , for the dominant frequency in a band of interest is determined. The time series is then multiplied by  $\exp(-i\omega_g t)$  to shift the desired wave content to zero frequency. This demodulated signal is then low-pass filtered in time to yield the instantaneous phase and amplitude of the signal component with frequency  $\omega_g$ . If the estimated frequency  $\omega_g$  is in error, a linear change in instantaneous phase with time will be observed; the slope of the linear change represents the error in  $\omega_g$ . In this manner the dominant

frequency of each narrow band in the periodogram may be determined very accurately as well as its instantaneous amplitude and phase. (More details on the application of complex demodulation technique including a discussion of the low-pass filter properties may be found in Lin and Hammack.<sup>24</sup>) The edge wave frequencies in each experiment were determined using this technique and are summarized in table 2. Figures 15 and 16 show the instantaneous amplitude and phase, respectively, of the edge wave harmonic at the onshore gage in run 2. Both parameters oscillate rather wildly during the initial time  $t < 25$  secs; this behavior is a characteristic result when the signal-to-noise ratio is small. (Note that during this period this instantaneous amplitude of the edge wave is less than 0.07 cm!) The edge wave amplitude in figure 15 then begins to grow in an exponential manner while the edge wave phase in figure 16 becomes constant. As time continues to increase, edge wave growth slows and a steady state is achieved for  $t > 70$  secs; the gage-site amplitude of the edge wave at steady-state is  $a_0 = 0.754$  cm. The measured growth rates  $\gamma_m$  and steady-state amplitudes  $a_0$  are shown in table 2. The inferred shoreline amplitude  $A_0$  based on the measured  $a_0$  at gage-site is easily calculated; the ratio of  $A_0/a_i$  ranges from 3-6 in all experiments in agreement with the theoretical prediction that steady-state amplitudes of the edge wave should exceed those of the offshore standing wave. It is important to note that measured growth rates are significantly influenced by viscous and turbulent damping forces which must be clarified before a legitimate comparison with inviscid and irrotational theoretical models. The viscous damping rate is easily measured in the laboratory model simply by turning off the wavemaker and monitoring the damping of the edge wave harmonic with time. Typical

results are shown in figure 17 which corresponds to run 2. As expected, exponential decay occurs when the edge wave becomes sufficiently small (and linear theory is applicable). The measured decay rates  $\delta$  in the exponential stage for each experiment are presented in table 2. As noted by Guza and Bowen,<sup>27</sup> the damping of edge waves in the presence of breaking incident waves is likely to be dominated by turbulent exchange mechanisms rather than (laminar) viscosity. Viscous effects are enhanced by laboratory model scales and should play an important role; however, based on the results to follow, turbulent exchange mechanisms also appear to be important at laboratory scales. Ignoring the effects on laboratory damping of edge waves due to incident wave breaking, a measured "inviscid" estimate of the initial growth rate may be calculated by  $\gamma'_m = \gamma_m + \delta$ . Results for  $\gamma'_m$  are tabulated in table 2 along with the theoretical predictions for the growth rate according to 42a. It is evident that large discrepancies still exist; however, it should also be remembered that the theoretical predictions assume a perfectly reflecting beach. To examine the potential effect of the imperfect reflection in the experiments we have plotted the ratio of  $\gamma'_m / \gamma$  versus the reflection coefficient  $R$  in figure 18. Note that excellent correlation exists (data lie on  $45^\circ$  line) suggesting that the growth rates should be calculated using the reflected wave amplitude  $a_r$  instead of the incident wave amplitude  $a_i$ , i.e., we should replace  $\gamma$  by  $\gamma R$ . Theoretical estimates of  $\gamma R$  are listed in table 2. It is important to emphasize that this behavior of the measured data clearly demonstrates that it is the reflected wave component of the offshore standing wave which drives the edge waves. It further supports the observation (Guza and Inman<sup>17</sup>) that edge waves do not occur on dissipative beaches which produce little reflection.

In order to compute the theoretical amplitude of the edge waves in steady state, the results above suggest that we should modify the theoretical growth rate in (46) to the form

$$(46b) \quad A_0 = \left[ \frac{R(\gamma^2 - \kappa^2)}{\mu} \right]^{\frac{1}{2}}$$

The theoretical amplitude at a specific gage site then becomes

$$(47) \quad a_0 = A_0 \cos k_m x \exp(-k_m y \cos \beta);$$

results of computations for the predictions of both G-B and M-W are shown in table 2. Except for run 4, theoretical results exceed measured data by factors of 1.18 to 1.91. This behavior pattern is expected since the turbulent damping of the edge waves in the presence of breaking incident waves has been neglected. Also consistent with this hypothesis is the fact that agreement between experiment and prediction is best in run 5 where the least wave breaking was observed. Run 4 is anomalous as the measured amplitude exceeds theoretical prediction. (Interestingly, absolute agreement between measured and predicted data is best for run 4!) There is also the following evidence that run 4 is unusual re. re. to the other experiments. Note from table 1 that the offshore standing wave changes little between runs 3 and 4 while the steady-state amplitude of the edge wave in table 2 doubles! In other words, a major difference in the wave field occurs even though the forcing remains approximately constant. The difference between runs 3 and 4 is the slightly greater

beach slope ( $2^0$ ) in run 4 which no longer corresponds to one of the set  $\pi/2N$  required by the theoretical models. Based on this limited datum, it does appear that the predictions for steady-state response on beach with slopes satisfying  $\beta = \pi/2N$  cannot be extrapolated to intermediate slopes. (However, extrapolation for the initial growth rates does appear permissible with the modifications due to partial reflection described earlier.)

##### 5. — Conclusions

Based on the experiments described herein, the following major conclusions may be stated regarding edge wave excitation on beaches by normally incident waves from offshore.

- i) The theoretical growth rates calculated for perfectly reflecting beaches may be generalized to beaches with imperfect reflection simply by reducing the growth rates in direct proportion to the reflection coefficient of the beach. This result suggests that the reflected wave is indeed the driving force for edge wave response and absolutely necessary in order to excite these modes.
- ii) Growth rates modified for partial reflection effects may be extrapolated to beaches with slopes not satisfying  $\beta = \pi/2N$ .
- iii) No change in the edge wave phase occurs once the exponential growth stage is encountered. Hence, the evolution equation for the real amplitude of the edge wave is applicable.
- iv) There is limited evidence that the steady-state amplitudes of edge waves on beaches with  $\beta \neq \pi/2N$  are significantly larger than those for nearby beach slopes with  $\beta = \pi/2N$ .

- v) Damping effects on edge waves are significantly influenced by turbulent exchange mechanisms resulting from breaking incident waves, even on the laboratory scale.

\* \* \*

Financial support for much of the work reported in these lectures was provided by the Office of Naval Research, Fluid Dynamics Division, and the National Science Foundation, Engineering Division. The Center for Studies of Nonlinear Dynamics at the La Jolla Institute also provided support for the preparation of the lecture notes. The experiments reported in Part IV were performed by N.K. Lin, at the University of California. The author gratefully acknowledges the support and assistance from each of these sources.

REFERENCES

- [1] H. Segur: *J. Fluid Mech.*, 59(4), p. 721 (1973).
- [2] J. Hammack and H. Segur: *J. Fluid Mech.*, 65(2), p. 289 (1974).
- [3] J. Hammack: *J. Phys. Oceanogr.*, to appear (1980).
- [4] J. Hammack and H. Segur: in preparation.
- [5] J. Hammack and H. Segur: *J. Fluid Mech.*, 84(2), p. 337 (1978).
- [6] G. G. Stokes: *Trans. Camb. Phil. Soc.*, 8, p. 441 (1849).
- [7] H. Hasimoto and H. Ono: *J. Phys. Soc. Japan*, 33(3), p. 805 (1972).
- [8] H. Yuen and B. Lake: *Phys. Fluids*, 18, p. 956 (1975).
- [9] H. Yuen and B. Lake: *Ann. Rev. Fluid Mech.*, 12, p. 303 (1980).
- [10] J. Hammack and H. Segur: *J. Fluid Mech.*, 84(2), p. 359 (1978).
- [11] F. Ursell: *Proc. Camb. Phil. Soc.*, 49, p. 685 (1953).
- [12] G. Carrier: *Lect. Appl. Math. Am. Math. Soc.*, 14, p. 157 (1971).
- [13] G. G. Stokes: *Brit. Ass. Rep.*, part 1, p. 1 (1846).
- [14] F. Ursell: *Proc. Roy. Soc.*, A214, p. 79 (1952).
- [15] E. T. Hanson: *Proc. Roy. Soc.*, A111, p. 49 (1926).
- [16] J. D. Isaacs, E. A. Williams, and C. Ekart: *EOS Trans. AUG*, 32, p. 37 (1951).
- [17] R. T. Guza and D. L. Inman: *J. Geophys. Res.*, 80(21), p. 2997.
- [18] A. J. Bowen and D. L. Inman: *J. Geophys. Res.*, 76(36), p. 8662 (1961).
- [19] A. J. Bowen and D. L. Inman: *J. Geophys. Res.*, 74(23), p. 5479 (1969).
- [20] R. T. Guza and R. E. Davis: *J. Geophys. Res.*, 79(9), p. 1285 (1974).
- [21] R. T. Guza and A. J. Bowen: *J. Mar. Res.*, 34(2), p. 269 (1976).

- [22] A. A. Minzoni and G. B. Whitman: *J. Fluid Mech.*, 79(2), p. 273 (1977).
- [23] R. Rockliff: *Math. Proc. Camb. Phil. Soc.*, 83, 463 (1978).
- [24] N. K. Lin and J. L. Hammack, in preparation.
- [25] A. A. Minzoni: *J. Fluid Mech.*, 74(2), p. 369 (1976).
- [26] P. Bloomfield: *Fourier Analysis of Time Series: An Introduction* (New York, 1976), p. 118.
- [27] R. T. Guza and A. J. Bowen: *Proc. 15th Coast. Engng. Conf.*, p. 560 (1976).

Run	$\beta$	W $\left( \frac{\text{rad}}{\text{sec}} \right)$	$a_i$ (cm)	$a_r$ (cm)	R
1	$15^{\circ}$	9.98	0.82	0.11	0.134
2	$15^{\circ}$	7.54	0.62	0.31	0.500
3	$18^{\circ}$	9.82	0.87	0.30	0.345
4	$20^{\circ}$	10.65	0.90	0.32	0.356
5	$22.5^{\circ}$	10.86	0.63	0.29	0.460

Table 1. Beach and offshore standing wave properties

Run	$m$	$\omega$ (rad/sec)	$\gamma_m$ (sec $^{-1}$ )	$\delta$ (sec $^{-1}$ )	$\gamma'_m$ (sec $^{-1}$ )	$\gamma$ (sec $^{-1}$ )	$\gamma_R$ (sec $^{-1}$ )	$a_0$ meas (cm)	$a_0$ G-B (cm)	$a_0$ M-W (cm)
1	5	4.93	0.0295	0.1086	0.1381	0.9652	0.1293	0.28	0.55	0.49
2	3	3.80	0.0880	0.0771	0.1651	0.3144	0.1572	0.75	1.52	1.36
3	4	4.83	0.1120	0.0677	0.1797	0.6051	0.2088	0.67	1.01	0.93
4	4	5.29	0.0910	0.1289	0.2199	0.6031	0.2147	1.38	1.14	1.26
5	4	5.42	0.1000	0.0693	0.1693	0.3264	0.1501	0.90	1.07	1.05

Table 2. Measured and predicted properties of excited edge waves

FIGURE CAPTIONS

Figure 1. Definition sketch of the fluid domain.

Figure 2. Schematic drawing of the wave generator.

Figure 3. Surface wave evolution:  $h = 5 \text{ cm}$ ,  $b = 61 \text{ cm}$ ,  $V = 30.5 \text{ cm}^2$ ,  $N = 3$ . ———, measured profiles; ●, soliton profiles computed using (7).

Figure 4. Surface wave evolution:  $h = 5 \text{ cm}$ ,  $b = 30.5 \text{ cm}$ ,  $V = 30.5 \text{ cm}^2$ ,  $N = 3$ . ———, measured profiles; ●, soliton profiles computed using (7).

Figure 5. Surface wave evolution:  $h = 5 \text{ cm}$ ,  $b = 61 \text{ cm}$ ,  $V = 30.5 \text{ cm}^2$ ,  $N = 0$ .

Figure 6. Surface wave evolution:  $h = 5 \text{ cm}$ ,  $b = 30.5 \text{ cm}$ ,  $V = -30.5 \text{ cm}^2$ ,  $N = 1$ .

Figure 7. Surface wave evolution:  $h = 5 \text{ cm}$ ,  $b = 30.5 \text{ cm}^2$ ,  $V = 0$ ,  $N = 2$ .  
———, measured profiles; ●, soliton profiles computed using (7).

Figure 8. Internal wave evolution:  $h_1 = 45 \text{ cm}$ ,  $h_2 = 5 \text{ cm}$ ,  $b = 61 \text{ cm}$ ,  $\Delta = 0.05$

Figure 9. Comparison of leading wave profiles with theoretical (internal) KdV soliton.

Figure 10. Evolution of a narrow-banded wave packet. ———, measured profiles; ●, soliton profile computed using (12).

Figure 11a) Definition sketch of fluid domain and Stoke's edge-wave mode.

b) Sample offshore profiles of higher edge-wave modes: ———, discrete spectrum (trapped) mode; ——, continuous spectrum (untrapped) mode.

Figure 12. Schematic drawing of wave basin -- plan view.

Figure 13. Time-series of water surface elevations onshore and offshore.

Figure 14. Periodogram of onshore time series.

Figure 15. Amplitude evolution of subharmonic edge wave for run 2.

Figure 16. Phase evolution of subharmonic edge wave in run 2.

Figure 17. Viscous damping of subharmonic edge wave in run 2.

Figure 18. Correlation of measured and theoretical "inviscid" growth rates with beach reflection coefficient.

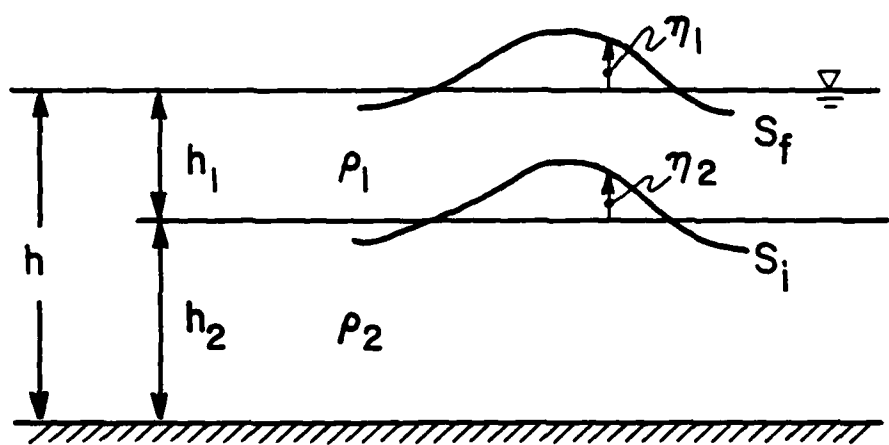


FIGURE 1

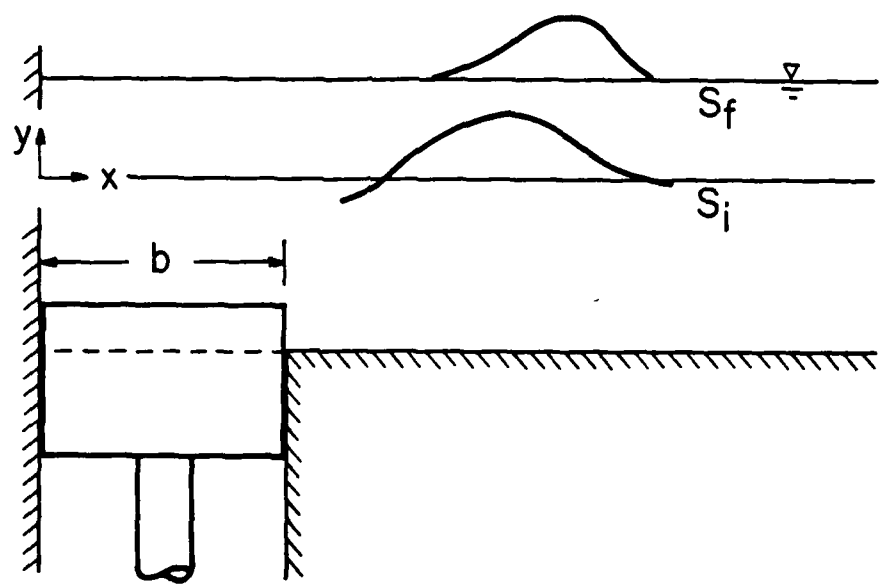


FIGURE 2

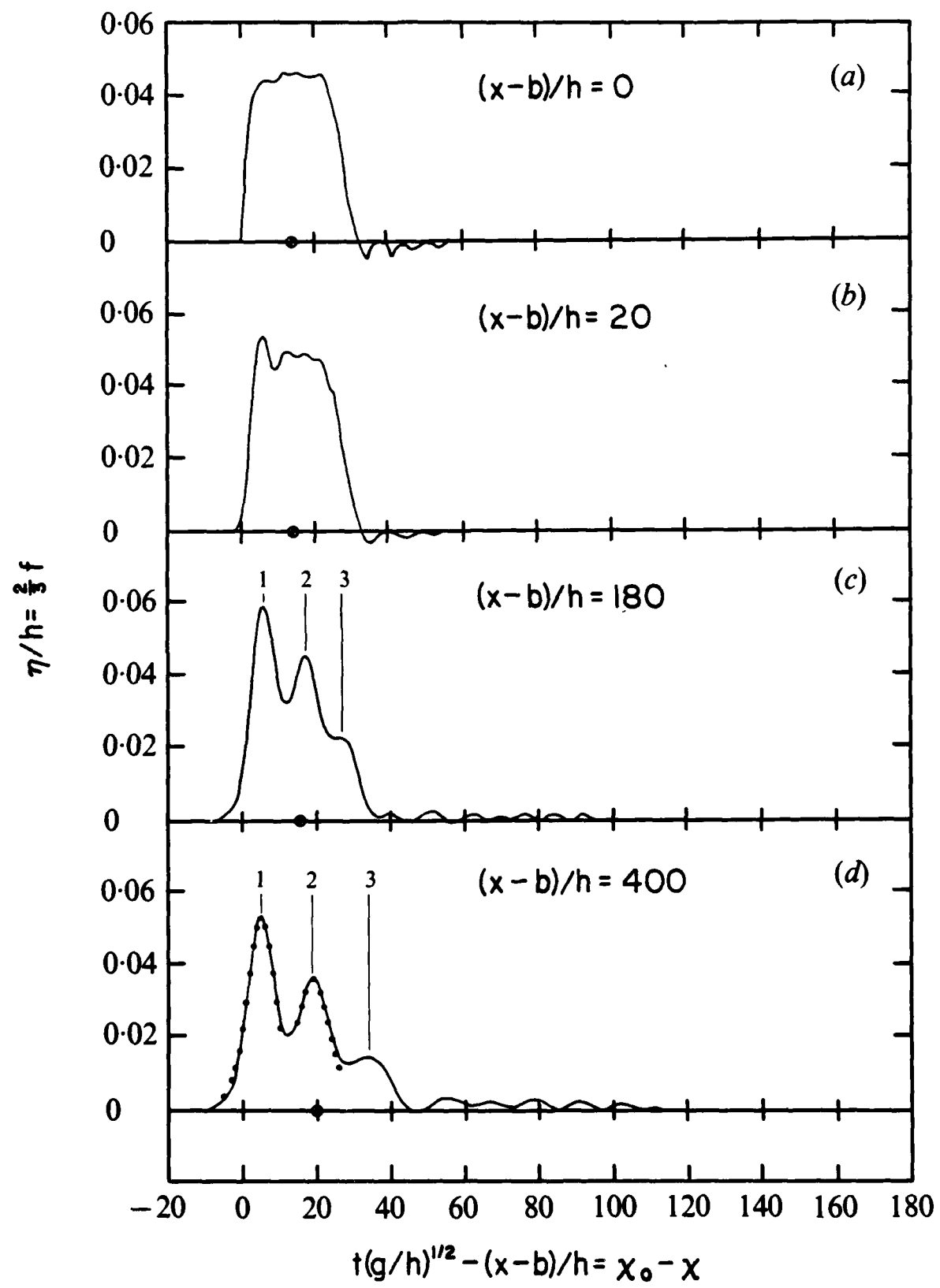
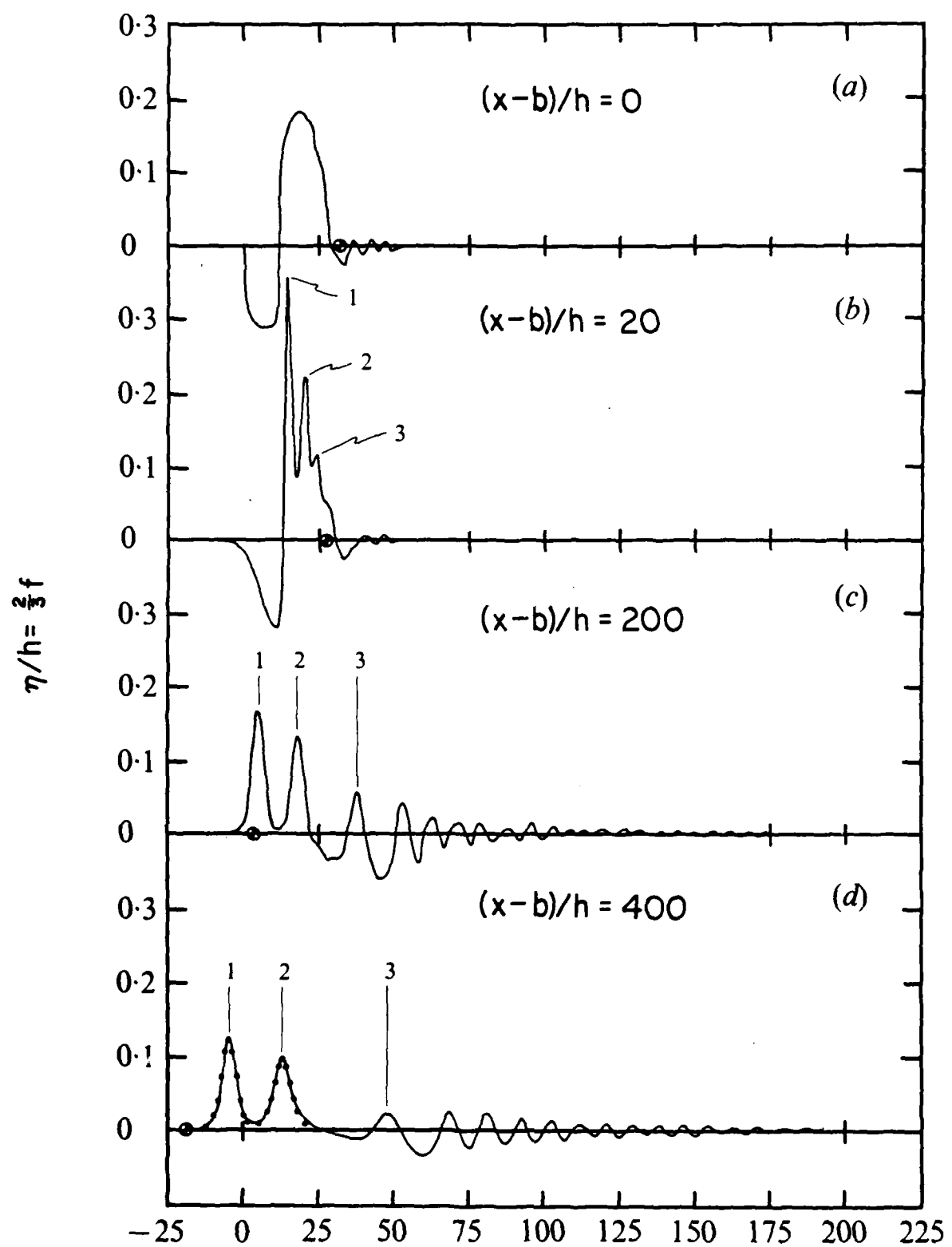
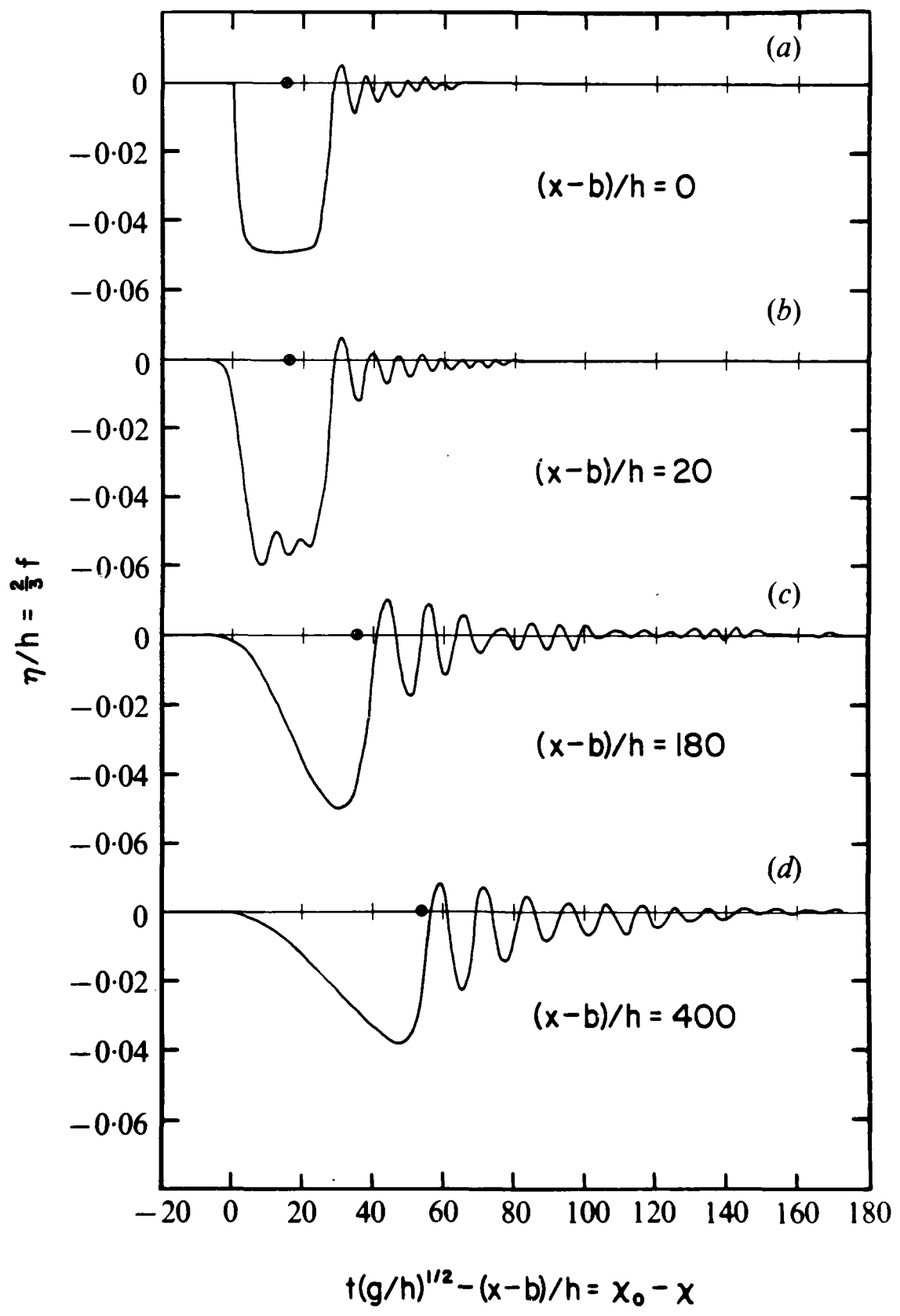


FIGURE 3



$$t(g/h)^{1/2} - (x-b)/h = \chi_0 - \chi$$

FIGURE 4



AD-A101 384

CALIFORNIA UNIV BERKELEY DEPT OF CIVIL ENGINEERING  
EXPERIMENTAL SOLITON WAVES. (U)

NOV 80 J HAMMACK

F/0 8/3

N0001R-78-C-0889

ML

UNCLASSIFIED

2 x 2  
40 A  
113.04

END  
DATE  
FILED  
8-81  
DTIC

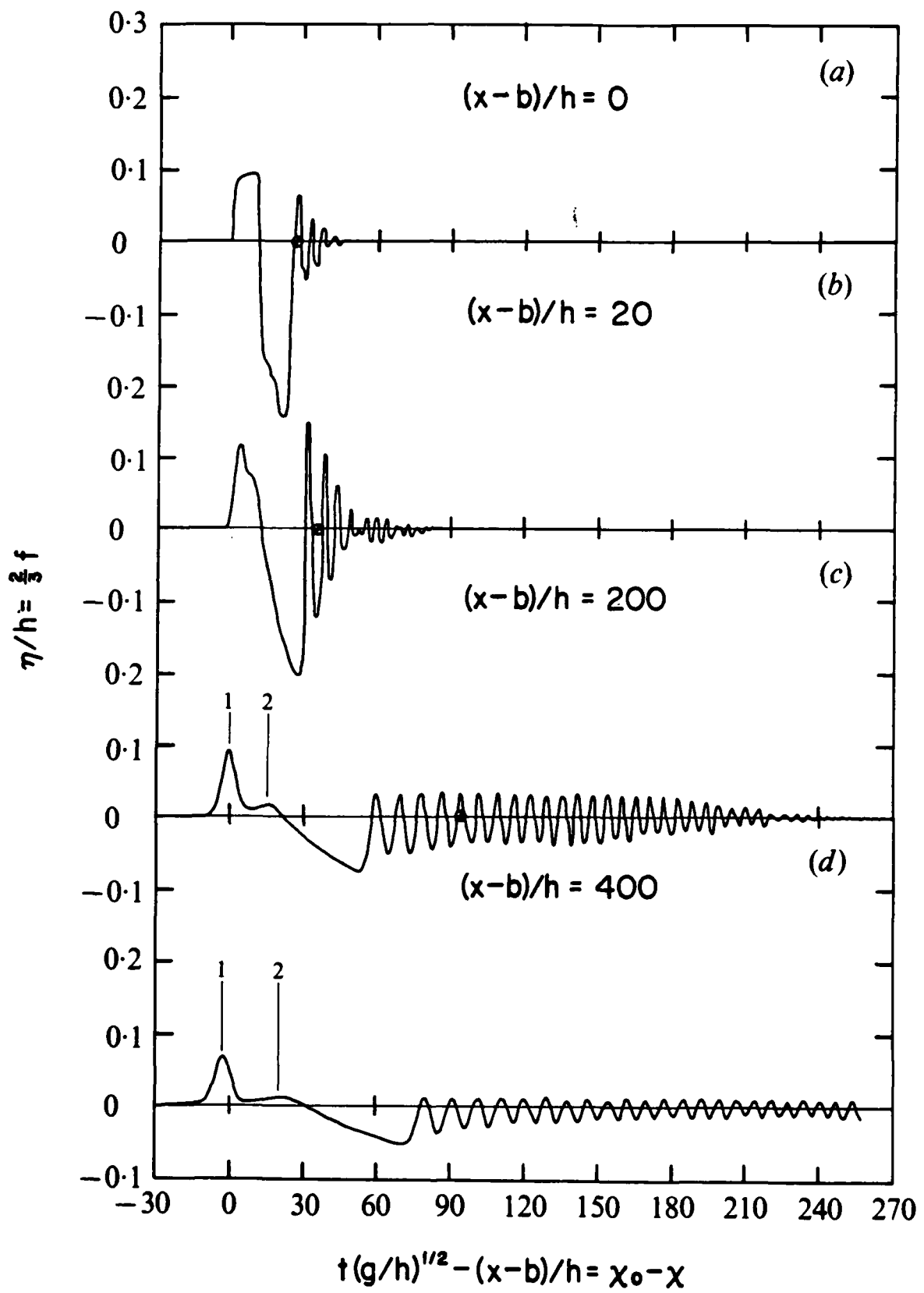


FIGURE 6

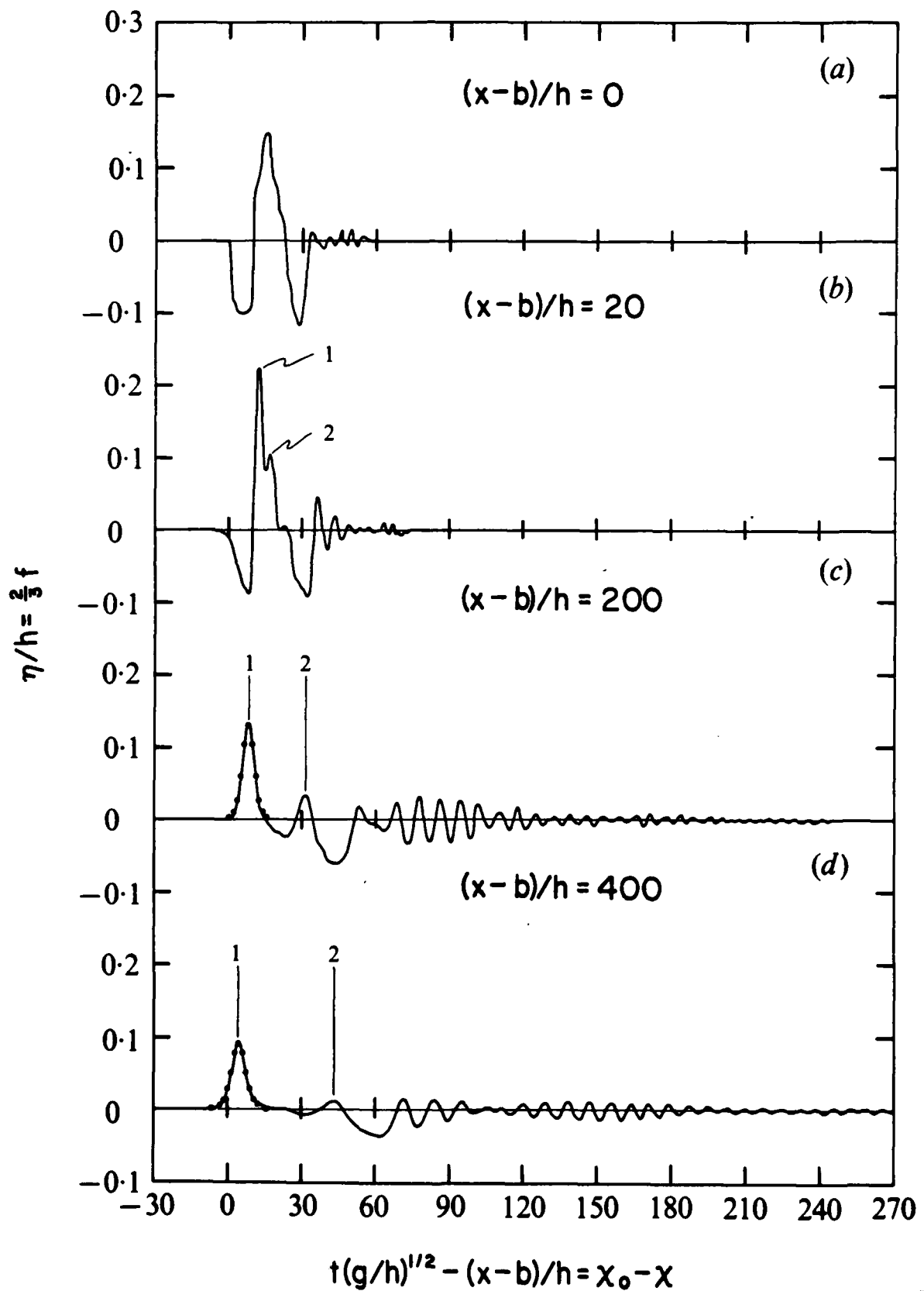


FIGURE 7

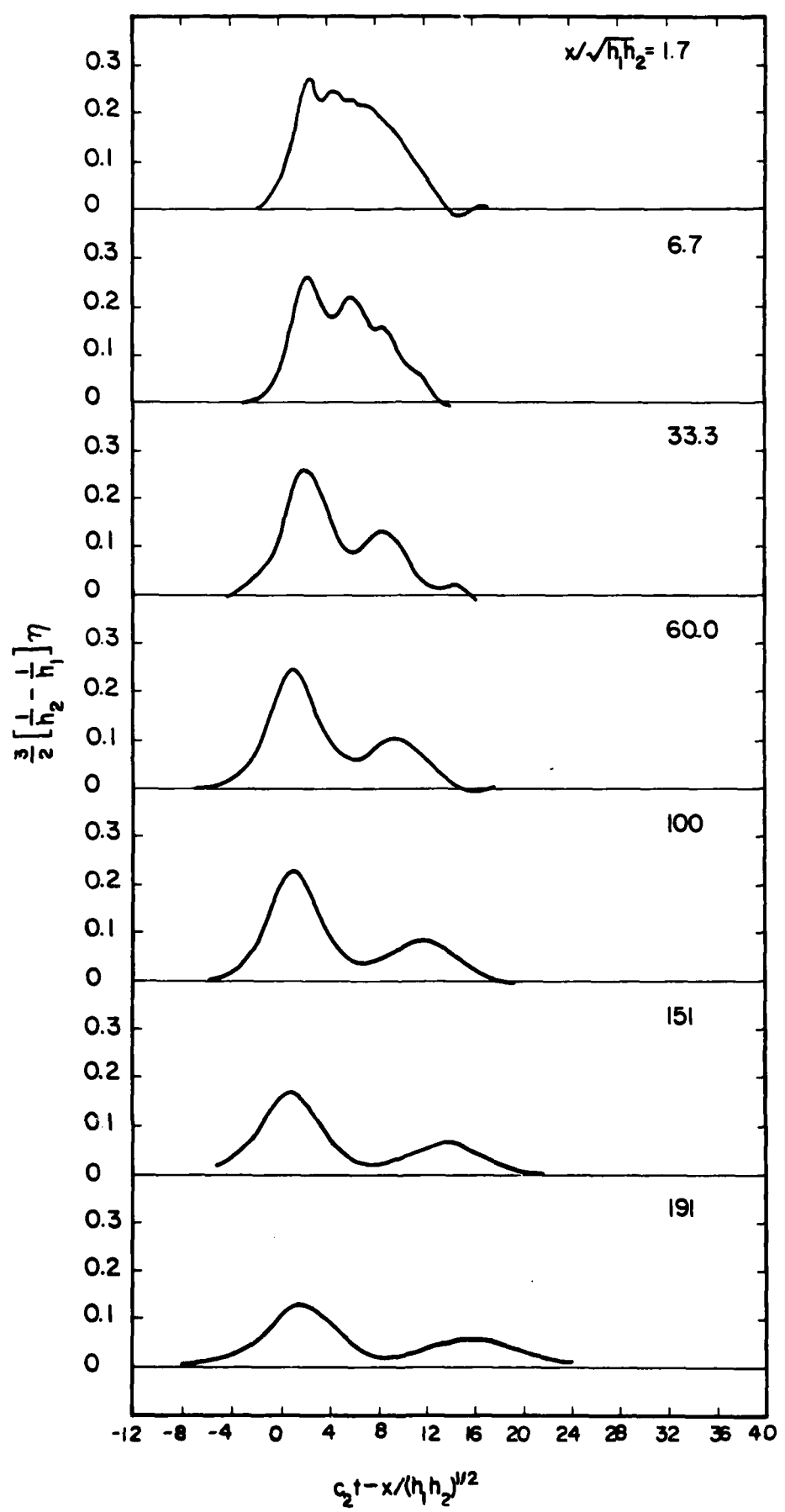


FIGURE 8

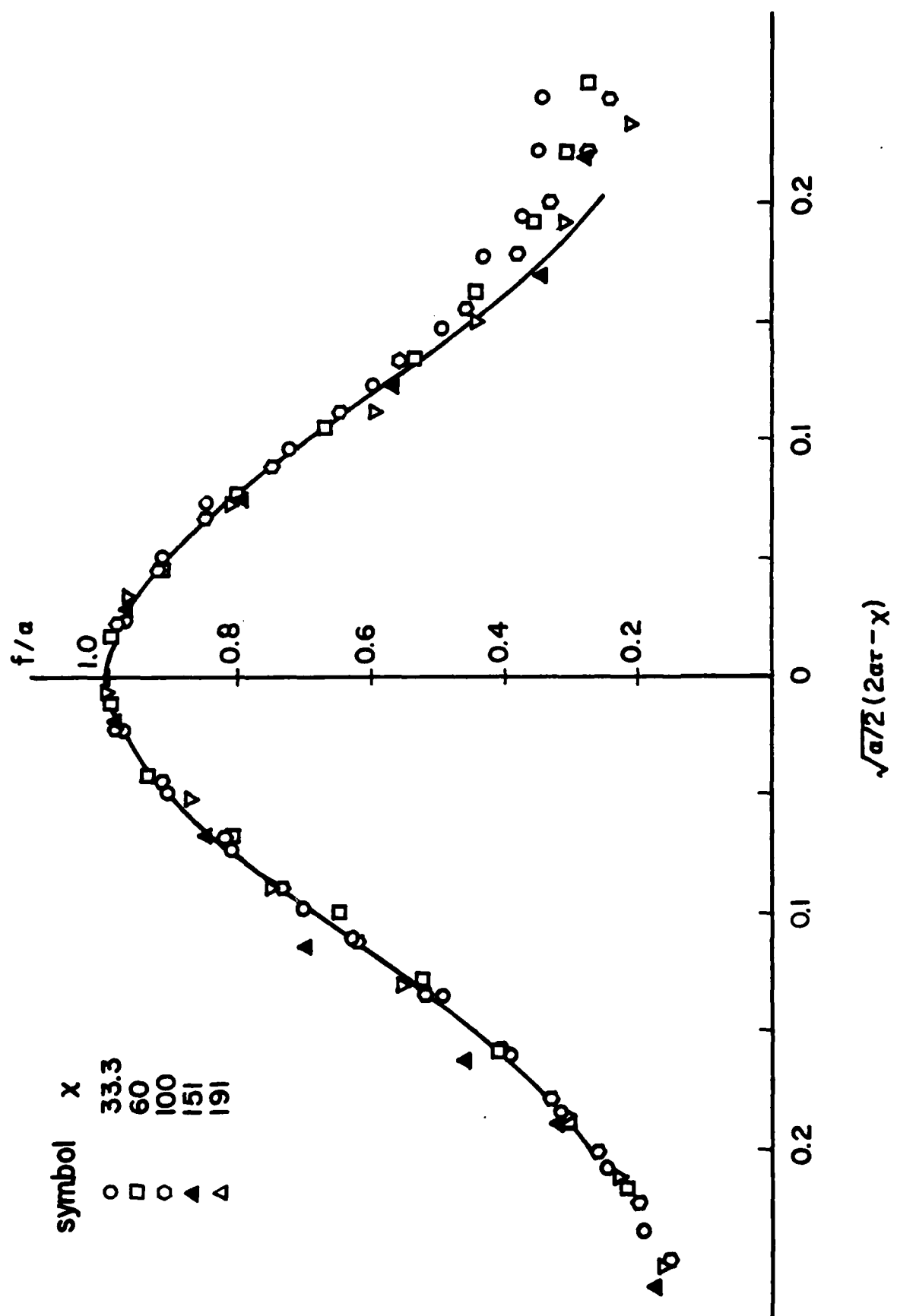


FIGURE 9

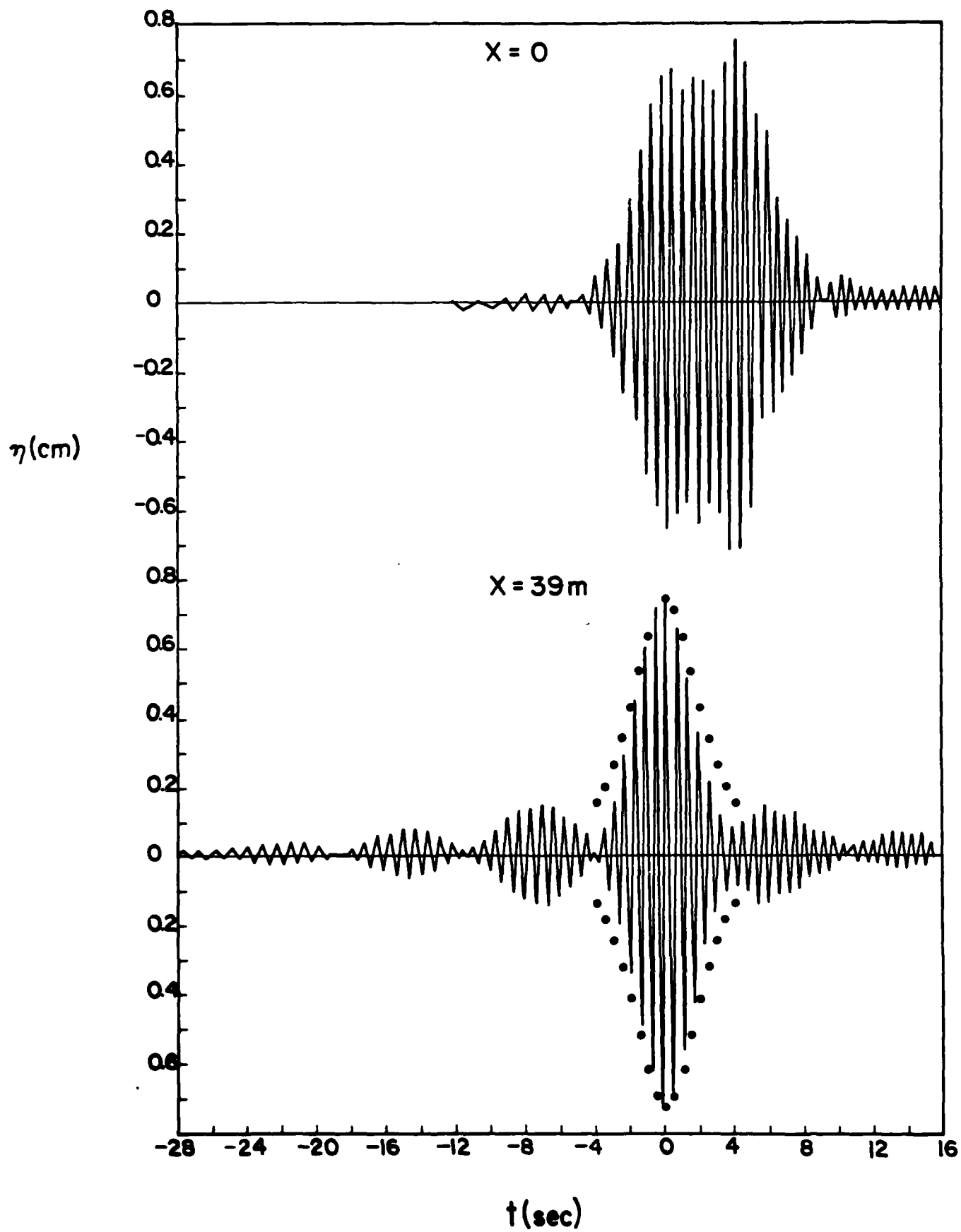


FIGURE 10

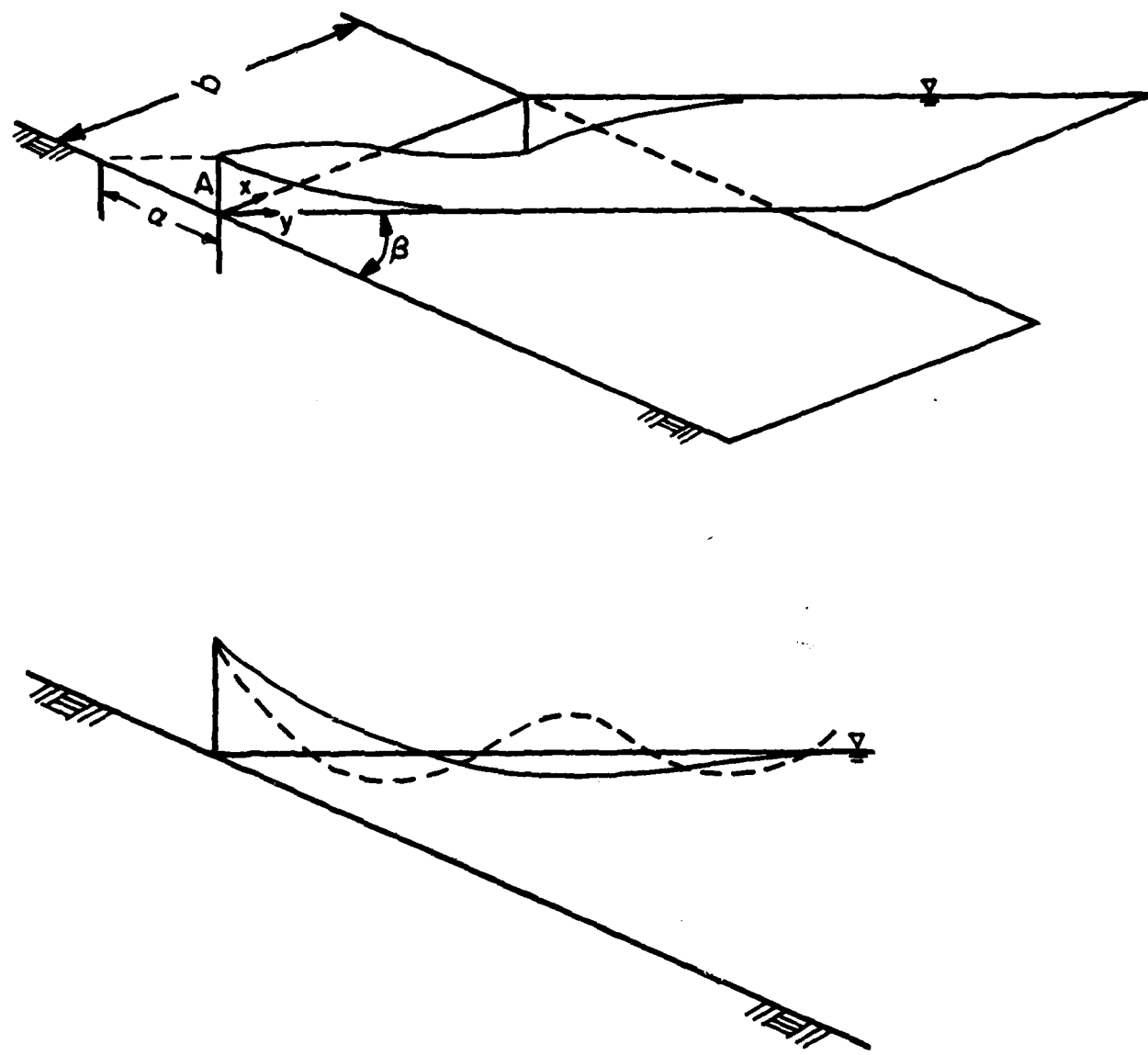


FIGURE 11

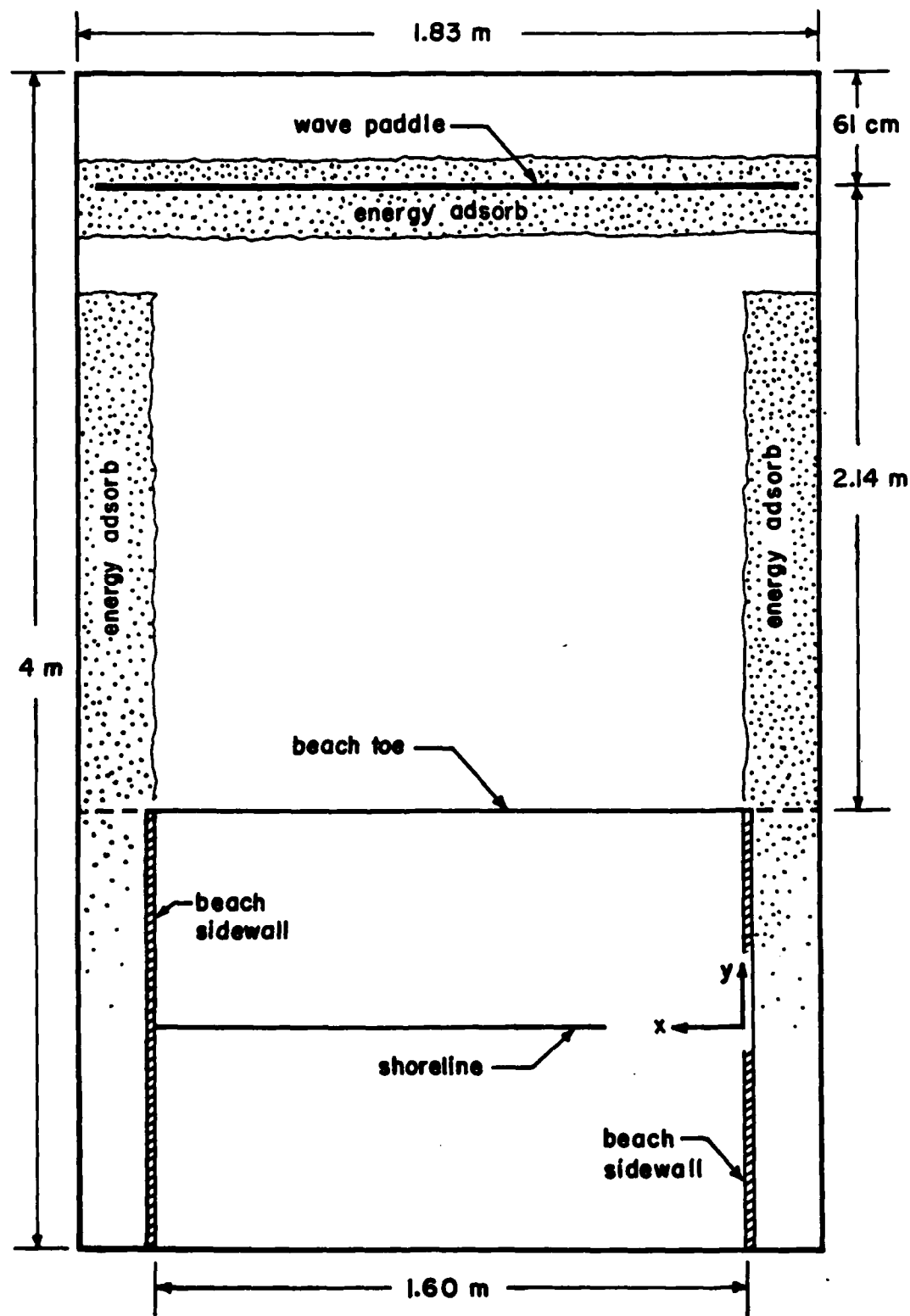


FIGURE 12

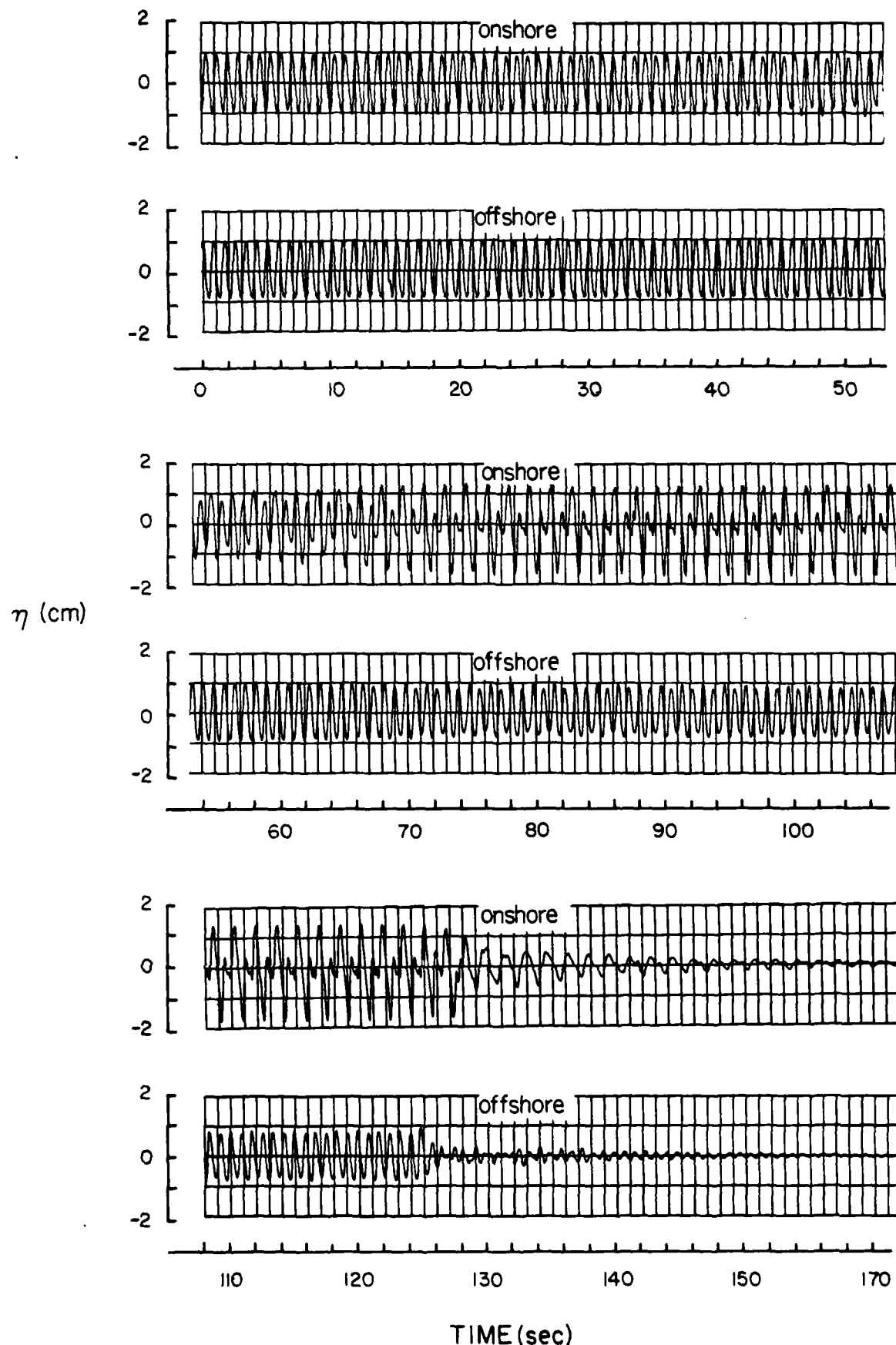


FIGURE 13

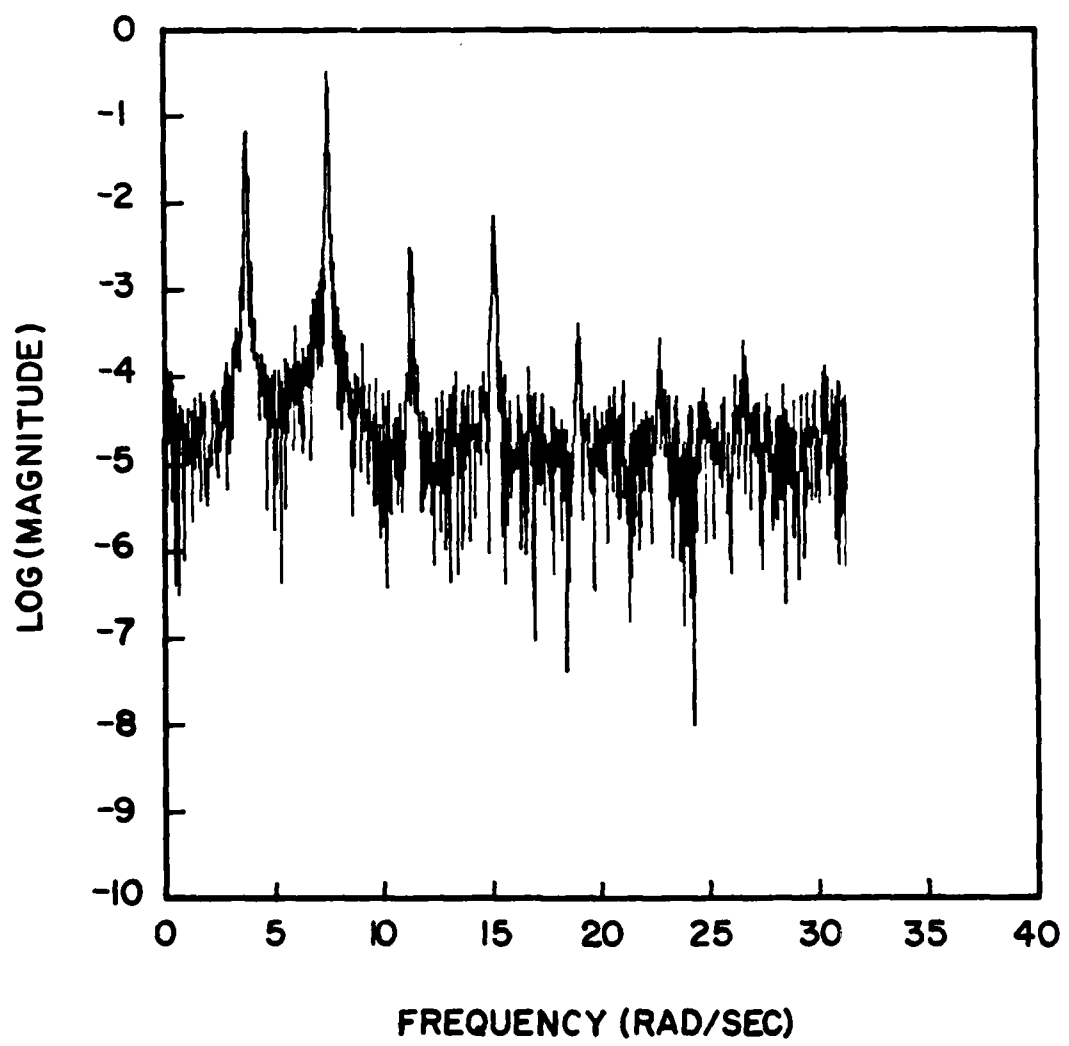


FIGURE 14

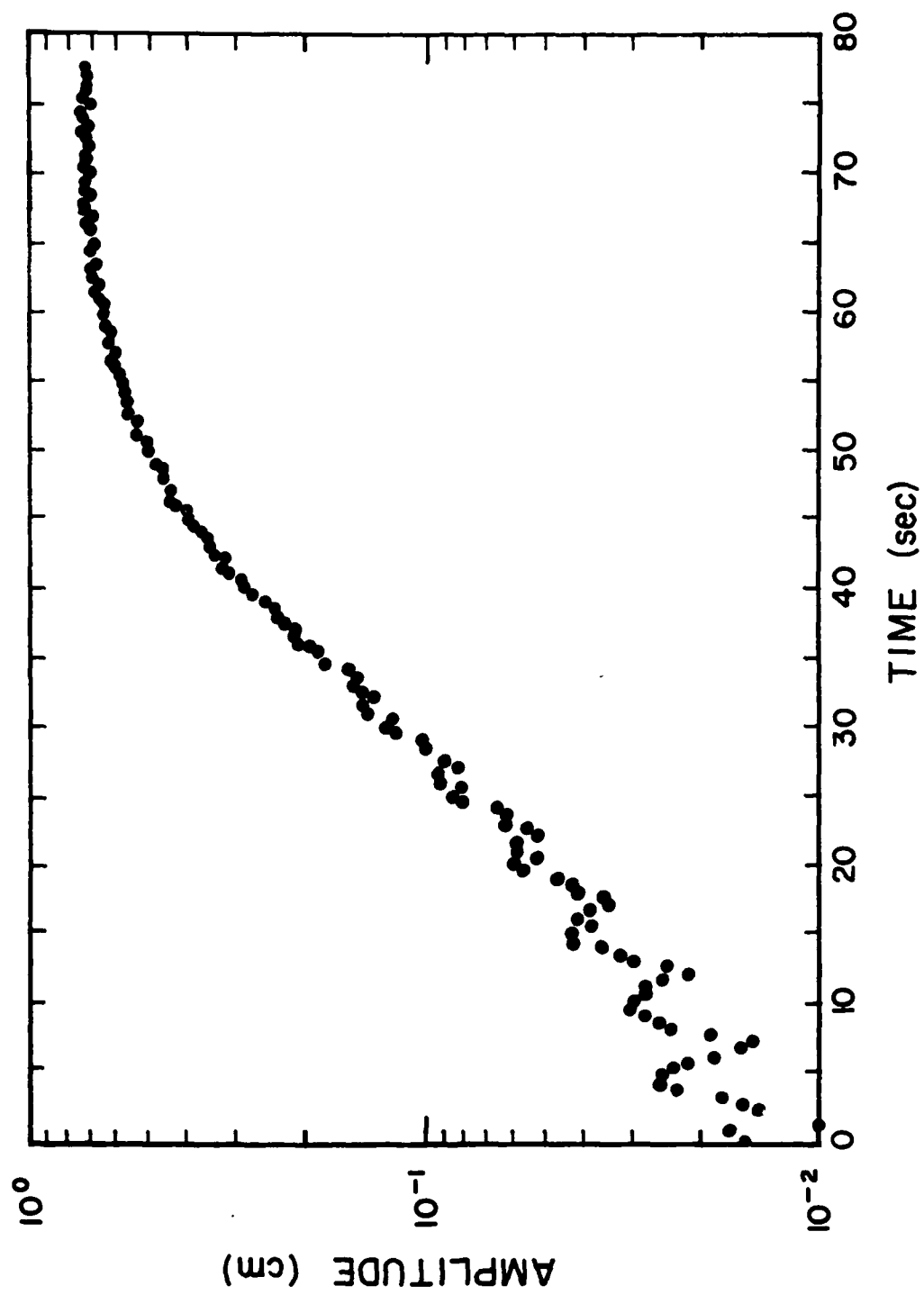


FIGURE 15

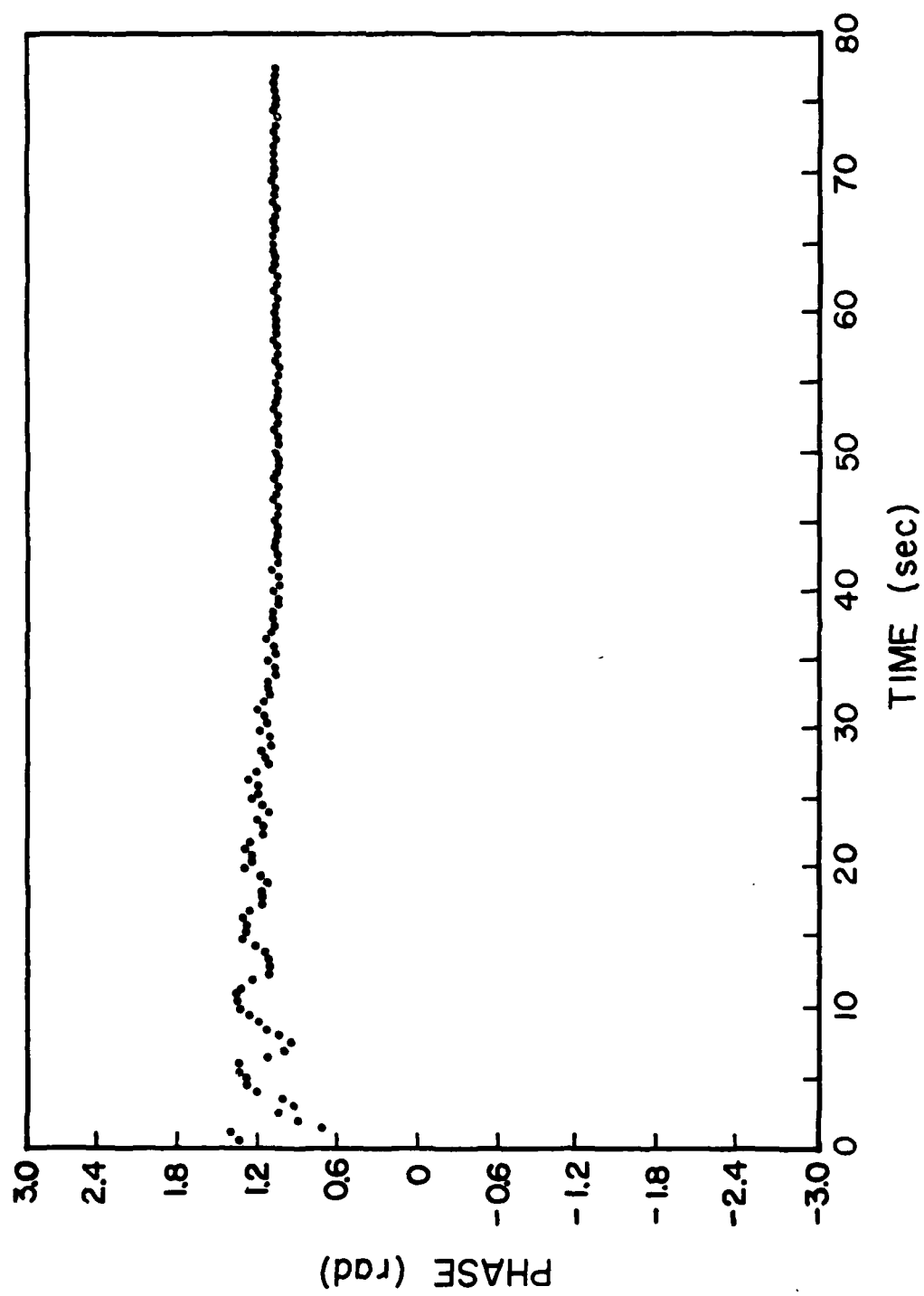


FIGURE 16

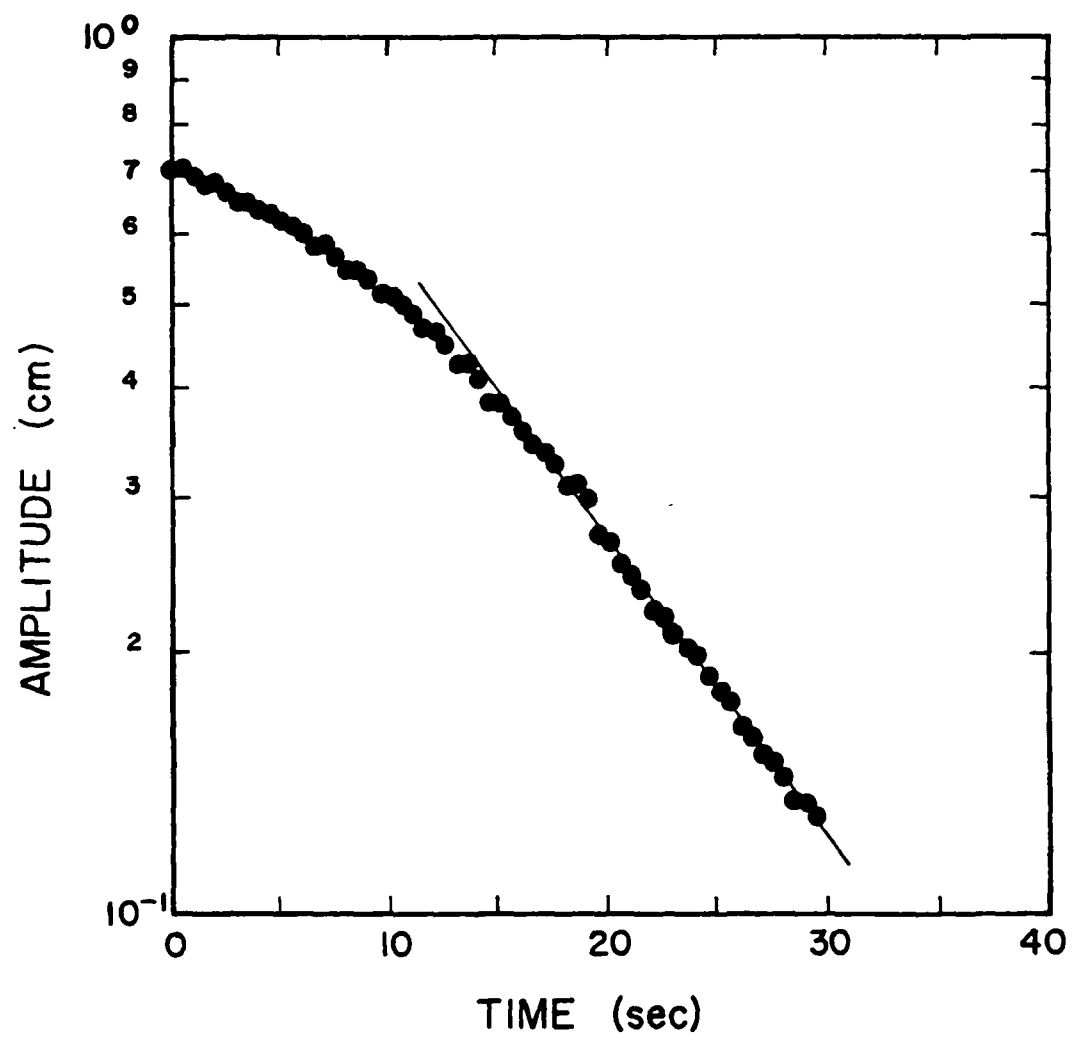


FIGURE 17

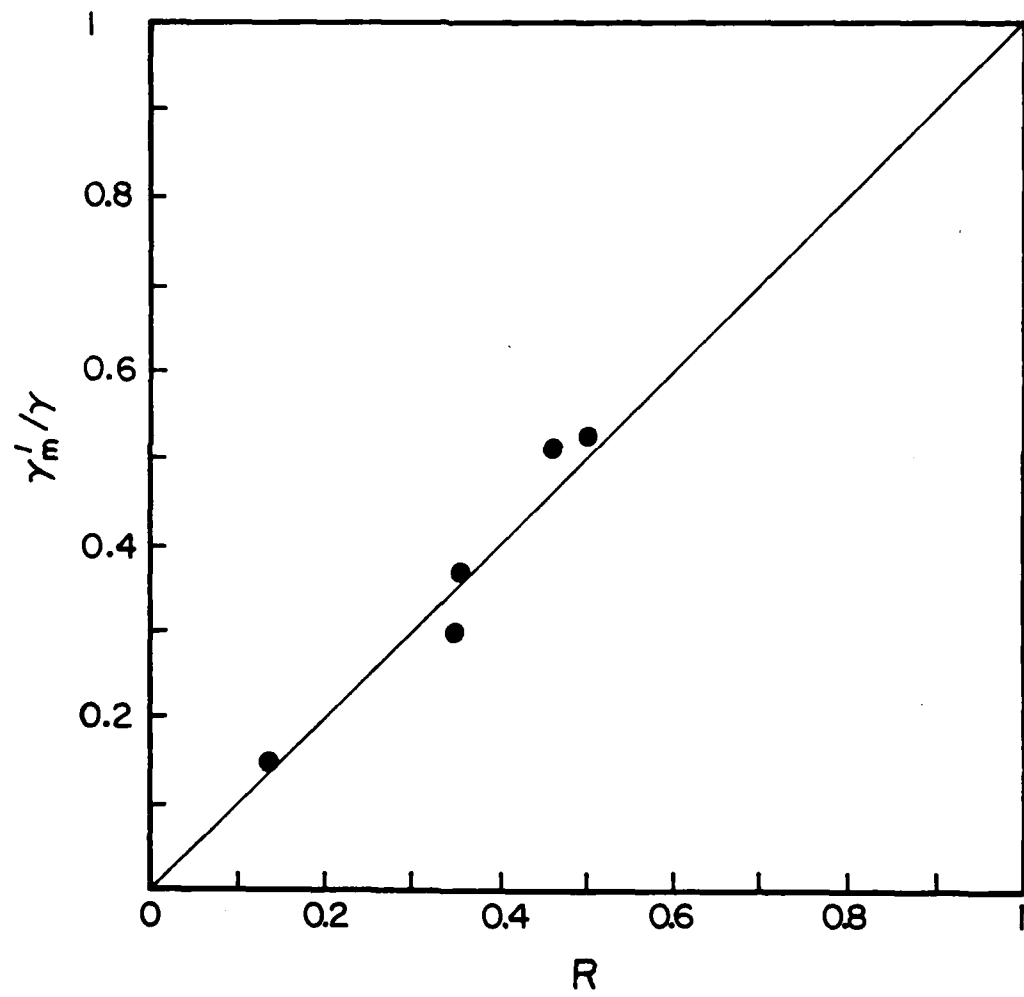


FIGURE 18